



DEVELOPMENT AND VALIDATION OF AUTOMATED OPTO-MECHATRONIC SCREENING SOLUTIONS FOR 3D TUMOUR MODEL ENGINEERING

Entwicklung und Validierung von automatisierten opto-mechatronischen
Screening-Lösungen für 3D-Tumormodelle

Der Technischen Fakultät
Der Friedrich-Alexander-Universität Erlangen-Nürnberg
zur
Erlangung des Doktorgrades Dr.-Ing.
vorgelegt von

Melanie Kahl

Submitted in fulfilment of the requirements for the degree of
Doctor of Philosophy
Centre for Biomedical Technologies
Faculty of Health
Queensland University of Technology

2022

Centre for Biomedical Technologies
School of Biomedical Sciences
Faculty of Health
Queensland University of Technology

Lehrstuhl für Medizinische Biotechnologie
Technische Fakultät
Friedrich-Alexander-Universität
Erlangen-Nürnberg



Als Dissertation genehmigt
von der Technischen Fakultät
der Friedrich-Alexander-Universität Erlangen-Nürnberg

Tag der mündlichen Prüfung:
20.03.2023

Gutachter/in: Prof. Dr. Aldo R. Boccaccini
Prof. Dr. Yi-Chin Toh

Keywords

3D cell culture, automation, biomanufacturing workstation, compression test, fluorescence, GelMA, hydrogel, linear actuator, low-cost, microscope, open-source, reproducibility

Abstract

Hydrogels are a vital part of 3D cell culture techniques. They can mimic the native cellular microenvironment and hence contribute to producing more physiologically relevant results than standard cell cultures cultivated in 2D monolayers. However, cost-effective automated solutions for hydrogel-based cell culture workflows are required to increase the throughput and obtain more reproducible user-independent results. Indeed, 3D bioprinters can handle viscous materials such as hydrogel precursor solutions; however, their throughput is currently low, they are limited to specific biomaterials, and they lack subsequent post-processing and analysis methods. Contrary, liquid handlings robots and workstations have higher throughput, but they are missing viscous materials handling capabilities. In addition, commercial systems are not only expensive but mostly also not open-source and hence not adaptable to specific experimental requirements.

Therefore, a biomanufacturing workstation has been developed, capable of handling non-viscous and viscous solutions with integrated modules for hydrogel photo-crosslinking and storage for up to six tissue culture plates. Thus, the aim of this thesis is the validation and application of the newly developed workstation and the implementation of an opto-mechatronic screening module for automated 3D cell culture workflows from production to analysis.

In a first step, automated workflows for the preparation of GelMA-based hydrogels with reproducible, user-independent results were developed, and the analysis of compression test data of hydrogels was automated. Secondly, an analysis module with an inverted fluorescence widefield microscope and a motorised XYZ stage was engineered to transport tissue culture plates from the storage rack of the workstation to the microscope and assess fluorescence-based cell parameters, such as viability and morphology. Lastly, viability assays and drug-response studies were conducted on 3D tumour models to demonstrate the capabilities of the newly developed opto-mechatronic screening module.

Altogether, the integration of an opto-mechatronic screening module into the biomanufacturing workstation enables the automated, reproducible and user-independent production and analysis of hydrogels-based 3D cell cultures.

Zusammenfassung

Hydrogele sind ein wesentlicher Bestandteil von 3D-Zellkulturen. Sie können die Mikroumgebung von Zellen nachbilden und tragen somit dazu bei, physiologisch relevante Ergebnisse zu produzieren, verglichen mit den standard 2D-Zellkulturen. Jedoch fehlen Technologien, um die Arbeitsschritte für Hydrogel-basierte Zellkulturen zu automatisieren und somit den Durchsatz zu erhöhen, um reproduzierbarere, nutzerunabhängige Ergebnisse zu erzielen. 3D-Biodrucker bieten zwar die Möglichkeit, viskose Materialien exakt zu positionieren, doch ihr Durchsatz ist gering und anschließende automatisierte Weiterverarbeitungs- und Analysemöglichkeiten fehlen. Pipettierroboter hingegen haben einen höheren Durchsatz, jedoch können sie oft keine viskosen Flüssigkeiten verarbeiten.

Daher wurde eine *Biomanufacturing Workstation* entwickelt, die sowohl nichtviskose als auch viskose Flüssigkeiten verarbeiten kann. Zusätzlich hat die *Workstation* ein Modul für *photo-crosslinking*-Reaktionen und eine Aufbewahrung für bis zu sechs Zellkulturplatten integriert. Deshalb war das Ziel dieser Dissertation, die neu entwickelte *Workstation* zu validieren, anzuwenden und ein opto-mechatronisches Analysemodul zu integrieren.

Im ersten Schritt wurden automatisierte Arbeitsschritte mit reproduzierbaren, nutzerunabhängigen Ergebnissen für das Handling von GelMA-basierten Hydrogelen entwickelt und die Analyse von mechanischen Kompressionstest-Daten von Hydrogelen automatisiert. Im zweiten Schritt wurde ein Analysemodul mit einem inversen Weitfeld-Floreszenzmikroskop und einer motorisierten XYZ-Plattform entwickelt, um Zellkulturplatten vom Aufbewahrungsmodul zum Mikroskop zu transportieren und automatisiert die Fluoreszenz aufzunehmen, um z. B. die Viabilität von Zellen auszuwerten. Im dritten und letzten Schritt wurden zellbasierte Viabilitätsassays und *Drugscreenings* durchgeführt, um die Anwendbarkeit des neu entwickelten Moduls zu demonstrieren.

Somit ermöglicht die Integration eines automatisierten Mikroskops mit kombinierter motorisierter XYZ-Plattform in die *Biomanufacturing Workstation* eine reproduzierbare, nutzerunabhängige Herstellung, Verarbeitung und Analyse von Hydrogel-basierten 3D Zellkulturen ohne manuelles Eingreifen.

Table of Contents

Keywords	ii
Abstract.....	iii
Zusammenfassung.....	iv
Table of Contents.....	v
List of Figures.....	vii
List of Tables	ix
List of Abbreviations	x
Acknowledgements.....	xi
Chapter 1: Introduction	1
Chapter 2: State of the Art.....	5
2.1 3D Cell Culture and the Influence of the Cellular Microenvironment	5
2.1.1 Microenvironment	5
2.1.2 3D cell culture and hydrogels.....	8
2.1.3 Applications of 3D cell culture systems	12
2.2 Laboratory Automation Technology	15
2.2.1 Automation in the life sciences	15
2.2.2 Automation of 3D cell cultures	17
2.2.3 Biomanufacturing workstation	18
2.3 Automated Microscopy Systems	20
2.3.1 Fluorescence microscopy	20
2.3.2 Open-source microscopes.....	25
2.4 Summary and Implications	27
2.4.1 Requirements for the opto-mechatronic screening module.....	28
Chapter 3: Research Design.....	31
3.1 Aim 1: Validation of the Biomanufacturing Workstation	31
3.1.1 Implementation of an automated and reproducible workflow for manufacturing of gelatin methacryloyl (GelMA)-based hydrogels.....	31
3.1.2 Conception of a parameter library	36
3.1.3 Automated analysis of compression test data with <i>MechAnalyze</i>	38
3.2 Aim 2: Integration of an Imaging Module.....	41
3.2.1 Fluorescence microscope.....	42
3.2.2 XYZz-stage	47
3.2.3 Integration and software	52
3.3 Aim 3: Proof-of-Concept Study.....	54
3.3.1 Live/dead viability assays.....	55
3.3.2 Drug-response study.....	56
3.3.3 Imaging and image analysis	59
3.3.4 Statistical analysis	59
Chapter 4: Results.....	61
4.1 Aim 1: Validation of the Biomanufacturing Workstation	61

4.1.1	Implementation of an automated and reproducible workflow for manufacturing of gelatin methacryloyl (GelMA)-based hydrogels	61
4.1.2	Conception of a parameter library to produce GelMA-based hydrogels with specific mechanical properties.....	69
4.1.3	Automated analysis of compression test data with <i>MechAnalyze</i>	70
4.2	Aim 2: Integration of an Imaging Module	74
4.2.1	The opto-mechatronic screening module and its integration into the workstation	74
4.2.2	Validation of the microscope	75
4.2.3	Validation of the XYZz-stage.....	78
4.2.4	Software and graphical user interface	82
4.3	Aim 3: Proof-of-Concept Study.....	84
4.3.1	Live/dead cell viability assays	84
4.3.2	Drug-response study	87
Chapter 5:	Discussion	99
5.1	Aim 1: Validation of the Biomanufacturing Workstation	99
5.1.1	Automated and reproducible workflow	99
5.1.2	Parameter library.....	102
5.1.3	Automated analysis of unconfined compression test data using <i>MechAnalyze</i>	103
5.2	Aim 2: Integration of an Imaging Module	106
5.2.1	The opto-mechatronic screening module and its integration into the workstation	106
5.2.2	Validation of the microscope	109
5.2.3	Validation of the XYZz-stage.....	111
5.2.4	Operation of the OMSM.....	112
5.3	Aim 3: Proof-of-Concept Study	113
5.3.1	Time-dependent live/dead cell viability assay	113
5.3.2	Endpoint and time-dependent drug-response studies.....	113
Conclusions	117	
Bibliography	121	
Appendices	137	

List of Figures

Figure 1.1 High-throughput screenings on 3D tumour models	2
Figure 2.1 Literature search on 3D drug screenings	14
Figure 2.2: General workflow of a HTS	16
Figure 2.3 Biomanufacturing workstation	19
Figure 2.4 Fluorescence principle	21
Figure 3.1 Automated workflow for the production of GelMA-based hydrogels	33
Figure 3.2 Calculation of the compressive modulus	35
Figure 3.3 Optimisation workflow	35
Figure 3.4 Box-Behnken-Design with design points on the edges and in the centre	37
Figure 3.5 <i>MechAnalyze</i> workflow and output example	40
Figure 3.6 Microscope and its lightpath	43
Figure 3.7 Microscope assembly	45
Figure 3.8 Wavelength spectra of multi-band fluorescence filter, LED and two dyes for live/dead imaging	46
Figure 3.9 Assembly of the X- and Y-stage	48
Figure 3.10 Assembly of the XYZz-stage	50
Figure 3.11 Process workflow of the OMSM-module	52
Figure 3.12 Electronics of the XYZz-stage	54
Figure 3.13 Timeline of the endpoint drug-response study	57
Figure 3.14: Timeline of time-dependent drug-response study	58
Figure 4.1 Influence of three different micowell-plate types on the compressive modulus of GelMA hydrogels	62
Figure 4.2 Compressive moduli of 10% GelMA and 0.15% (0.30%) LAP concentration crosslinked for 2, 4 and 8 min	63
Figure 4.3 Mixing optimisation – absorption measurements of 10% GelMA manufactured with PBS mixed with Orange G	66
Figure 4.4 Optimised automated mixing step	67
Figure 4.5 Optimised mixing protocols for 5% and 15% GelMA hydrogels	68
Figure 4.6 Reproducibility of crosslinked GelMA hydrogels	68
Figure 4.7 Parameter library	69
Figure 4.8 Comparison of manual and automatically analysed compression test data	71

Figure 4.9 Variability of manually analysed datasets between individual researchers and <i>MechAnalyze</i>	73
Figure 4.10 Opto-mechatronic screening module and its integration into the biomanufacturing workstation	75
Figure 4.11 Resolution and contrast of the Raspberry Pi HQ camera	76
Figure 4.12 Axial resolution of the microscope	77
Figure 4.13 GFP microsphere calibration	79
Figure 4.14 Repeatability and accuracy of the XYZz-stage	80
Figure 4.15 Spatial resolution of the X- and Y-axis	81
Figure 4.16 Spatial resolution of the Z-fine and Z-coarse axis	82
Figure 4.17 Graphical user interface	83
Figure 4.18 Fluorescence images of the live/dead viability assay	85
Figure 4.19 Comparison of opto-mechatronic screening module with a conventional fluorescence microscope	86
Figure 4.20 Endpoint (3 days) drug-response study of PC-3 cells treated with docetaxel	88
Figure 4.21 Analysis of endpoint drug-response study.....	90
Figure 4.22: Representative images of the time-dependent drug-response study of PC-3 cells cultured in 2D.....	91
Figure 4.23: Representative images of the time-dependent drug-response study of PC-3 cells cultured in 3D.....	93
Figure 4.24: Viability and cell number of the time-dependent drug-response study	95
Figure 4.25: Analysis of morphology	97

List of Tables

Table 2.1: Advantages and disadvantages of GelMA being used for vitro 3D models and the automated fabrication process	12
Table 3.1 Factors for DoE approach	38
Table 4.1 Mixing optimisation experiment 5 – decrease in duration of mixing step by increasing dispension speed	65
Table 4.2: Viability of PC-3 cells cultured in 2D and 3D calculated on the basis of image taken with OMSM and Nikon Eclipse Ti, respectively (n = 6)	86
Table 4.3: IC ₅₀ values for docetaxel and results of the null hypothesis test for 2D and 3D cultured PC-3 cells	96

List of Abbreviations

2D	Two-dimensional
3D	Three-dimensional
DMSO	Dimethyl sulfoxide
DoE	Design of Experiment
DTX	Docetaxel
ECM	Extracellular matrix
EthD-III	Ethidium homodimer III
FWHM	Full width of half maximum
GelMA	Gelatin methacryloyl
GFP	Green fluorescent protein
GUI	Graphical user interface
HA	Hyaluronic acid
HCS	High-content screening
HTS	High-throughput screening
LAP	Lithium phenyl-2,4,6-trimethylbenzoylphosphinate
LED	Light-emitting diode
OMSM	Opto-Mechatronic Screening Module
PBS	Phosphate buffered saline
PWM	Pulse-width modulation

Acknowledgements

First and foremost, I thank my principal supervisors, Prof Dr Dr Oliver Friedrich and D/Prof Dietmar Hutmacher, for their support, guidance, encouragement, and advice throughout my PhD. Many thanks also go to my associate supervisors, Dr Nathalie Bock and Dr Christoph Meinert, for their valuable help, support and feedback. Additionally, I acknowledge my funding support, as this research was supported by QUT Postgraduate Research Award scholarship.

I also thank the members of both research groups, the Regenerative Medicine group and the members of the MBT, for their advice, help and companionship.

In particular, I want to thank Sebastian Eggert for his introduction to his project, our collaboration and for letting me pursue his project. In addition, I thank Hannah, Margaux, Tina, Marietta and all other members of the RM group I made friends with and for the invaluable memories of exploring Australia.

Many thanks also go to my colleagues in the USS for creating many memorable, cheerful moments. Special thanks go to Dominik Schneidereit for the valuable feedback discussions, Ulrike Schöler for her help in the laboratory and cell culture, and Christian Lesko for his expertise on linear actuators and ball screws. I also thank our workshop staff at the MBT, Axel Stolz and Gerhard Prölß, for their help with the mechanical and electrical components.

Doing a Joint PhD on two continents ending up in a global pandemic with months-long border restrictions is not always easy. However, I am very thankful for my supportive family, particularly my parents, Margret und Reiner, and my dearest friends, Ann-Christin, Jannah, Lea, Maria, Victoria and Jonas. A bunch of flatmates accompanied me during my PhD due to the nature of a binational PhD. Special thanks go to my flatmates in Brisbane, Nelly and Alex, for being my “Australian” family. Many thanks go to flatmates in Erlangen, Sandra, Ruth, Katha and Adrian, for getting through months of lockdowns together with innumerable cooking and board game sessions. Last but not least, I thank my partner Christoph not only for the gravel bike rides on the weekends but also for his endless support, motivation speeches and patience, especially in the last months of this PhD.

Chapter 1: Introduction

In drug discovery, cancer has one of the worst success rates amongst other therapeutic areas, mainly caused by the high heterogeneity and complexity of this disease. Approximately 95% of drug candidates, which produced promising results in preclinical studies and *in vitro* screenings, failed during clinical trials [1], [2]. *In vitro* screenings are an essential part in different phases within the drug discovery phases from the primary compound screening, to target identification and secondary assays to mechanism of action studies and *in vitro* toxicology assays [3]. Therefore, it is necessary to reflect this diversity of cancer in the drug discovery process by applying highly flexible and modular technologies, which enable the use of various cell types and culturing techniques.

To address the inability of two-dimensional (2D) cell cultures to mimic the complexity of *in vivo* solid tumours and the low-throughput, high costs, poor translatability, and ethical challenges associated with animal models, 3D *in vitro* tumour models “bridge the gap” between 2D screenings and *in vivo* experiments by recapitulating major clinical tumour features [2], [4], [5]. However, automation is necessary to increase the throughput of 3D drug screenings. Although several solutions to automate the production of 3D tumour models already exist [6], [7], most of them are based on self-aggregation of cells on low adhesion surface plates [8] or hanging drop techniques [9], [10]. However, these methods do not fully replicate a physiological extracellular microenvironment. Thus, cell-matrix interactions, which strongly influence the tumour phenotype, diffusion rate and drug delivery [11], are not considered. Nevertheless, drug screenings on 3D tumour models have not been undertaken extensively due to the labour-intensive production of scaffold-based 3D models and their analysis [12]. Additionally, most systems for automated production and incorporated analysis units for high-throughput screenings (HTS) and high-content screening (HCS) of 3D cell models are still in the proof-of-concept phase and do not provide sufficient robustness and validated results [13]. The steps from the uptake of staining reagents to imaging 3D structures in high-throughput in a reasonable time and appropriate resolution are still the main issues that must be handled [14], [15]. In addition, while high-content imaging technologies exist, these have been developed

to suit 2D samples. Challenges remain in Z-axis rendering and automated image analysis of 3D spheroids. Hence, to address the needs to perform successful high-throughput screenings on 3D tumour models, expertise from multiple research disciplines such as cancer research, materials science, automation technology and microscopy techniques is necessary (Figure 1.1).

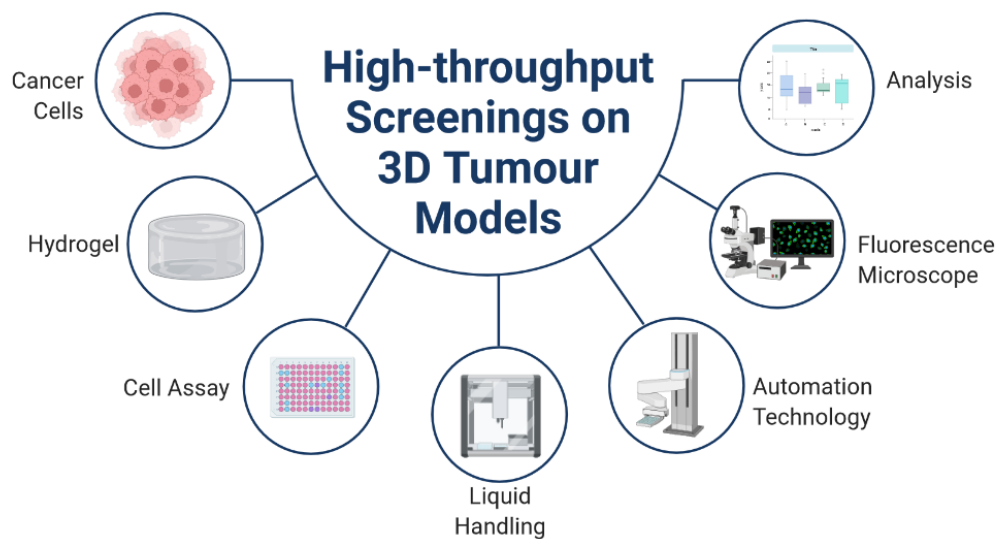


Figure 1.1 High-throughput screenings on 3D tumour models

To address the needs for high-throughput screenings on 3D tumour models, expertise from multiple research disciplines is necessary (created with BioRender.com).

To overcome these challenges, new technology is necessary that automates the production and analysis of 3D models suitable for various applications. Hydrogels, which suit many cell types and show similarities to the native extracellular matrix, like gelatin methacryloyl (GelMA), provide a flexible platform due to their tuneable properties. Therefore, this thesis offers automated solutions for 3D *in vitro* tumour models using hydrogel-encapsulated cancer cells. To facilitate drug screenings on 3D tumour models, the entire workflow from hydrogel construct manufacturing, processing, imaging, and analysis shall be automated in an open-source approach using an in-house developed liquid handling workstation with a newly developed imaging module. The liquid handling workstation was developed by Eggert et al. to automate the production of hydrogel-based 3D cell cultures. It incorporates a pipetting robot, equipped with positive-displacement pipettes for handling viscous and non-viscous materials, a crosslinking and a storage module for tissue culture plates [16], [17]. Based on this workstation, automated workflows and analysis methods were

established by converting previously established manual steps of hydrogel production, such as liquid handling of viscous solutions and photo-crosslinking, to match the requirements of high-throughput manufacture and screening applications. A parameter library dedicated to this workstation enables automated biomanufacturing of hydrogels with desired stiffness to accommodate the needs of various cell types and experimental hypotheses. A newly developed algorithm, *MechAnalyze*, automated the analysis of mechanical compression tests of hydrogels. Implementing an automated fluorescence-based imaging module facilitates drug screenings on 3D cell culture models with increased throughput and minimal manual intervention, paving the way for more widespread uptake of the next generation of cell culture by the cancer research community.

This thesis is structured into four main chapters. The next chapter, “State-of-the-Art,” summarises the current research on 3D cell culture models and the importance of the cellular microenvironment. Commercial and open-source technologies for 3D cell cultures and their analysis based on fluorescence microscopy are described. The following three chapters are subdivided into three aims of this thesis. The first aim is to establish automated workflows on the biomanufacturing workstation. The second aim is to establish and validate an imaging module, which can be integrated into the biomanufacturing workstation. The third aim connects the first and second aim with proof-of-concept studies on the newly developed imaging module. Hence, the third chapter, “Research Design”, explains the design of experimental studies and the development and assembly of specialised hardware and software. The generated results are presented in the following chapter, “Results”, then discussed and evaluated in the chapter “Discussion”. Finally, the last chapter summarises and concludes the findings and limitations of this thesis and gives an outlook towards future applications.

Chapter 2: State of the Art

This chapter begins with an introduction to 3D cell culture (2.1). It reviews the literature on the following topics: The microenvironment of cells and tumours, hydrogels and the application of 3D cell culture and hydrogel-based systems. Section 2.2 delineates automation technology in the field of life science, especially for 3D cell culture. The fundamentals of fluorescence microscopy and open-source microscope systems are described in section 2.3. Section 2.4 highlights the implications from the literature and defines the requirements of this project.

2.1 3D CELL CULTURE AND THE INFLUENCE OF THE CELLULAR MICROENVIRONMENT

2.1.1 Microenvironment

In vivo, cells do not exist in isolation; instead, they are surrounded by a tissue- and state-specific microenvironment; this microenvironment consists of other types of cells, blood vessels, and the extracellular matrix (ECM), which all influence cellular processes and pathways. Hence, the ECM, the interactions of cells with their surrounding environment and the importance of stiffness is described below.

In tumour formation and progression microenvironmental factors play a critical role. Various stromal cells, such as cancer-associated fibroblasts, immune cells, and endothelial cells secrete growth factors, cytokines, and ECM components that can promote tumour cell proliferation, angiogenesis and invasion. In order to receive nutrients and oxygen, tumours require blood supply. Hence, tumour and stromal cells release pro-angiogenic factors such as vascular endothelial growth factor (VEGF), promoting the recruitment and proliferation of endothelial cells to form new blood vessels. However, in solid tumours, oxygen deprivation or hypoxia are also common features activating various signalling pathways, such as hypoxia-inducible factor (HIF) pathway, leading to the expression of genes involved in angiogenesis, metabolic adaptation, and cell survival. Thereby, hypoxia also influences tumour cell behaviour, promoting invasion, metastasis, and resistance to therapy [18], [19].

2.1.1.1 *The extracellular matrix*

The ECM provides physical stability and adhesion sites for cells and facilitates cellular processes, including proliferation, migration, and invasion. The ECM of most tissues consists of approximately 300 proteins. The main proteins are long filaments such as collagen, elastin and fibronectin, and non-fibre forming proteins like proteoglycans, glycoproteins and signalling molecules. These include chemokines, cytokines and growth factors, which bind to specific ECM proteins. Therefore, the ECM serves as an anchor point and reservoir of factors, regulating various cell functions such as growth, migration, protein synthesis and secretion [20]–[22]. In tumours, however, the composition and organization of the ECM is altered facilitating tumour cell migration, invasion, and angiogenesis. Thereby, abnormal ECM remodeling can create a permissive environment for tumour growth and metastasis.

Another important task of the ECM is to provide mechanical stability. The ECM can be described by mechanical properties, such as stiffness and viscoelastic behaviour, and by bulk metrics, e.g. pore size and average fibre length. The intrinsic fibre network also leads to a high degree of heterogeneity [20]. Fibrous proteins and their arrangement regulate the mechanical properties of the ECM. Most of the filaments tend to be stiff under tension but yield under compressive or tensile stress. Collagen exhibits a non-linear viscoelastic behaviour; hence, its mechanical properties are both time and strain-dependent [20], [23]. In contrast, elastin shows linear entropic elastic behaviour and can sustain high levels of strain without fracture. Proteoglycans can resist high compressive and tensile stress due to their high negative charge density and are essential in cartilaginous tissues [21].

2.1.1.2 *Cell-matrix interactions*

Cells constantly interact with their environment and the ECM surrounding them. Cells not only adhere and migrate on the ECM but also synthesise and degrade matrix proteins and thereby remodel their environment [24]. The mechanical properties of the ECM are regulated by the cells in the matrix. The cells can sense stress on the matrix via cell-matrix adhesion molecules, such as integrins, which link the ECM to the actin cytoskeleton of the cells. By synthesising or degrading matrix proteins and altering the extent of cross-linking between the fibres, cells are then able to respond to mechanical stimuli, change, and fine-tune the mechanical properties of their environment [21]. Important mechanical parameters are the stiffness/compliance and viscoelasticity [25],

[26] of the ECM, which influence proliferation, motility and differentiation processes [24]. It has been shown that stress relaxation impacts differentiation of mesenchymal stem cells (MSCs) [25] and cartilage formation of chondrocytes [26]. Stiffness affects neuronal outgrowth of PC12 neuronal cells [27], the nucleus and chromatin state of mammary epithelial cells regulating phenotypic changes [28], differentiation of MSCs [29] and C2C12 myoblasts [30] and the phenotype and ECM production of chondrocytes [31].

2.1.1.3 *Stiffness*

The extent to which an object resists deformation in response to an applied force is defined as stiffness. The stiffness of the ECM is an important feature that has a high impact on cell behaviour. Morphology [31], proliferation, cell adhesion [27], migration [32] and differentiation [29] processes may depend on the stiffness of the matrix [30]. The human body contains, among others, soft tissues, such as lung tissue with an elastic modulus in the range of 5 – 30 kPa [33], and substantially stiffer tissues, such as cartilage with an elastic modulus between 2 – 7 GPa [34], and bone with a modulus of about 15-20 GPa [35]. However, the stiffness differs between tissues and changes with age or disease conditions of the tissue. During cancer progression, e.g. in breast epithelial cells, the stiffness of the normal mammary gland increases from 150 Pa to more than 4,000 Pa [33].

Cells respond to changes in the stiffness, e.g. not only affecting focal adhesion and cytoskeleton formation of differentiated cells but also influencing differentiation processes. It has been shown that the differentiation of MSCs depends on the stiffness of the substrate they are growing on. Adipogenic differentiation was promoted by softer substrates and osteogenic differentiation by stiffer substrates [36]. To respond to changes in stiffness, cells have to sense the stiffness of their environment. It was demonstrated that MSC, which were cultured on soft hydrogels, can sense the underlying stiffer substrate up to a depth of five micrometres [37]. Furthermore, fibroblasts even migrated along stiffness gradients in the absence of chemical stimuli into a softer matrix, providing enhanced conditions for their survival and migration [32].

2.1.2 3D cell culture and hydrogels

2.1.2.1 3D cell culture

So far, the most common cell culture method, especially in drug and toxicity screenings, remains 2D monolayer culture performed on rigid plastic surfaces. The stiffness of standard tissue culture plates is in the range of gigapascal [24], which is much higher than the normal cell environment of most tissues. Cells cultured in monolayers exhibit a flattened cell shape, abnormal distribution of adhesion proteins on the cell surface and a forced polarity resulting in an aberrant phenotype and non-predictive data [38]. However, the high failure rate of potential drugs in animal studies and clinical trials demonstrates that 2D cell cultures do not properly represent physiological processes. When cells are cultured in 3D, multiple studies have shown that they mimic cell behaviour of living tissues and tumours more closely than cells cultured in 2D [39]–[43].

There are various methods for culturing cells in 3D such as spheroids that self-assemble in 3D culture, organoids that are 3D structures derived from patient-derived tumour cells or microfluidic devices enabling the precise control of culture conditions. Here, the focus lies on spheroids which can be cultured using scaffold-based and scaffold-free approaches. Scaffold-free approaches rely on the self-assembly of cells to form multicellular aggregates, which is facilitated by low-attachment plates or culture methods like the hanging drop [9], [10]. In low-attachment plates cells are seeded in non-adherent plates or dishes that prevent cell attachment, allowing them to self-aggregate and form spheroids. In the hanging drop method, droplets containing the cells are placed on the lid of a culture dish, which is then inverted, the cells aggregate and form spheroids due to gravity. It has been observed that the anticancer drug efficacy is reduced due to the three-dimensional structure and that tumour spheroids represent clinical tumours more closely than 2D monolayers [44]. However, it is crucial to mimic not only the 3D architecture but also the microenvironment and cell-matrix interactions. Scaffold-based 3D culturing techniques, therefore, offer a method to recreate the hydrophilic 3D network of the ECM by encapsulating cells in hydrogels or decellularised ECM-derived scaffolds. Here, cells are mixed with the hydrogel before gelation or seeded onto the scaffold.

2.1.2.2 Hydrogels

Hydrogels are a network of hydrophilic polymers, which are either naturally derived, of synthetic origin or a mixture of both. They can hold large amounts of water and share many similarities with native tissues. Hydrogels are highly tuneable and can be tailored greatly regarding their physicochemical properties and biochemical composition. Hence, they can closely mimic the 3D structure and biochemistry of the ECM. Therefore, hydrogels not only find application in 3D cell culture models [45], [46] and bioinks for biofabrication [47] but also in other areas of biomedicine, such as drug delivery [48], [49], tissue repair [50], wound healing [51], and medical devices [52]. Various polymers, as described below, are available to produce hydrogels varying in mechanical properties, such as stiffness and viscoelastic behaviour, pore size, biocompatibility, degradability, and the presence or absence of adhesion sites. This is particularly important because the mechanical properties of biomaterials are powerful regulators of cell and tissue function, mediating their intended function largely. For example, hydrogel matrix properties regulate proliferation [31], adhesion [27], migration [32] and differentiation [29] processes.

Two main groups of hydrogels used for 3D cell culture and tissue engineering: synthetic and naturally derived hydrogels. Synthetic hydrogels are chemically engineering such as polyacrylamides or polyethylene glycol (PEG). They are synthetic polymers with tuneable mechanical properties and the ability to be modified with various biologically active ligands and binding sites.

Naturally derived biomaterials are composed of macromolecules, originated from the ECM, or made of other biological materials, like alginate, which is derived from brown algae. Therefore, these materials are highly biocompatible but often suffer from batch-to-batch variations. Hydrogels based on native ECM proteins like collagen or fibronectin facilitate physiological cellular functions like proliferation, metabolism, motility, and differentiation. The structural proteins provide strength and elasticity of the matrices [2]. Several hydrogels are based on collagen, which is widely used as a hydrogel for cell culture since collagen is a major component of the native ECM and, therefore, provides cell adhesion sites and a native viscoelastic environment [38], [53]. Hyaluronic acid (HA) is also a natural component of many tissues, including skin, cartilage, and brain. It is commonly produced in industrial processes via bacterial fermentation or derived from animal products. Thus, it is chemically tuneable, can be

modified with adhesive ligands and is often used for tissue engineering and drug delivery applications [38].

Matrigel® is a commercially available basement membrane hydrogel extracted from Engelbreth-Holm-Swarm (EHS) mouse sarcoma tumours, containing a complex mixture of type IV collagen, laminin, proteoglycans and growth factors. Due to its tumour growth and angiogenesis promoting characteristics, Matrigel® has been widely used in 3D cell cultures and is commonly regarded as the current ‘gold standard’. However, as with other naturally derived hydrogels, it suffers from batch-to-batch variations, poor control over physicochemical properties, and a lack of standardisation, collectively contributing to limited experimental reproducibility. Furthermore, due to its inconsistent properties [53] and undefined composition, it is difficult to identify the factors promoting specific signals and cellular functions [2]. In addition, incorporating Matrigel® in high-throughput screenings is challenging due to its need for cooling and lack of control over physicochemical properties, which are dependent on temperature [24].

Other collagenous hydrogels are based on gelatin, which contains partially hydrolysed collagens and other proteins of the ECM like proteoglycans, glycoproteins, elastin and glycosaminoglycans. Therefore, these hydrogels are highly bio- and cytocompatible, degradable and provide adhesion sites.

Another important group of hydrogels that are commonly used for biomimetic 3D cancer models are photopolymerisable gels. In contrast to other crosslinking methods such as ionotropic gelation, these hydrogels can undergo a gelation process upon exposure to light, typically UV light, but also light with longer wavelengths, depending on the utilized photo-initiator. The photopolymerisation process allows for precise spatial and temporal control over gel formation, enabling the creation of complex 3D structures with high resolution and fidelity. This capability facilitates the precise positioning of cancer cells and other components within the hydrogel, enabling the construction of well-defined tumour architectures. However, the cytocompatibility of photopolymerisable hydrogels can be affected by factors such as the exposure duration and intensity of irradiation and the exposure to cytotoxic free radicals of the photo-initiator [54], [55].

One example of photopolymerisable hydrogels are gelatin methacryloyl (GelMA) hydrogels based on gelatin, which has been functionalised with methacryloyl

groups to improve the stability and reproducibility of gelatin hydrogels, still providing cell adhesion and matrix metalloproteinases (MMP) cleavage sites. Cell adhesion receptors can bind to GelMA, while proteases secreted by the cells can degrade the hydrogel [45]. GelMA can be reversibly crosslinked by thermal gelation and covalently by photo-crosslinking. GelMA is thermally crosslinked at low temperatures, resulting in a stiff hydrogel. Increasing temperature up to 37°C reverses this crosslinking process and decreases its viscosity, thus facilitating pipetting and its use with robotic liquid handlers. The methacryloyl groups can be covalently crosslinked via a photo-initiated polymerisation [56]. This crosslinking reaction enables tuneable properties of GelMA. The mechanical properties can be tuned by variation of the polymer concentration and crosslinking parameters, like photo-initiator concentration, light exposure time and intensity [57], [58]. O'Connell et al. described photo-crosslinking rates for GelMA as dependent on the light intensity, exposure time and photo-initiator. They used 2-hydroxy-40-(2-hydroxyethoxy)-2-methylpropiophenone (Irgacure-2959) as a photo-initiator and UV light with a wavelength of 365 nm [57]. However, photo-crosslinking conditions differ from various photo-initiators, each in conjunction with multiple wavelengths, light intensity, and general experimental set-ups, such as utilised moulds and hydrogel volumes, each influencing the physical properties of the resulting hydrogel. More recently developed photo-initiators, such as lithium phenyl(2,4,6-trimethylbenzoyl) phosphinate (LAP) [59]–[61] or eosin Y in combination with triethanolamine (TEA), and 1-vinyl-2 pyrrolidinone (NVP) [62], [63], have also been employed for photo-crosslinking. These photo-initiators are commonly activated by visible light with a wavelength of 400 nm and 460 nm, respectively, which has been shown to be less cell-damaging than light of shorter wavelengths such as UV light used in conjunction with Irgacure-2959 [63]–[65]. Furthermore, the photo-initiator used and its concentration can also influence pore size [59] and the mechanical properties of the resulting hydrogels [57].

The ability to tune the stiffness of GelMA is a crucial feature because spheroid formation, adhesion and cell viability are dependent on the matrix stiffness [27], [45]. These tuneable mechanical properties permit its use in various cell types, preferring different kinds of stiffness, and replicate pathophysiological changes to the physicochemical properties of the ECM, such as they occur during cancer initiation

and progression. GelMA is also suitable for drug screenings and automation applications because the semi-synthetic origin allows reproducible production of hydrogels with comparable physical properties [45].

Table 2.1: Advantages and disadvantages of GelMA being used for *vitro* 3D models and the automated fabrication process

	Advantage	Disadvantage
Use for <i>in vitro</i> 3D models	<ul style="list-style-type: none"> • High biocompatibility • Tunable mechanical properties • Degradability 	<ul style="list-style-type: none"> • Batch variability • Higher costs • Gelation is sensitive to environmental conditions
Use for automated fabrication process	<ul style="list-style-type: none"> • Less viscous at higher temperatures • Scalability 	<ul style="list-style-type: none"> • (light) crosslinking and temperature control needed

2.1.3 Applications of 3D cell culture systems

2D cell culture is still widely used for drug and toxicity screenings because of its ease of use, well-established methods and bioassays, which are compatible with high-throughput systems. Cells grow easily on inexpensive standard tissue culture plates compatible with a range of automated devices from liquid handling to automated imaging and analysis. Cell biological methods, such as transfections, protein expression and drug treatments, as well as protein-, RNA, or DNA extraction, are relatively simple, and the evaluation of cytotoxicity is standardised and repeatable [66]. However, the inaccurate representation of physiological behaviour in 2D cell cultures leads to imprecise results, which do not necessarily reflect the *in vivo* behaviour. The rigid plastic surface of tissue culture plates leads to polarising of the cells and an increased exchange area to culture media. Therefore, the cells experience overexposure to nutrients and oxygen, which do not reflect *in vivo* molecular gradients. The high tensile stress also stimulates high proliferation rates [67]. Due to the 2D environment, cell-cell interactions are limited, which modifies gene expression and the extracellular matrix composition.

Aside from differences in morphology between 2D and 3D cultures, it has been shown that monolayers of cells are hypersensitive to anti-cancer drugs [9], [39], [68], [69]. The absence of a physical barrier between applied drugs and the cells can lead to overexposure to anti-cancer drugs [66]. The high proliferation rates, stimulated by an

increased cell tension, impact the sensitivity of cells to anti-cancer drugs [39]. Overcoming these drawbacks of conventional 2D cell culture, 3D cell culture can be used to mimic tumours more accurately, including cell-cell and cell-matrix interactions, as well as metabolic gradients [44]. Geno- and phenotype are altered in 3D compared to conventional 2D monolayers, showing more similarities between 3D spheroids and *in vivo* conditions. This results in an enhanced predictive value of pharmacological responses of 3D tumour models compared to 2D cell cultures [39], [70]. Mosaad et al. showed that 3D prostate cancer spheroids are less sensitive to docetaxel and Abiraterone Acetate than 2D monolayers, and even the recovery of the cells after repeated drug treatment was increased in the spheroids [39].

Despite the more accurate representation of physiological characteristics of 3D tumour models, they are still not the standard in high-throughput screenings (HTS). A literature search on PubMed revealed that in 2021 892 out of 1999 publications involved 3D cell culture models (Figure 2.1). Indeed, the number of drug screening studies on 3D models increases from year to year, but only less than a fifth of these studies included automation or high-throughput technologies in 2021 (Figure 2.1 B).

Various assays are used on 3D cell cultures in drug discovery and testing to assess the efficacy and potential toxicity of drug. These assays provide valuable insights into the response of cancer cells within the 3D context, allowing for more accurate predictions of drug behaviour compared to traditional 2D cell culture models. Some commonly employed assays for drug testing in 3D cancer models not only include cell viability assays to measure the overall viability in response to drug treatments [71] but also apoptosis, cell migration and invasion assays [72]. In addition, changes in gene expression profiles using quantitative real-time polymerase chain reaction (qPCR) are assessed [73] and specific proteins are visualized and quantified employing immunofluorescence techniques [74]. And, with the help of confocal and multiphoton microscopy the distribution and morphology of cells and spheroids can be visualized and analysed [75].

However, most of the existing manufacturing processes and analytical tools are not compatible with high-throughput methods for 3D cell cultures, e.g. the addition of drugs or exchange of medium can result in displacement of the micro-tumours when low-attachment microplates are used to form spheroids [39]. In addition, current HTS systems cannot handle viscous liquids and photo-crosslinking of hydrogels. So far, 3D

cell cultures have been used for small-scale experiments with single endpoint measurements, which also do not allow monitoring the real-time effect of applied drugs on 3D spheroids [70]. However, the reproducibility of drug screenings in 3D cell culture is low due to the heterogeneity in the growth behaviour of the spheroids and lower cell numbers. Phenotypic analysis can cope with these problems because it allows normalisation to cell or object numbers and can additionally capture the complexity of 3D spheroids [76].

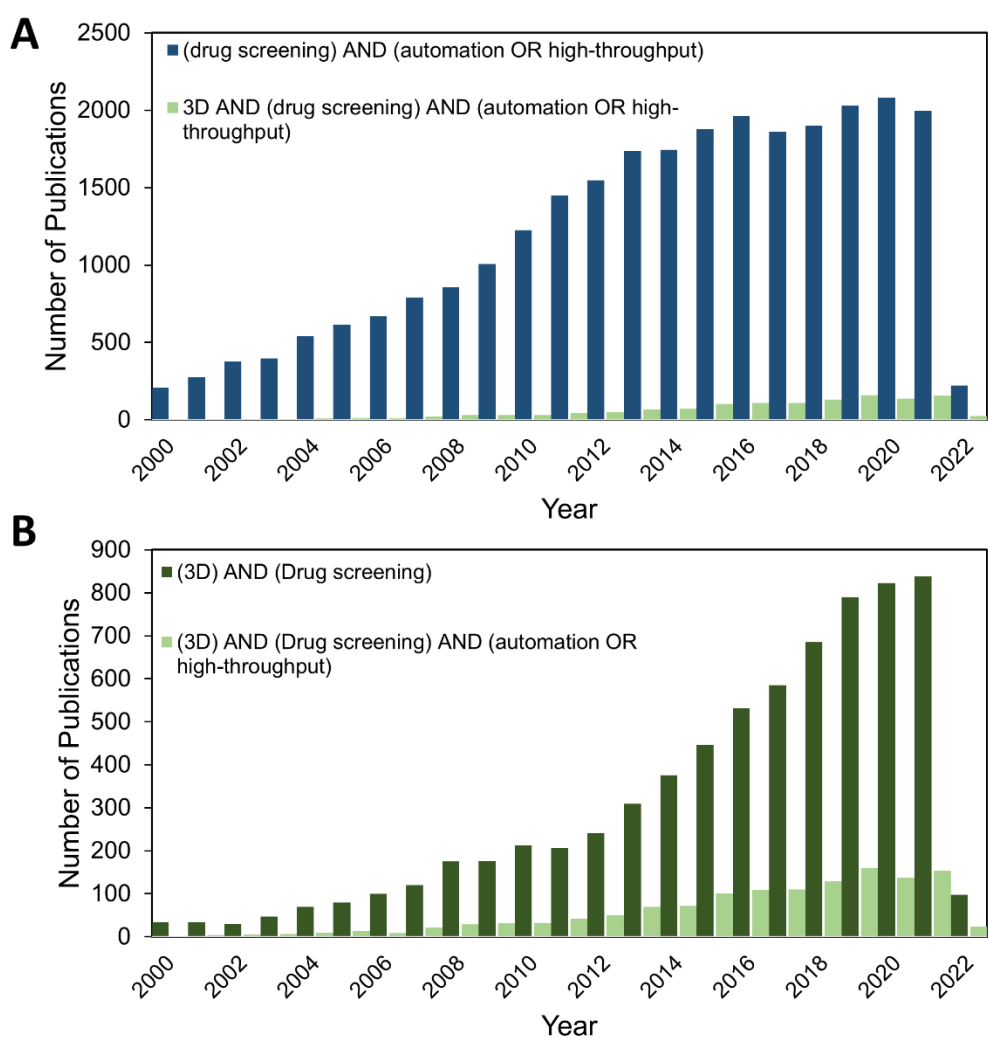


Figure 2.1 Literature search on 3D drug screenings

(A) The number of publications per year published about drug screenings in general ((drug screening) AND (Automation OR high-throughput)) and specifically on 3D drug screenings (3D AND (drug screening) AND (automation OR high-throughput)) (B) The number of publications per year on automated or high-throughput 3D drug screenings ((3D) AND (Drug screening)) and automated or high-throughput drug screenings on 3D models ((3D) AND (Drug screening) AND (automation OR high-throughput)) (PubMed Search performed on 10/02/2022).

2.2 LABORATORY AUTOMATION TECHNOLOGY

2.2.1 Automation in the life sciences

Automation is not only reasonable in large-scale industries, such as automotive or logistics, but also in a life sciences laboratory environment, as it has been already implemented, e.g. in high-throughput screenings, synthetic biology, combinatorial chemistry or quality control laboratories [77]. Although automation has initially high investment costs, in the long run, it is not only more cost-effective but also ensures more reproducible results, and hence, reduces user-bias. Especially complex workflows and processes are time- and labour-intensive and, therefore, dependent on the experimenter performing the task. On the contrary, automation is largely user-independent, ensures accuracy and precision and can increase the throughput while keeping the labour investment for the user relatively low [78].

Automated laboratory equipment can take over a variety of tasks, from automating specific repetitive tasks, like pipetting and analysing samples, and partial automation, like plate-handling workstations, to total laboratory automation, where different analysers and other devices are connected via robotic arms or arranged in assembly lines to automate whole workflows covering several process steps such as moving plates, pipetting and changing media. With a higher degree of automation, the efficiency and quality of testing can be improved; the sample volume can be reduced and also the biological risk for operators can be minimised [78].

In HTS, automation is part of all steps involved. Starting with the assay design and development, when identifying the target and assay parameters, a robust and reproducible assay format suitable for HTS needs to be designed and developed as well. Cell culture steps, such as seeding and media change, and compound addition are automated with liquid handling systems. An automated transfer to environmental controlled chamber ensures controlled incubation conditions. Depending on the type of assay and required readout, various instruments such as plate reads, imaging systems or automated microscopes automate the data acquisition. Afterwards automated image processing and data analysis steps for hit identification, dose-response analysis, and data visualization are necessary.

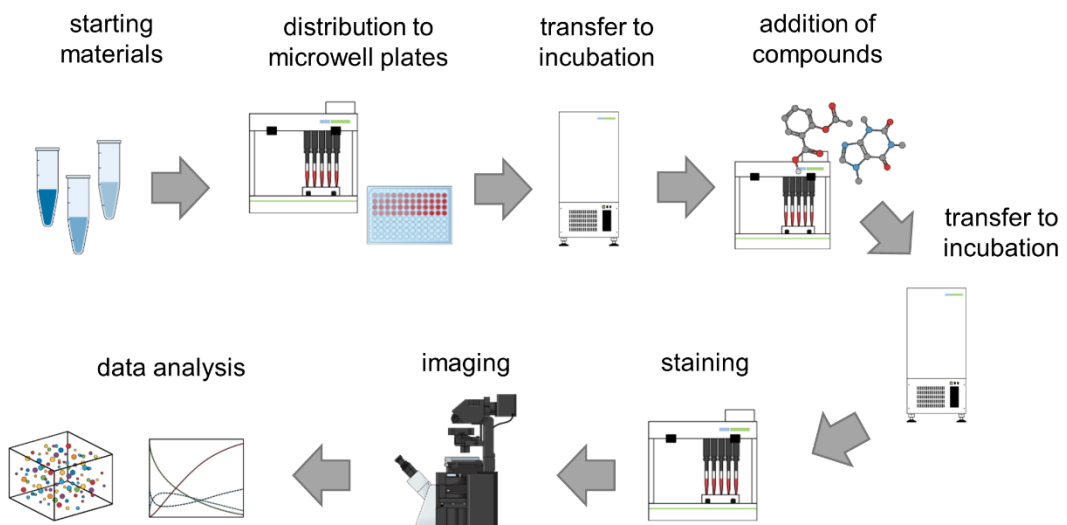


Figure 2.2: **General workflow of a HTS**

The starting materials, including cells and cell culture medium, are distributed to microwell plates using liquid handling robots. Once the plates are prepared, they are transferred to an incubation chamber. In the next stage, compounds of interest are automatically added to the wells in the microwell plates. Depending on the specific assay type being performed, an additional incubation step might be required before further processing. After the necessary incubation periods, the samples are ready for automated staining and imaging using dedicated equipment. Finally, the acquired data is analysed using computational methods or specialized software.

Nevertheless shifting von manual to automated workflows involves not only integrating more advanced equipment and technology but also requires adaptions of methods and techniques. Special attention must be given to critical processing steps such as centrifugation and subsequent transfer of the supernatant, dissolving cell pellets, or mixing viscous solutions that may require modified protocols or specialized equipment in automated workflows.

Liquid handling

A common device for automation in life science is the robotic liquid handler since pipetting tasks must be fulfilled in almost every laboratory situation. For a higher degree of automation, liquid handlers can be connected to plate washers, sealers and plate readers, incubators and other devices [79]. Liquid handlers are used in various research settings, such as gene sequencing, protein crystallisation, antibody testing and drug screening, and everywhere else where high accuracy and precision with a high-throughput aspect to a low volume of samples is required. These tasks would be

tedious, time-consuming or even impossible if performed manually. Therefore, a wide variety of liquid handler and pipetting robots is commercially available.

In general, liquid handlers consist of a control centre, single- or multichannel pipettes with fixed or disposable tips, a washing station and a deck holding space for microwell-plates. Via robotic arms, liquid plate handlers can be connected to automated incubators and plate readers for analysis.

Commercially available liquid handlers are often restricted in their application. They do not allow changes to the hard- and software, which might be needed if they are used in research institutions with various projects. However, there are some open-source projects. Barthels et al. [80] developed an open-source liquid-handling workstation, which can be 3D-printed for less than \$400. It provides reliable and flexible dispensing with low pipetting errors. Another open-source pipetting robot is the OT-1 from OpenTrons, which is commercially available and with costs of US\$4,000 still more affordable for academic research institutions than other high-end liquid-handling workstations, which can cost more than US\$30,000.

2.2.2 Automation of 3D cell cultures

Automated workflows are already standard for 2D cell cultures in drug discovery and drug screenings; typically tasks such as moving plates, pipetting, changing media, and imaging are automated. Automation systems for 2D cell cultures often rely on robotic arms, liquid handling systems, and plate-handling devices. These systems are designed to carry out repetitive tasks with precision and efficiency.

However, when transitioning to 3D cell cultures, additional considerations and challenges arise. The underlying materials such as hydrogels require the handling of viscous solutions, which is challenging for most automated liquid handling systems. Additional processing steps such as hydrogel preparation steps and crosslinking with light are necessary and cell culture steps such as cell seeding and media change become more complex. Hence, most of the current technology is not yet adapted and compatible with 3D cell culture techniques. Standardised and reproducible methods are still missing. 3D cultures often require the handling of viscous hydrogels, have to be kept at a specific temperature [81] and require specific handling since they adhere more to the tools and droplet release may take longer. Many liquid handling systems

cannot handle these materials since their pipettes are not suitable for viscous materials, and heating systems are missing [76].

Nevertheless, there are some approaches to automate 3D cell culture. One commercial system suitable for high-throughput production of 3D cell cultures is RASTRUM™ (Inventia Life Science Pty Ltd., Alexandria NSW, Australia), which uses a droplet-based approach to place cell-laden hydrogels into tissue culture microplates [82]. Scaffold-free 3D cell cultures based on suspension media and low-attachment plates can be conveniently automated, as was done by Monjaret et al. [6]. Spheroids of different cancer cell lines were automatically produced with a Freedom EVO 150 workstation (Tecan, Männedorf, Switzerland) on micro-patterned 96 microwell plates with subsequent drug exposure and dose-response experiments. Rimann et al. [83] automated a hydrogel-based 3D cell culture system and subsequent drug screening using a Freedom EVO liquid-handling robot. The whole process of embedding human colon carcinoma cells in dextran-based hydrogels, gelation of the gels, adding drugs and testing for viability and DNA content was automated. The authors demonstrated that the production of this 3D cell culture system was adaptable to the liquid handling platform, and results were reproducible.

2.2.3 Biomanufacturing workstation

A biomanufacturing platform has been developed by Eggert et al. incorporating a pipetting, crosslinking, storage and a transportation module to move multiwell plates between the individual workstation units (Figure 2.3) to address the needs for the automated production of hydrogel-based 3D cell cultures [16], [17].

The pipetting module (Figure 2.3 A) is based on the liquid handling robot OT-1 from Opentrons and can be operated by a python-based application programming interface (API) [84]. The pipetting robot enables automated liquid aspiration, dispensing and mixing tasks. The pipetting module (Figure 2.3 B) has been modified for handling viscous and non-viscous materials by exchanging the standard air-cushion pipettes with positive displacement pipettes. Additionally, two temperature docks were integrated into the pipetting module, with temperature control ranging from 5.5°C to 95°C. This feature allows the processing of thermoresponsive hydrogel precursor solutions, such as GelMA, Matrigel and collagen, and pre-warming of solutions for cell culture workflows, such as media and buffers. The pipetting module can be

equipped with two pipettes, either two single pipettes or one single channel and one 8-channel pipette, and up to eight containers.

The crosslinking module (Figure 2.3 C) holds a light-emitting diode (LED) panel for photo-crosslinking hydrogels. The LED panel is based on a plug-and-play system allowing a quick exchange of the LED panel to integrate LEDs with a different wavelength. The intensity of the light can be regulated by adjusting the distance of the light or by varying the voltage intensity using pulse-width modulation (PWM). A light intensity of up to 4 mW cm^{-2} can be reached at full maximum. In addition, the crosslinking module contains a sliding mask allowing the creation of exposure gradients in one well plate.

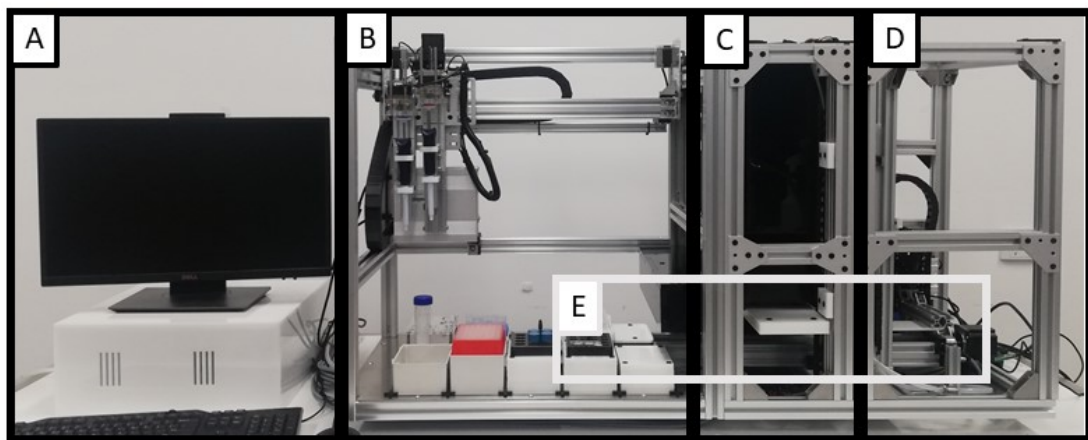


Figure 2.3 **Biomanufacturing workstation**

(A) Control unit. (B) Pipetting module with positive displacement pipettes and heating blocks. (C). Crosslinking module. (D). Storage module including a lid lifter. (E) Transportation module connecting the pipetting, crosslinking and storage module (adapted from Eggert et al [16]).

The storage module (Figure 2.3 D) holds up to six tissue culture plates to increase the overall sample throughput. An integrated plate mover transports the plates from the storage rack on the transportation module and back. A lid lifter using vacuum suction cups ensures that the lid of the well plate is closed before being stored. A transportation module (Figure 2.3 E) connects the three modules, facilitating automated production of hydrogels, distributing to tissue culture plates, crosslinking and further processing with one protocol. The complete biomanufacturing workstation fits into a standard biosafety cabinet class 2, ensuring a sterile environment and enabling the work with cell cultures.

The crosslinking, storage and transportation module are based on linear stages and can be controlled via G-Code. The code can be combined with Opentron's API of the pipetting module to allow operating the whole biomanufacturing workstation with one python-based script. Additionally, a custom-designed graphical user interface (GUI), called 'Protocol Design App', guides the user through the parameter selection process.

2.3 AUTOMATED MICROSCOPY SYSTEMS

2.3.1 Fluorescence microscopy

Fluorescence microscopy is a well-established and powerful tool used in biochemistry, molecular and cell biology. It offers a variety of analysis methods from simultaneous imaging of different cellular, subcellular or molecular components to monitor chemical environments. Various image analysis measurements and descriptors can be used to extract quantitative information about the cells and their spatial arrangement based on different fluorescent staining techniques. These descriptors include the area, quantifying the size of individual cells or clusters in the image and providing information about cell growth, expansion or changes in cell size over time, the perimeter providing insights into cell shape and cell-cell adhesion and the diameter to determine cell size and uniformity within a cell population. Other parameters are the solidity, quantifying the compactness of a cell or cell cluster and thereby useful for studying cell spreading or cell-cell contacts, and the intensity measurements, which capture the intensity values of pixels or regions of interest in the image. The volume and surface area are particularly relevant for 3D cell cultures as they quantify the size and shape of individual cells or cell aggregates, allowing the analysis of cell growth, spheroid formation, or invasion [85]. Protein components of living systems can be tagged with fluorescent reporter molecules; hence, the production and distribution of proteins and other molecules can be observed within a living cell. Changes in pH, calcium ions, adenosine triphosphate (ATP) or other second messenger concentrations can be identified or even quantitatively measured with ratiometric assays [86]. Hence, fluorescence imaging has become an indispensable technique and offers a wide range of applications in biology and biomedical sciences.

2.3.1.1 Fluorescence fundamentals

The underlying principle of fluorescence is the emission of light of longer wavelengths after the absorption of light by certain molecules called fluorophores. The first stage of fluorescence is the excitation of the fluorophore with light of a certain wavelength. Electrons are boosted from the ground state S_0 into a different orbital of the molecule creating excited singlet states, e.g. S_1 and S_2 , as illustrated in the Jablonski diagram (Figure 2.4 A). The singlet state S_2 contains more energy than S_1 , and S_1 contains more energy than the ground state S_0 . The molecule returns to the ground state from the excited state using several different pathways, such as internal conversion and vibrational relaxation, to dissipate the absorbed energy. Typically, internal conversion and vibrational relaxation bring the molecule from S_2 to the lowest energy level of S_1 . An expulsion of a photon returns the fluorophore from S_1 back to the ground state.

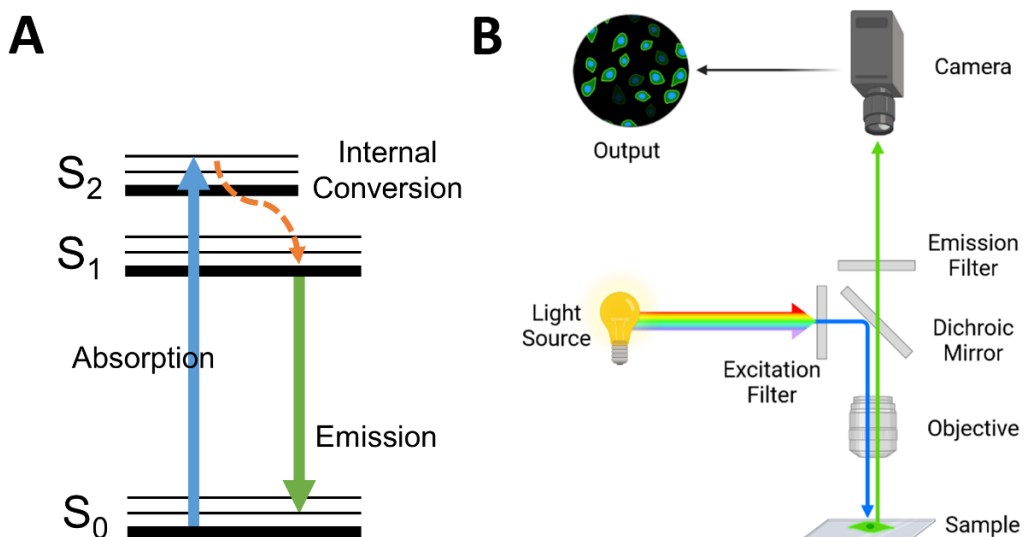


Figure 2.4 Fluorescence principle

(A) Simplified Jablonski diagram for fluorescence. Electrons of a fluorophore are boosted from the ground state S_0 into an excited singlet state, e.g. S_2 . The electron dissipates the absorbed energy through different pathways, e.g. internal conversion, which brings the electron to a lower excited state S_1 . From there, it returns to the ground state S_0 , emitting light of longer wavelengths. (B) Lightpath of a fluorescence microscope. The excitation filter blocks unwanted light emitted from the illumination source. The excitation light (blue), required to excite the fluorophore, is reflected by the dichroic mirror and focused by the objective onto the specimen. The fluorophore emits light of longer wavelengths (green), which is collected by the objective. The emission light passes through the dichroic mirror and emission filter onto the camera sensor (created with BioRender.com).

The energy of an emitted photon is lower, thereby having a longer wavelength, than the exciting photon, which has a shorter wavelength, due to energy dissipation during the excited state, known as the Stokes shift. This Stokes shift is fundamental to fluorescence imaging because the fluorescence signal can be detected by filtering out the excitation light without blocking the emitted light [86].

2.3.1.2 *Fluorescence microscope*

Similar to a basic transmission light microscope, a fluorescence microscope uses an objective, which collects the light from the sample and focuses it through a group of lenses onto the eye of the viewer or, in digital microscopes, onto a camera sensor. But, instead of trans-illumination, fluorescence microscopes commonly use epi-illumination. Here, the objective not only images and magnifies the specimen but also serves as a condenser illuminating the specimen and focussing the excitation light to the sample to warrant a high energy density. The light required to excite the fluorophore passes through an excitation filter blocking unwanted light from the illumination source. Then, it is reflected by a dichroic mirror and focused on the specimen by the objective. The light emitted by the fluorophore in the specimen is collected by the objective and passes through the dichroic mirror, which transmits the light for longer wavelengths. An emission filter blocks any shorter or longer wavelength to minimise background noise. Then, the light is focused by a tube lens onto the camera sensor.

Illumination

More and more microscopes use LEDs as the source of illumination, but mercury and xenon arc lamps are still common as well. The development of LEDs within the last years has overcome their disadvantages, such as low intensity and limited selection of wavelengths [87], so that LEDs increasingly replace arc lamps. Nowadays, LEDs are available in almost any wavelength throughout the ultraviolet (UV), visible light and near-infrared (NIR) spectrum.

Due to their longer lifetime, LEDs are more energy- and cost-efficient than a mercury bulb. Additionally, LEDs do not require any warm-up time to reach thermal equilibrium or cool-down time. They have a small footprint and low power consumption, making them ideal for portable microscopes. Visible light LEDs emit almost no UV or infrared (IR) radiation, minimising toxicity and heating of samples. Furthermore, LED emission is stable and reproducible, simplifying background

correction and comparison of image brightness between different samples [88]. Additionally, the controllability of LEDs comes with many advantages. LEDs can be switched on and off within milliseconds, eliminating the need for a mechanical shutter and thereby minimising vibrations. The excitation light can be synchronised with the acquisition of images with a camera, reducing phototoxicity and improving the temporal resolution of experiments [88]–[91]. However, due to the narrow bandwidth of LEDs, researchers need to understand the concept of fluorescence and LED illumination better to choose the correct optical filters [87]. Additionally, when designing an LED control system, attention must be paid to the LED's output power, peak wavelength, emission spectrum and voltage characteristics as they depend on the applied current and temperature of the LED. Furthermore, due to differences in manufacturing and inhomogeneities in the raw materials, LEDs of the same model can vary in their forward voltage drop [90].

Filter

In a fluorescence microscope, the setup of optical filters is a crucial element since it separates the emission from the excitation light and the wanted from the unwanted wavelength bins. Typically, a fluorescence filter setup consists of a filter cube with a dichroic mirror and an emission filter. The excitation filter has a narrow transmission band, which only allows the light source's wavelengths to pass, which excite the fluorophore. The excitation light is reflected by the dichroic mirror positioned at a 45° angle to the excitation filter. Dichroic mirrors are defined by a cut-off wavelength; the mirror reflects light whose wavelengths are below the cut-off and transmits wavelength above this value. Thereby it separates the excitation light from the emission light. The emission filter permits only light of the desired wavelength bin emitted by the fluorophore to pass and blocks unwanted traces of excitation to minimise background noise. This described setup with dichroic mirror, excitation and emission filter is specific for one kind of fluorophore, e.g. GFP, TRITC, etc. Thereby the whole filter cube needs to be changed in order to image another fluorophore. In a commercial microscope, three to nine of such filter cubes are fitted into a circular carousel or linear block so that the position of the filter cubes can be changed either manually or by a computer-driven motor. However, due to the change of whole filter cubes, the filter might be perfectly aligned, especially the dichroic mirror, and care must be taken when overlapping two images of different cubes. Therefore, other

systems use a more sophisticated dichroic mirror in combination with filter wheels, allowing rapid switching between different filter setups. These dichroic mirrors can have up to four bandwidths reflecting and transmitting, respectively fluorophores [86].

2.3.1.3 *Fluorescence microscopy and HCS for 3D cell culture*

High-content screening (HCS) combines high-throughput technologies and cellular imaging for phenotypic multiparametric data acquisition [3]. Phenotypic profiling plays a vital role in drug discovery because it leads to a high percentage of FDA-approved drugs and provides more biologically relevant information than conventional molecular assays [92], [93]. HCS enables parallel imaging of multiple cell parameters and offers a variety of possible screenings from fluorescent reporter genes to protein localisation and complex morphological assays [94]. Compared to high-resolution imaging techniques, the focus is more on low resolution, enabling high numbers of observations and saving time. Transmitted light can be used to determine the spheroid size and density. In addition, a variety of fluorescence dyes can be employed, e.g. viability, DNA-binding and apoptosis dyes or other fluorescence markers, to detect various morphological features [14].

HCS is widely adapted in 2D cell cultures, offering a broad spectrum of readouts with a single measurement. However, in 3D cell-based assays, HCS remains challenging regarding imaging, image analysis, computation, data storage and visualisation [76]. Overcoming these challenges, the high-content analysis also offers an increased potential to extract more information from the increased complexity of phenotypes of 3D tumour models [72]. Furthermore, no disruption of spheroids is required with image-based analysis, and various readouts with one measurement are possible [14]. Microscope manufacturers are already aware of this, offering a wide range of high-content imaging systems (Appendix A), facilitating 3D imaging by confocal technologies or widefield fluorescence optics combined with other image analysis tools like deconvolution.

Several studies have already shown the implementation of the 3D cell culture technique to HCS. A common method is to use low-attachment round-bottom plates, as their workflow is simple and compatible with standard liquid handlers and high-content imaging systems [14]. A high-content assay for 3D cancer spheroid cultures has been developed to screen a library of 119 anticancer drugs. 3D spheroid formation of colon cancer cells was facilitated in low adhesion U-bottom plates, followed by a

one-step staining protocol optimised for spheroid culture and imaging using a confocal spinning disk as well as a widefield HCl system [14]. Monjaret et al. [6] used micro-patterned well-plates to fully automate the production and screening of 3D tumour spheroids. Standard liquid handling systems were capable of producing scaffold-free spheroids, which were imaged by a widefield fluorescence high-content imaging system. Another approach, which has been used for 3D HCS, is the overlay technique, where cells are seeded on top of a layer of hydrogel. To study dose-dependent cytotoxicity, growth inhibition, and size-dependent response of different treatments, ovarian and pancreatic cancer cells have been seeded on Matrigel® to create quasi-3D tumour models. The spheroids were stained with Alexa Fluor 488/DAPI for confocal immunofluorescence imaging and live/dead staining for fluorescence imaging [81]. In another study, multicellular tumour spheroids were created by a liquid overlay technique to identify nine substances out of two commercially available drug libraries specifically targeting the inner core of the spheroids. For the HCS, the 3D tumour models' all nuclei and dead cells were stained and imaged in widefield fluorescence mode to quantify the inner core cell death by capturing one image per spheroid focused on the spheroids' centre [95].

However, scaffold-free and scaffold-based techniques have been already employed for HCS. Prostate cancer cells were cultured in Matrigel® in standard 384-multiwell plates to study the drug response of 80 potential inhibitors using over 800 phenotypic parameters imaged with an inverted fluorescence microscope [72]. To profile 598 parameters in a HCS, human breast cancer cells were cultured in a mixture of collagen and Matrigel® and imaged with a widefield microscope to increase the imaging process [96]. In conclusion, HCS has been proven to be feasible for 3D cell cultures and to offer many possibilities to study cell behaviour and drug effects in 3D tumour models.

2.3.2 Open-source microscopes

In addition to commercial microscopes, the scientific community has developed several open-source and low-cost microscopes. There is a wide range of microscopes, each developed for a different purpose. There are low-cost systems to be used in educational settings and scientific clinical applications in low-income countries [97], [98]. Other systems aim for certain applications, such as for the use in conventional tissue culture incubators [99] or for neurogenetics experiments [100]. However, most

of the developed systems offer a low-cost and modifiable alternative to commercial systems [101]–[103].

Diederich et al. [101] developed a modular microscopy toolbox made from 3D-printed components. It offers brightfield and fluorescence imaging modes and can also be transformed into a light sheet fluorescence microscope. The setup is made of optical building blocks, which can be rearranged to adapt to different needs, e.g. a brightfield microscope for long-term incubator enclosed in-vitro imaging, conversion into a cell-phone microscope or light-sheet microscope. However, a motorised stage and automated sample positioning are missing.

Other systems, like the OpenFlexure microscope [97], include trans- and epifluorescence imaging and motorised sample positioning and focus control. However, due to the microscope's compact size, its travel range is limited to 12 mm x 12 mm x 4 mm and, hence, does not allow scanning of whole microwell plates or tissue culture flasks. Another approach is integrating an actual 3D stage, described by Wijnen et al. [102]. They converted a RepRap 3D printer into an XYZ-stage and combined it with a USB microscope with accuracy and repeatability below conventional 2D microscope stages, but still sufficient for many scientific applications. Similar to this, the motion control system for the “Incubot”, a microscope fitting into a conventional tissue culture incubator, is based on a cartesian 3D printer as well [99]. The “Incubot” is a low-cost reflected, oblique and fluorescence imaging system based on 3D printed components and standard optical elements, such as a commercial infinite-conjugate objective lens and an achromatic doublet lens used as a tube lens. Images are taken with a Raspberry Pi Camera V2, connected to a Raspberry Pi computer that is also used for software integration. Fluorescence imaging of GFP is realised with inexpensive five-millimetre diameter LEDs.

The “Microscopi” is an inverted brightfield and fluorescence microscope, in a small and robust design, incorporating a motorised XY flexure stage and Z-objective lifter for focusing [98]. The XY flexure stage enables easy horizontal navigation through the sample and generation of composite images made of up to 5x5 panel views. The Microscopi comes with a web-based graphical user interface to be used on desktop computers and mobile devices, allowing to operate the microscope from a distance.

XYZ-stages

In order to provide a low-cost open-source alternative to expensive microscope stages, a 3D printed motorised XY positioning stage was developed by Schneidereit et al., enabling high-content screenings with a conventional inverted fluorescence microscope [104]. The presented study integrated the positioning stage into a previously custom-built imaging robot for automated functional Cl⁻ and Ca²⁺ high-content imaging in a 96-well format. The system is lightweight, portable and easy to reconstruct. However, the 3D printed components are not as durable as machined components using more robust materials. Additionally, the positioning stage did not include a Z-axis to enable Z-stacking or a robotic gripper for the automated exchange of tissue culture plates.

To address automated positioning of samples, either for microscopy or applications in neurophysiology, Campbell et al. developed an XYZ positioning system based on 3D printer components resembling a gantry crane [105]. Hence, unlike conventional microscopy stages, their system had rather large working dimensions (430 mm x 430 mm x 150 mm).

2.4 SUMMARY AND IMPLICATIONS

3D cell culture is already widely accepted to “bridge the gap” between 2D cell culture and animal models, but there are still challenges for their implementation in drug discovery and screening processes [66], [83]. Given the FDA Modernization Act 2.0, signed on December 29, 2022, alternatives to animal testing, such as organoids and organ-on-a-chip systems, are now allowed to prove the safety of drug and biological products, which will increase the demand of 3D cell culture models. Thereby, it has been officially recognized that cell-based alternatives can potentially deliver more accurate results than animal testing [106]. Nevertheless, so far, the throughput of 3D tumour models used for drug screenings is low, and most of them were used with small-scale end-point assays and single readouts, not exploiting the full potential and complexity of 3D tumour models [70], [76]. However, multiple readouts and real-time monitoring are necessary to better understand the effects of drugs on 3D spheroids. In order to increase the throughput, 3D culture systems must be compatible with liquid handling and high-content screening systems.

Challenges remain in automated liquid handling of viscous materials. Temperature control of hydrogel is crucial to allow liquid handling, precise pipetting, and avoid thermal gelation [2], [11]. Image acquisition is a critical component to enable multiple readouts. Care must be taken to find the right balance between optical resolution and acquisition time. Solutions for complex image processing, such as removal of background, scaling of fluorescence signals and segmentation, and analysis, are required [72], [81].

Altogether, 3D drug screening platforms and standardised methodologies are needed, which ensure reproducibility and are versatile enough to enter mainstream drug discovery [11], [72]. Hence, this PhD project provides an open-source-based biomanufacturing and automated imaging platform for 3D cell culture systems to accelerate this process and implement 3D culture systems in drug screenings. Optimisation and validation of automated workflows for biomanufacturing ensure reproducibility, and the implementation of an environmentally controlled imaging module permits real-time monitoring and drug screenings on scaffold-based 3D tumour models.

2.4.1 Requirements for the opto-mechatronic screening module

A new module is required to expand the biomanufacturing workstation, described in section 2.2.3, and enable the automated production of hydrogel-based 3D cell cultures and their analysis. Similar to the assembly line approach of the workstation, the module should follow an open-source and low-cost approach and be capable of being fully integrated, both hardware and software, into the workstation. Based on the findings in the literature, the new module must fulfil several requirements:

The microscope should be capable of imaging cell population in a well of a multiwell plate. By imaging cells at the whole-cell level, it is possible to distinguish between live and dead cells, accurately determine cell size and outer morphology, and analyse population-level responses. Subcellular resolution is not necessarily required as the focus is on capturing cell-level information rather than intricate details of internal structures. By prioritizing cell-level resolution, it allows for efficient screening of a large number of cells and facilitates the identification of cellular phenotypes and responses associated with the specific experimental conditions or drug treatments. This approach strikes a balance between obtaining valuable information about cell

populations while optimizing the throughput and processing capabilities of screening module. In order to image 3D cell cultures, Z-stacking capability of the microscope is necessary. Here, a minimum step size of 10 µm or lower is necessary to capture each cell. Additionally, the microscope should be compatible with standard cell assay, e.g. live/dead cell viability assays; hence, it should have a minimum of two fluorescence channels, preferably in the green and red spectra.

The corresponding XYZ-stage needs to fulfil the following functions: transportation of tissue culture multiwell plates from the storage module of the biomanufacturing workstation to the microscope and allow travelling between individual wells in XY direction for imaging. Hence, based on the dimension of the workstation and size of microwell plates, the X-axis needs to have a minimum travel range of 200 mm, the Y-axis 120 mm and the Z-axis 240 mm. The spatial resolution of the X- and Y-axis should be around the size of one cell, hence between 20 - 30 µm.

Chapter 3: Research Design

This chapter describes the methods and design adopted by this research to achieve the aims and objectives stated in Chapter 1 to establish an automated workflow for the biomanufacturing workstation, the integration of an imaging module and proof-of-concept studies of the whole system. Section 3.1 describes the methods used to establish automated workflows for the biomanufacturing workstation (aim 1); section 3.2 details the assembly of the imaging module and the methods used for the validation of the microscope and the XYZZ-stage (aim 2), and section 3.3 outlines the process and methods for the proof-of-concept studies (aim 3).

3.1 AIM 1: VALIDATION OF THE BIOMANUFACTURING WORKSTATION

The objective of aim 1 is the validation of the biomanufacturing platform for photo-crosslinkable hydrogels. The automated workflow for the biomanufacturing of hydrogels was analysed and optimised, the reproducibility was increased, and a library of hydrogels' properties was established, which facilitates the manufacturing of defined mechanical characteristics.

3.1.1 Implementation of an automated and reproducible workflow for manufacturing of gelatin methacryloyl (GelMA)-based hydrogels

The transition from manual to automated workflows is not as self-evident as it seems. Standardised workflows have to be established, which are compatible with various applications, pipetting steps have to be minimised, manual handling has to be translated into automated processes, and complex movements have to be diminished.

In manual workflows, hydrogels are often crosslinked in casting moulds and covered with glass slides. Afterwards, the gels are removed and transferred into cell culture dishes [56]. However, this workflow contains complex movements, which cannot be translated into automated movements. In order to automate the biomanufacturing of hydrogels with subsequent automated image analysis, the hydrogels must be produced, processed and analysed within one single microwell plate. However, various parameters influence the crosslinking rate and properties of the hydrogels: the exposed surface of the gel to oxygen [64], the material of the surrounding gel and the volume of the gel can influence the crosslinking rate [57].

Therefore, the automated system had not only to be established (aim 1.1) but also characterised (aim 1.2).

3.1.1.1 Realisation of an automated workflow

For the automated manufacturing of GelMA-based hydrogels, three input solutions need to be provided (Figure 3.1: Input): a stock solution with 20% (w/v) GelMA (or any other concentration, which should be at least 10% higher than the highest concentration of GelMA to be produced), a stock solution of the photo-initiator (here 30 mg/ml LAP in phosphate-buffered saline (PBS)) and PBS to dilute the GelMA stock solution. The input solutions are incubated at 37°C to decrease the thermal crosslinking of the GelMA solution and facilitate its pipetting. This temperature is also ideal for future cell studies.

According to the final concentration, PBS, photo-initiator and GelMA stock solution are distributed to create a mastermix, mixed immediately (Figure 3.1: Mixing) and incubated at 37°C. The mixing of the three input solutions is a crucial step to ensure reproducibility and consistent results. An extensive study of this mixing step is described in section 3.1.1.4. After sufficient mixing, the mastermix is distributed to the output microplates (Figure 3.1: Output). Since their volume-throughput ratio is optimal for this application, transparent 96 microwell plates are used as a model system. 60 µl of each mastermix are pipetted into each well. This volume is the minimum volume to ensure complete coverage of the bottom of the well, necessary for mechanical testing while keeping the meniscus as low as possible. For all aspiration steps of hydrogel, it is crucial to adjust the immersion depth of the pipette tip. In order to avoid excess hydrogel on the outside of the pipette tip, the immersion depth has to be 2 – 3 mm below the surface of the current liquid level.

After distributing the mastermix to the output, the 96 microwell plate is moved to the crosslinker module to photo-crosslink the hydrogel for a specific time and intensity with visible light ($\lambda = 400$ nm) (Figure 3.1: “Crosslinking”), according to the protocol. Once the gels are crosslinked by light exposure, the plate is moved back to the pipetting module to add PBS or cell culture media (Figure 3.1: “Addition of PBS for Swelling”), which is necessary for swelling of the gels. 200 µl PBS are added on top of every gel. After incubation at 37°C in humidified air to allow swelling of the gels, the gels can be processed for further analysis (Figure 3.1: “Mechanical Testing”).

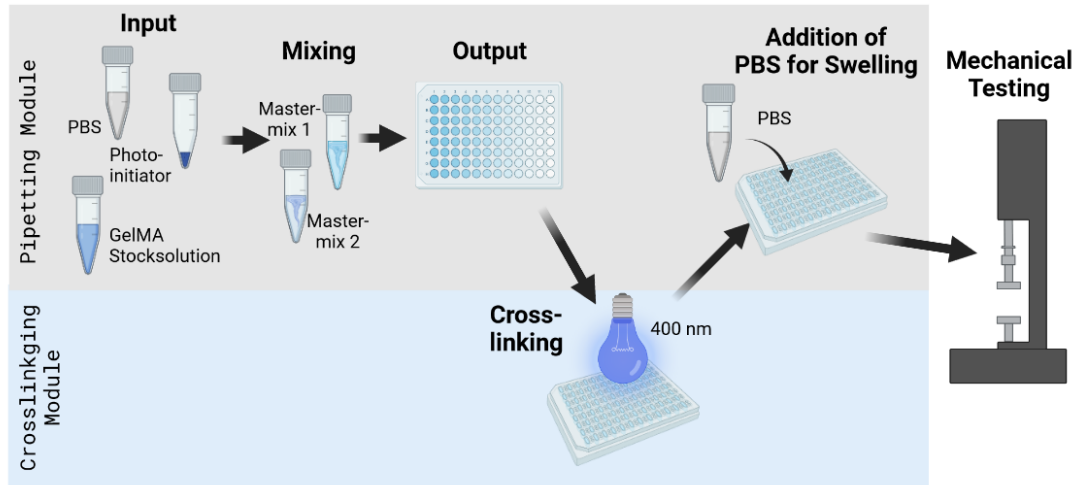


Figure 3.1 Automated workflow for the production of GelMA-based hydrogels

Three solutions (PBS, photo-initiator and GelMA stock solution) need to be provided as an input for the automated production of GelMA-based hydrogels. These input solutions were mixed on the pipetting module to mastermixes (Mixing) and distributed to a microwell plate (Output). The plates were moved to the crosslinking module and illuminated with light of a specific wavelength to initiate the crosslinking reaction. Then, the plates were transported back to pipetting module to add PBS to enable swelling of the hydrogels. After incubation time, the hydrogels can be further analysed, e.g. mechanical analysis with compression tests (Figure created with Biorender).

3.1.1.2 *Mechanical analysis of manufactured hydrogels*

The compressive modulus was measured in an immersed unconfined compression testing setting (Figure 3.2 C) with an Instron 5567 microtester (Instron, Norwood, MA, US) to determine the stiffness of the manufactured hydrogels. After swelling of the manufactured hydrogels, blue food colour was added to the wells to stain the gels to enhance contrast and visibility. The gels were removed from the well, and a cylindrical specimen was punched out with a biopsy punch (Biopsy punch, 4 mm, kai medical, Solingen, Germany). The punched-out hydrogel was placed under the non-porous aluminium indenter in a PBS bath at 37°C to mimic physiological conditions. The hydrogels were tested with a strain rate of 0.01 mm/s until failure, or the maximum load of the load cell (5 N) was reached.

The compressive modulus was calculated from the measured data as follows: First, the height h (mm) of each hydrogel was determined from the force-displacement curve. The height of the gel was defined as the point at which the curve deviates significantly from the baseline; this point is marked in the extension-load diagram in

Figure 3.2 A. To obtain the stress-strain curve (Figure 3.2 B), the strain ε_1 (mm/mm) was calculated for each point

$$\varepsilon_1 = 1 - \frac{\text{displacement}}{h} \quad \text{Equation 3.1}$$

and the stress σ_1 (kPa) was calculated via the applied force F (N) and the cross-sectional area a (mm^2)

$$\sigma_1 = \frac{F_1}{a} * 1000 \quad \text{Equation 3.2}$$

The compressive modulus E_c is determined as the slope of the linear region of the stress-strain curve between 10% and 15% of the compressive strain (Figure 3.2 D). It can be calculated as the slope of a tangent between 10% and 15% of strain with the equation

$$E_c = \frac{\sigma_{0.15} - \sigma_{0.1}}{\varepsilon_{0.15} - \varepsilon_{0.1}} \quad \text{Equation 3.3}$$

where $\varepsilon_{0.15}$ is a strain of 0.15 and $\sigma_{0.15}$ is the stress at this point, $\varepsilon_{0.1}$ and $\sigma_{0.1}$ accordingly [56].

To accelerate the calculation of the compressive modulus of the high amount of samples, which can be manufactured by the biomanufacturing workstation, we developed the software *MechAnalyze*, described in section 3.1.3.

3.1.1.3 Influence of photo-initiator concentration

To assess the influence of the concentration of the photo-initiator LAP on the compressive modulus, two commonly used concentrations were tested. 10% GelMA hydrogels with 0.15% and 0.30% LAP concentration, respectively, were manufactured as described above, 60 μl of each distributed to transparent micowell plates and crosslinked for 2, 4 and 8 min, respectively. After crosslinking, PBS was added for swelling of the gels, incubated, and compressive modulus was measured the next day.

3.1.1.4 Optimisation of mixing step

To ensure reproducible results and minimise their standard deviations, the manufacturing of GelMA-based hydrogels made from a 20% GelMA stock solution was optimised. Orange G was added to PBS to a final concentration of 0.2 mg/ml to determine the mixing efficiency. By measuring the absorbance of Orange G, its distribution throughout the tube and, therefore, the mixing efficiency could be measured. Samples of 60 μl from four positions in the mastermix were distributed to

a 96-microwell plate (Figure 3.3), and the absorbance was measured at 450 nm using a microplate reader (CLARIOstar, BMG Labtech).

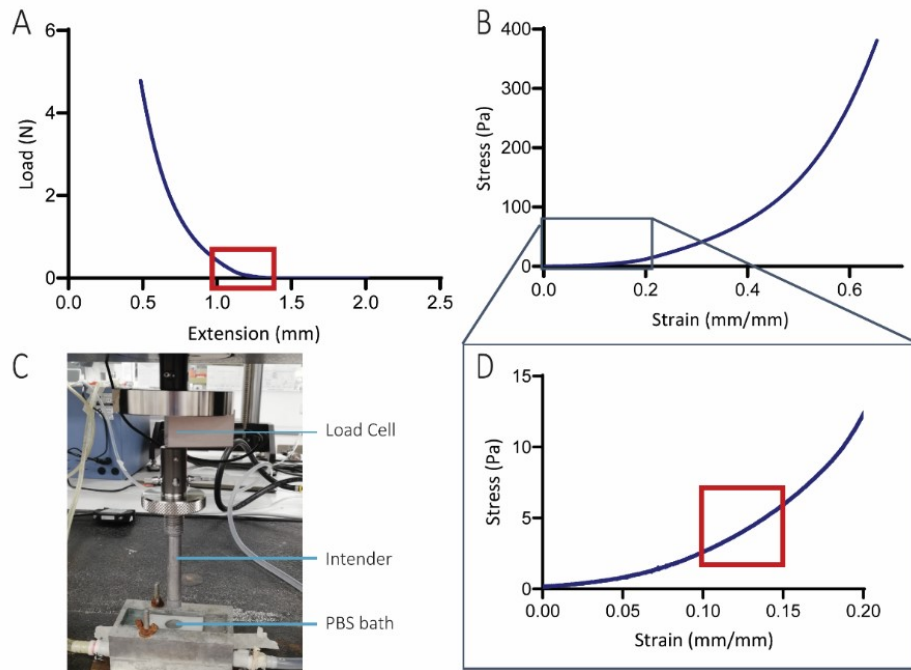


Figure 3.2 Calculation of the compressive modulus

(A) Extension-load diagram. The point where the curve deviates from the baseline, required for height calculation, is marked in the red rectangle. (B) Strain-stress curve used for calculating the compressive modulus. (C) Experimental set-up of a microtester for immersed unconfined compression test. (D). Zoomed-in area of the strain-stress curve shown in (B). The slope of the marked area is the compressive modulus.

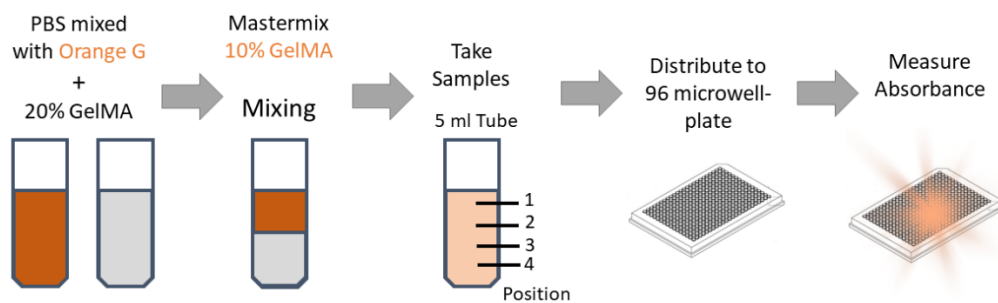


Figure 3.3 Optimisation workflow

PBS, mixed with Orange G, and a 20% GelMA stock solution were mixed in equal parts according to multiple mixing protocols. After mixing, three samples were taken and distributed to a 96-microwell plate at each of four positions to measure the absorbance.

The mastermix was mixed using different protocols varying in a number of mixing steps, the position of the pipette for mixing and increasing the speed of

aspirating and dispensing liquid. Four to eight different mixing protocols were tested in one experiment. To compare protocols with varying intensity, the coefficient of variation (CV), also known as relative standard deviation (RSD), was calculated as the ratio of the standard deviation (STD) σ to the mean μ :

$$C_v = \frac{\sigma}{\mu} \quad \text{Equation 3.4}$$

For the next optimisation step, the two protocols with the lowest relative standard deviations were chosen and slightly modified for further optimisation.

Statistical Analysis

Statistical analysis of the data was performed using two-way analysis of variance (ANOVA) and post-hoc tests where appropriate using the statistical analysis software IBM SPSS Statistics 25 (IBM Corporation) to calculate p values. Differences were considered statistically significant for $p < 0.05$ (*).

3.1.2 Conception of a parameter library

The physicochemical properties of the ECM largely regulate cellular function. Thus, the fundamental effects of parameters, such as polymer concentration and crosslinking conditions, on the properties of hydrogels produced by a biomanufacturing platform were characterised by a systematic assessment of the following parameters on hydrogel physical properties:

- polymer concentration (w/v)
- Crosslinking parameter:
 - light exposure time
 - light intensity

Experimental work and set-up were organised following a “Design of Experiment” (DoE) approach to select a representative set of experiments and identify the influence of each parameter. Pipetting protocols for automated manufacturing were written in the programming language Python, based on manual production steps. Then, pipetting tasks and crosslinking of hydrogels were undertaken on the biomanufacturing workstation. Subsequently, the compressive modulus of automatically produced hydrogels was determined by unconfined compression testing under physiological conditions. The aim was to establish a methodological library,

enabling automated manufacturing of biomechanically defined hydrogel properties with given parameters.

3.1.2.1 Design of Experiment

With a DoE approach, multiple parameters can be evaluated to study their influence on the response parameter. Contrary to a ‘changing one separate factor at a time’ (COST) approach, various factors, which are interconnected, are changed at the same time. Statistical tools can filter the key parameters with only a few experiments [107].

The Box-Behnken design, which is a three-level response-surface modelling (RSM) design, was used for the parameter library for the automated biomanufacturing of GelMA hydrogels. Thereby all design points, except for the centre points, are located at the centre of the edges of a hypercube and on the surface of a sphere (Figure 3.4). Thus, the full quadratic model can be estimated.

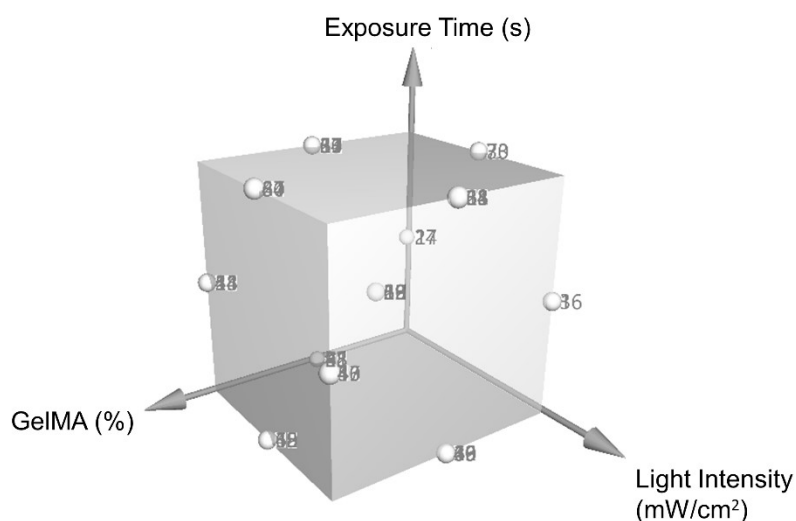


Figure 3.4 Box-Behnken-Design with design points on the edges and in the centre

A Box-Behnken-Design is a three-level response-surface modelling design, which was used to estimate the full quadratic model. Except for the centre point, all design points, which represent the parameter combinations, are located in the centre of the edges of a hypercube and on the surface of a sphere. Three parameter axes define the hypercube: GelMA concentration (%), light intensity (mW/cm^2) and exposure time (s) (adapted from MODDE 12.1).

The design and experimental parameters were calculated using the DoE software MODDE® (Version 12.1, Umetrics™, Sartorius Stedim Biotech) with the factors listed in Table 3.1. In order to estimate the entire model, a Box-Behnken design was

used, with 12 design runs, one centre point, and four replicates, resulting in 65 total runs.

Biomanufacturing and analysis of GelMA-based hydrogels

The hydrogels were manufactured according to the automated workflow described in section 3.1.1.1 with parameter combinations based on a Box-Behnken-Design, calculated with MODDE. Afterwards, the compressive modulus was determined by unconfined compression tests as described before (section 3.1.1.2) and calculated with *MechAnalyze* [108]. The determined compressive moduli were analysed with MODDE and log-transformed ($10\log(Y)$) for the prediction plots because the data showed a positive skewness.

Table 3.1 Factors for DoE approach

Parameter	Unit	Type	Use	Settings	Trans-formation	Precision
GelMA	%	quantitative	Controlled	3.5 to 15	None	1
Light Intensity	mW/cm ²	quantitative	Controlled	0.5 to 4	None	0.5
Exposure Time	seconds	quantitative	Controlled	120 to 360	None	-

3.1.3 Automated analysis of compression test data with *MechAnalyze*

To accelerate the calculation of the compressive modulus of the high amount of samples, which can be manufactured by the biomanufacturing workstation, we developed the software *MechAnalyze* [108]. Based on the raw data of unconfined compression tests, the software calculates the height of each sample, compressive modulus and, if required, failure stress and strain.

3.1.3.1 Sample preparation, compression test and manual determination of mechanical parameters

Hydrogels were prepared from GelMA, as described in section 3.1.1. Additionally, hydrogels prepared from other polymers, such as alginate, of varying concentrations and natural tissues, such as articular cartilage, were used to validate the software. Before the compression test, hydrogels were allowed to swell overnight at 37°C in PBS. Articular cartilage was obtained with ethics approval from the Holy

Spirit Northside Hospital (Brisbane, QLD, Australia) and Queensland University of Technology (ethics number: 1400001024) from consenting patients undergoing total knee arthroplasty surgeries for osteoarthritis.

All samples underwent unconfined compression tests and were analysed manually as explained in 3.1.1.2.

3.1.3.2 Algorithm of MechAnalyze

First, the algorithm determines the height of the sample with the first derivate of the load-displacement curve. Contact of the indenter and sample is assumed, hence the sample's height, once the first derivate exceeds a threshold larger than the background noise. The algorithm calculates the sample strain with the determined sample height and the piston extension. The sample stress is calculated by applying the load force on the user-specified sample cross-sectional area. A mechanical failure of the sample is assumed if, after the first piston contact of the sample, the next derivate of the stress-strain curve exhibits a negative value, which is larger than 5% of the absolute value, corresponding to the maximum positive value in the dataset. Finally, the compressive modulus is determined from the slope of the linear function, which is fitted to the stress-strain curve in the range of 10-15%, as described by Loessner et al. [56].

3.1.3.3 Use of the software

The software uses the raw data of the compression test measurements, load in Newton (N) and displacement in mm, and the surface area of each sample in mm², provided by the user, to calculate the mechanical parameter. A detailed step-by-step guide and a video tutorial are provided in the supplemental material of the publication [108].

After installation, the software guides the user through the analysis workflow. First, the raw data are selected, then the cross-sectional area of the samples is specified. Afterwards, the start of the load and extension data traces need to be identified, assuming all data to be analysed in this run are provided in the same format.

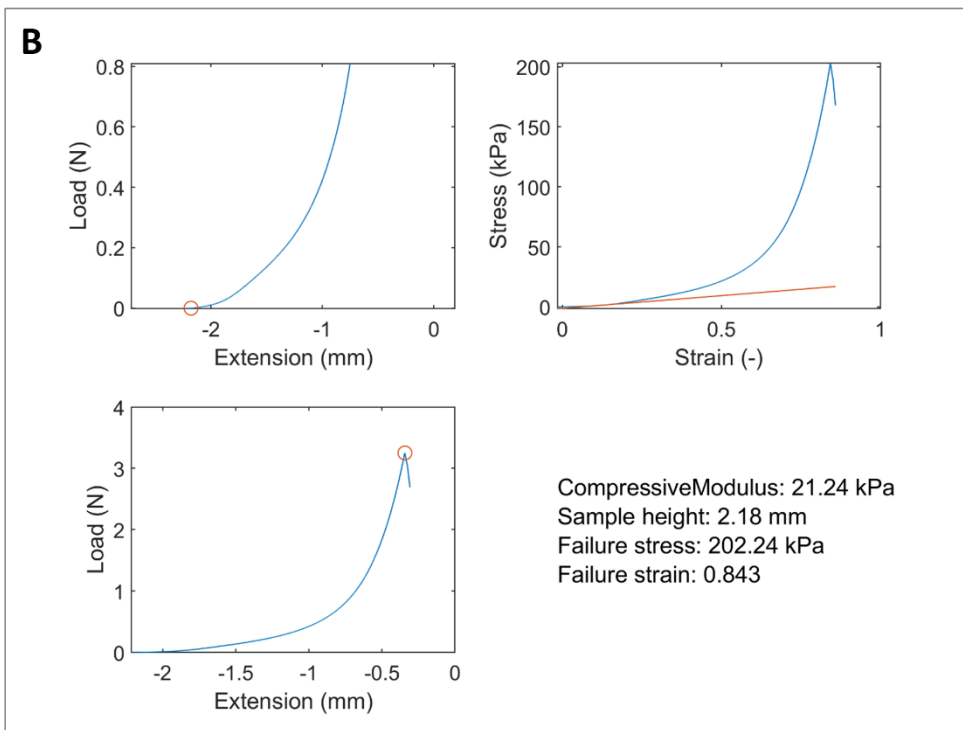
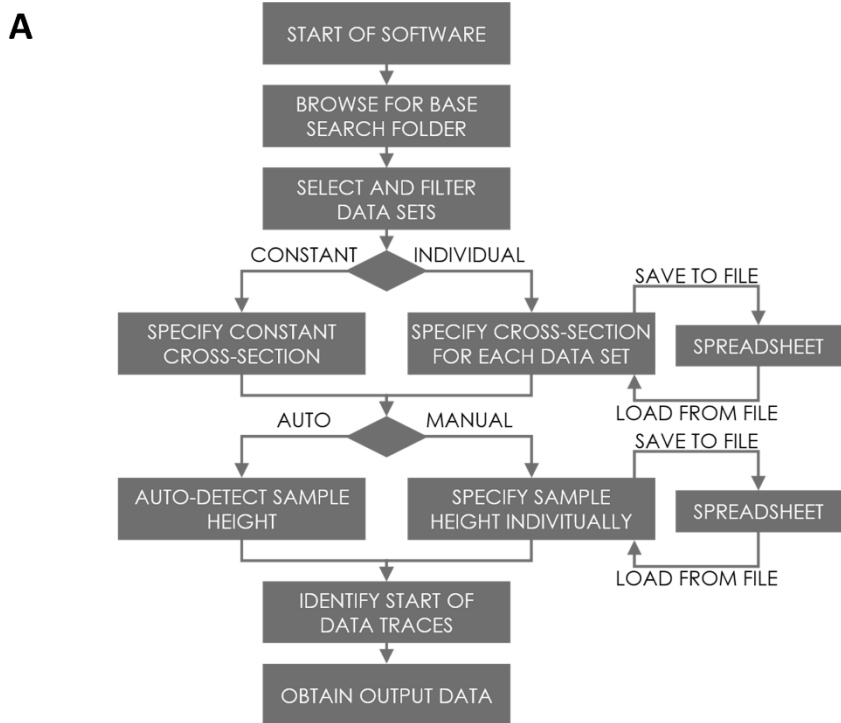


Figure 3.5 *MechAnalyze* workflow and output example

(A) This flowchart shows the user guidance through the software. (B) Example of graphs generated by *MechAnalyze*, with load-extension and stress-strains diagrams and the key parameter calculated for each sample (adapted from Kahl et al. [108]).

Then, the software runs through all initially selected data and provides, alongside the determination of the compressive moduli and failure points, load-extension and stress-strain plots as vector graphics. A spreadsheet file is generated containing all relevant data: compressive modulus, sample height, failure stress and failure strain. Visual quality control should be conducted to check the correct determination of the sample height in the load extension diagrams, which is marked with a red circle. If the software has not determined the sample height correctly, the height can be specified manually in a second analysis run of the data.

3.1.3.4 Statistical analysis

Statistical analysis was performed using SigmaPlot 14.0 (Systat Software, Inc.) to compare manually and automatically analysed data of the compression tests (compressive modulus and height: n = 698; failure properties: n = 355). Linear regression analysis was used to display the relationship between manual and automated determined values for each parameter. For better comparison of the results of *MechAnalyze* with manual analysis, Bland-Altman plots [109] were created with SigmaPlot for each parameter, illustrating the agreement of both methods. In addition, for each parameter, an error was calculated by dividing the mean difference by the mean average of manual and automated analysis.

3.2 AIM 2: INTEGRATION OF AN IMAGING MODULE

The objective of aim 2 is the implementation of an automated optical analysis unit into the biomanufacturing workstation to cover the entire workflow of drug screening from production to processing and analysis of 3D tumour models.

Although several high-content imaging systems suitable for 3D tumour models (Appendix A) are commercially available, they are very cost-intensive and bulky. Due to their incapability to soft- and hardware modifications, they are not compatible with our in-house developed biomanufacturing workstation. Therefore, the aim is to provide an open source-based solution that facilitates the analysis of 3D tumour models while being connectable to the biomanufacturing workstation. The imaging module needs to fulfil various requirements to enable 3D high-content imaging. These requirements include a good signal-to-noise ratio, a large field of view with an adequate spatial resolution, optical sectioning capability, and a fast image stack recording rate [75].

The optical unit consists of an inverted widefield fluorescence microscope enabling fluorescence-based cell assays. Widefield fluorescence microscopy permits a faster imaging process than confocal laser scanning microscopy but still provides a sufficient resolution to distinguish between individual cells [81]. Two fluorescence channels were included in the microscope to enable live/dead viability assays and the differentiation between compartments. Furthermore, a custom-made inexpensive motorised positioning stage for automated high-content screening based on an open-source design [104] is integrated. Following the proposed design, no manual handling of the microplates is necessary, and the workflow, from preparing mastermixes, distribution to microwell plates, media exchange, and addition of drugs and stains to incubation and imaging can be automated.

3.2.1 Fluorescence microscope

An inverted widefield epi-fluorescence microscope (Figure 3.6 A) was engineered into the opto-mechatronic screening module. The body of the microscope mainly consists of optomechanical components from Thorlabs. Two high-power LEDs combined with an aspheric condenser lens form the illumination unit. The LEDs are connected to and controlled via a single-board computer, a Raspberry Pi 3 Model B+. The fluorescence filter setup consists of a multi-band fluorescence dichroic mirror and a multi-band emission filter to allow imaging of different fluorescence spectra without the need of changing the fluorescence filter (Figure 3.6 B). The objective (10x 0.3 NA) is installed on a translational stage attached via gears to a small stepper motor for image focusing. Hence, the sample remains stationary during imaging and Z-stacking. Emitted fluorescence light passes the multi-band fluorescence filters and is focused by an achromatic doublet lens, acting as a tube lens, onto a Raspberry Pi HQ camera connected to the same single-board computer as the LEDs. All components are listed in detail in Appendix B.

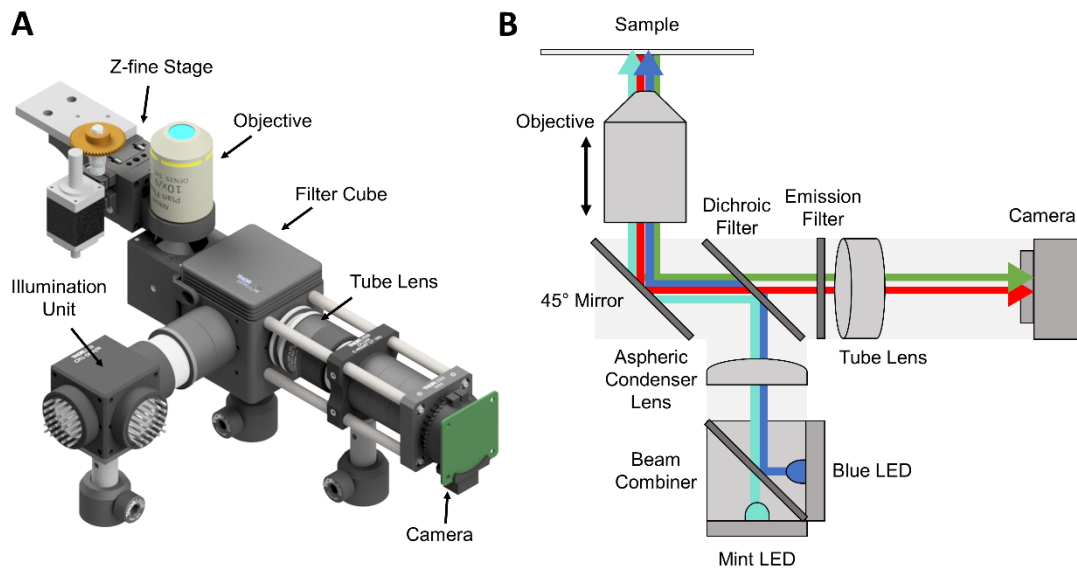


Figure 3.6 Microscope and its lightpath

(A) Isometric view of the microscope (CAD drawing) (B) Lightpath of the microscope. The light of the mint LED passes through the beam combiner, the light of the blue LED is reflected by the beam combiner, positioned at a 45° angle. Both light beams are collimated by the aspheric condenser lens and reflected by the dichroic filter onto the 45° mirror. The objective focuses the light beam onto the specimen, where the fluorophore is excited. The emission light is collected by the objective, reflected by the 45° mirror and passes through the dichroic and emission filter. The tube lens focused the light onto the camera sensor.

3.2.1.1 Assembly of the microscope

Microscope body

The microscope is based on Thorlabs' optomechanical components with the 30 mm cage systems and Ø1" lens tubes, which can be easily connected. The objective of the microscope is attached to the Z-focus stage, which, in turn, is attached to an aluminium profile of the frame, described in 3.2.2.

The body of the microscope consists of a 45° prism mirror (CCM1-P01/M, Thorlabs), connected to a filter cube (DFM1L/M, Thorlabs), on which an achromatic doublet lens (AC254-100-A-ML, Thorlabs) was connected. The achromatic doublet lens acts as a tube lens and focuses the light on the camera sensor. The camera (Camera HQ, Raspberry Pi) was attached to a cage plate (CP13/M, Thorlabs). Lens tubes (SM1, Thorlabs) were installed between the tube lens and the cage plate to reduce background light and ensure a fixed focal length. The required focal distance of 97.5 mm between the tube lens and the camera sensor was adjusted with an adjustable lens tube (SM1V10, Thorlabs) between the two components. Cage assembly rods (ER6,

Thorlabs) were installed between the filter cube and the cage plate for additional support and prevention of skewness of the microscope body. The microscope body was attached to an optical breadboard (MB1545/M, Thorlabs) via optical posts (TR30/M and TR40/M, Thorlabs) mounted on the filter cube and the cage plate.

Illumination unit

The illumination unit of the microscope consists of blue (XP-E2 SMD-LED blue, Cree) and mint (MINTD3, Thorlabs) high power SMD LEDs. The light is combined with a beam combiner (MD498, Thorlabs) and is collimated with an aspheric condenser lens (ACL2520U-DG15-A, Thorlabs). The illumination unit was attached to the fluorescence filter cube of the microscope body so that the light is reflected by the dichroic mirror and the 45° prism mirror onto the objective.

Each high power SMD LED was attached to a passive heatsink (heatsink round 28,5 mm for star circuit boards, Fischer Elektronik) via thermal adhesive pads and connected to a DC-DC constant current step-down LED driver (LDD-700HW, Mean Well). The heatsink was fitted into a Ø1" lens tube for easy integration into Thorlabs' Ø1" lens tube and 30 mm cage system (Figure 3.7). The LEDs were attached to a filter cube (CM1-DCH/M, Thorlabs) at a 90° angle, according to Figure 3.7. A beam combiner was placed into the filter cube to deflect the light on an aspheric condenser lens mounted into a Ø1" lens tube (SM1L05, Thorlabs). The condenser lens has an integrated diffuser and collimates the light of the LEDs for even illumination. An adjustable lens tube (SM1V10, Thorlabs) between the condenser lens and the filter cube, on which the LEDs are attached, allows adjusting the correct distance between the two optical components.

Z-focus stage

The objective (N10X-PF, Thorlabs) of the microscope was attached via adapters (MS103/M, CT101, Thorlabs) to the Z-focus stage, which consists of a manual side-actuated travel translation stage (MS1S/M, Thorlabs) as shown in Figure 3.7. The stage has a motion range of 6.5 mm and provides a travel distance of 0.5 mm per revolution. The knob of the stage was modified to fit a gear wheel, which is connected to a pinion attached to a NEMA 8 stepper motor. An angle bracket (MS102/M, Thorlabs) is attached to the backside of the stage to allow mounting to an aluminium profile via a customized adapter (Z01, Appendix C).

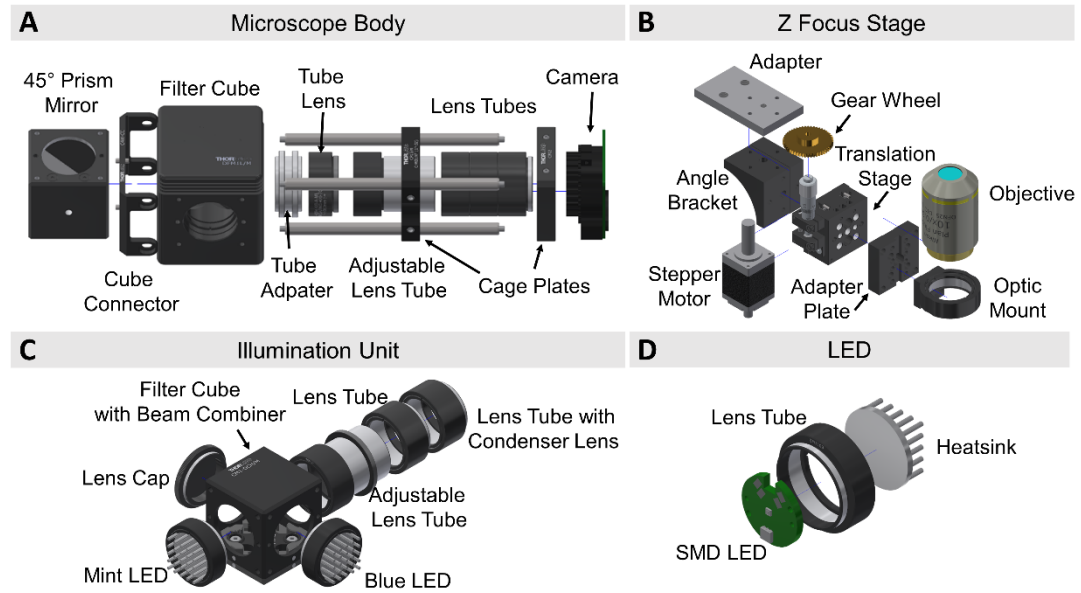


Figure 3.7 Microscope assembly

(A) Detailed view of the microscope body. The microscope body consists of a 45° prism mirror, which reflects the light from the filter cube on the objective and back, a filter cube with a dichroic mirror and an emission filter, a tube lens, a camera, which is attached to a cage plate and several lens tubes to connect the components. **(B)** Detailed view of the Z-focus stage. The objective is mounted via adapters to a motorised translation stage. The translation stage is powered by a small stepper motor, which is connected via gear wheels. **(C)** Detailed view of the illumination unit. Two LEDs are attached at a 90° angle to a filter cube. The light is transmitted and reflected by a beam combiner onto the condenser lens with an integrated diffusor. **(D)** An individual LED consists of an SMD-LED, attached to a heatsink, which is fitted into a lens tube.

Filter and LED setup

Typically, two fluorescence channels require the exchange of excitation and emission filter. However, the automated exchange of fluorescence adds another layer of complexity and possible error-proneness to the system. In order to overcome these challenges, multi-band bandpass fluorescence filters are used. In contrast to conventional fluorescence bandpass filters, multi-band fluorescence bandpass filters have multiple, in general, two to four, bands on a single filter to allow multiple wavelengths ranges passing through. This way, multiple fluorophores can be imaged simultaneously as multi-colour images or, with different LEDs, one after another at high speed without the need of mechanically switching the filter setup. Matching multi-edge fluorescence dichroic filters provides multiple transmission and reflection wavelength ranges to allow several (two to four, depending on the filter) excitation light ranges to be reflected and emission light passing through.

Here, a multi-edge fluorescence dichroic filter (#87-284, Edmund Optics Ltd, York, United Kingdom) and a matching multi-band fluorescence emission filter (#87-244, Edmund Optics Ltd, York, United Kingdom) were inserted into the filter cube. Due to the narrow spectra of the utilised LEDs, an emission filter was not used to reduce costs.

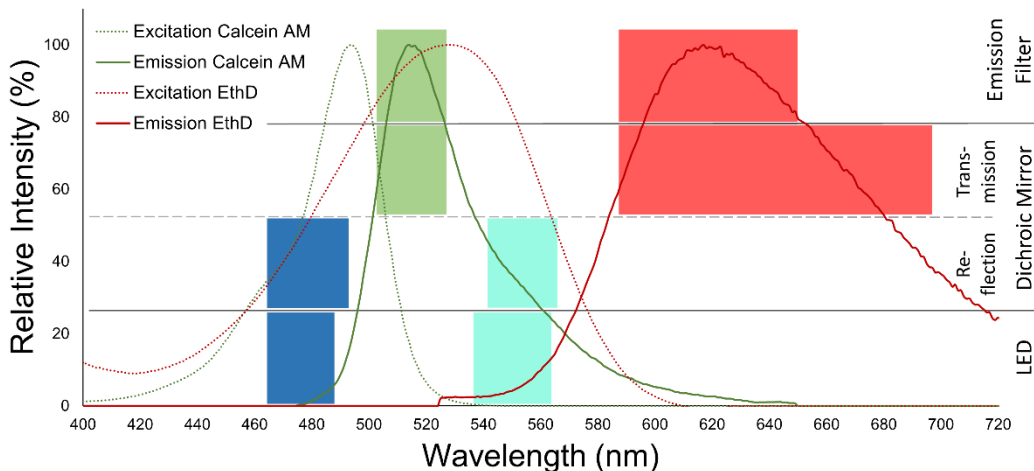


Figure 3.8 Wavelength spectra of multi-band fluorescence filter, LED and two dyes for live/dead imaging

The excitation and emission spectra of Calcein, a dye staining live cells, and EthD-III, a nucleic acid dye staining dead cells, are plotted in the graph. The excitation maximum of Calcein matches with the blue LED, and the excitation maximum of EthD-III matches with the mint LED. The multi-edge dichroic filter has two reflection bands between 466 - 490 nm and 546 - 565 nm, which overlap with the LED spectra, and two transmission bands between 505 - 528 nm and 684 – 700 nm, which overlap with the emission maxima of the corresponding dyes. The multi-band fluorescence emission bandpass filter has two transmission bandwidths at 517/23 nm and 615/61 nm, which overlap with the transmission bandwidths of the dichroic mirror.

3.2.1.2 Validation experiments of the microscope

Image resolution

A 1951 USAF test target (R3L1S4N, Thorlabs) was imaged in transmission mode to determine the microscope's resolution and contrast capacity. The contrast capacity was determined by measuring the grey values of a set of lines of the test target with ImageJ. The pixel size was determined by measuring the number of pixels of a given line of test target of known distance.

Axial resolution

Green-fluorescent microspheres (InSpeck™ Microscope Image Intensity Calibration Kit 2.5 µm, Molecular Probes Inc, Leiden, Netherlands) were embedded

in 5% (w/v) GelMA, distributed in 96 microwell plates and crosslinked for 4 min. PBS was added, and the hydrogels were left overnight for swelling. Images of the microspheres were taken as Z-stacks with a step size of 12.5 µm to determine the axial resolution. The PSF was determined using the ImageJ plugin PSFj (Version 2.5_build_245) [110] with the 3D search option of one image taken as described above. Within this image, 202 beads were analysed and averaged for the determination of the PSF to overcome the limitation of the step size being greater than one microsphere.

Microsphere validation

5 % (w/v) GelMA precursor solutions with 0.15% LAP were prepared and mixed with green-fluorescent microspheres (InSpeck™ Microscope Image Intensity Calibration Kit 6 µm, Molecular Probes Inc, Leiden, Netherlands) in concentrations of 50, 100, 300, 400, 500, 600, 700, 800, 900 and 1000 microspheres/µl. 80 µl of each concentration was distributed in triplicates to a 96-microwell plate and cross-linked for four minutes. Then, PBS was added to each sample and incubated overnight at 37°C, 5% CO₂ in a humidified atmosphere. The next day, images were taken as Z-stacks, with a step size of 10 µm and 31 images per stack, illuminated with blue light.

3.2.2 XYZz-stage

The XYZz-stage is composed of an X-, Y-, Z-coarse and Z-fine stage mounted into a frame of aluminium profiles. All components of the XYZz-stage are listed in Appendix B. The assembly of the Z-fine stage is described in 3.2.1.1.

The dimensions of the basic framework of the OMSM were adopted from the biomanufacturing workstation. Hence, the outer dimensions of the module are 460 mm x 460 mm x 560 mm. Four aluminium profiles with a length of 560 mm (NFSL6-3030-560, Misumi) were connected via brackets and joints to eight profiles with a length of 400 mm (NFSL6-3030-400, Misumi), each four at the bottom and top of the frame. An additional aluminium profile (400 mm x 30 m x 30 mm), on which the Z-fine stage was attached, was mounted on the left side of the frame with a distance of 166 mm from the bottom. Two additional 400 mm profiles were mounted at the back of the frame to hold the Z-coarse stage.

3.2.2.1 Assembly of X-, Y-, and Z-coarse stage

Baseplates, connection bridges, stepper motor holders and angles were manufactured from aluminium plates in a mechanical workshop according to their technical drawings shown in Appendix C.

A linear rail guide (SSE2BSL10-265, Misumi, Frankfurt, Germany) was attached to the base plate (X01, Appendix C) using M3 screws (Figure 3.9 A). The distance between the linear rail and the edge of the baseplate was measured using a dial gauge (Mitutoyo, Neuss, Germany) to ensure parallel alignment. The second linear rail guide was positioned parallel to the first linear rail guide with the help of the dial gauge (Figure 3.9 B, C). The connecting bridge (X02, Appendix C) was screwed onto the four carriages of the linear rail guide (Figure 3.9 D). Parallelism of the rail guide was again ensured by sliding the bridge back and forth if it could be moved back and forth easily without any resistance. If not, the position was repeatedly corrected with the help of the dial gauge.

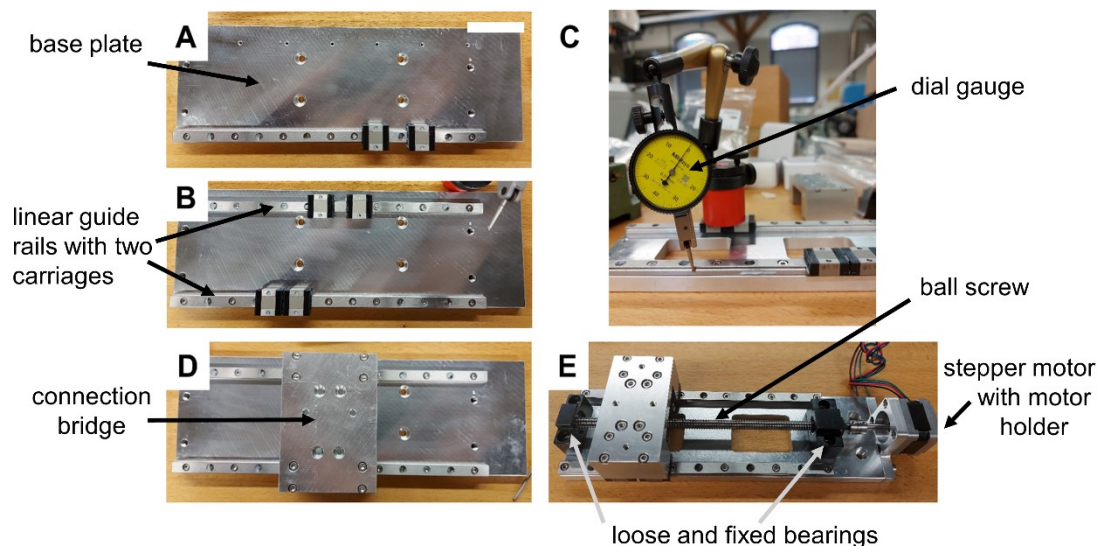


Figure 3.9 Assembly of the X- and Y-stage

(A) A linear rail guide was mounted on the baseplate of the X-stage. Scale bar (upper right corner) = 50 mm (B) A second linear rail guide was attached to the base plate. (C) Parallelism of both rail guides was ensured with a dial gauge. (D) A connection bridge was mounted on the carriages of both rail guides. (E) The finalised Y-stage. The baseplate of the Y-stage has two holes to reduce weight while maintaining stability.

The bracket (BNFA1004R-20, Misumi) was screwed onto the nut of the ball screw (BSST1004-280, Misumi) and tightened. The loose bearing (C-BSW8S-SET, Misumi) was attached to the end of the ball screw and tightened with a clamp. The

fixed bearing was placed on the other side of the screw and fixed with a nut to keep the bearing in position. The bracket of the loose bearing was mounted onto the base plate. The loose and fixed bearings, on which the ball screw is attached, were attached to the bracket. The connecting bridge X02 was mounted to the bracket of the ball screw. After testing, if the system slides smoothly back and forth, all screws were tightened with hex wrenches. The coupling (MST-12-5-6, Misumi) was attached to the ball screw. The stepper motor holder (X03, Appendix C) was screwed onto the stepper motor (2018246, Watterot, Leinefelde-Worbis, Germany), and then the holder was mounted onto the baseplate while the stepper motor was inserted into the coupling.

The Y-stage was assembled with the components listed in Appendix B in the same procedure (Figure 3.9 E).

The Z-stage (EMS1216A, Dold Mechatronik, Steinach, Germany) was assembled according to the manufacturer's instructions. Then, both angles (Z03, Appendix C) were screwed onto the Z-stage connection plate (Z02, Appendix C), and then the baseplate was attached to the carriage and the bracket of the Z-stage (Figure 3.10 A). The Z-stage was installed onto two additional aluminium profiles, which were attached to the aluminium frame (Figure 3.10 B). The X-stage was placed onto the angles attached to the Z-stage (Figure 3.10 C), and the Y-stage was installed onto the connecting bridge of the X-stage (Figure 3.10 D). Lastly, the gripper (Y04, Appendix C), which holds the tissue culture plates, was screwed onto the Y-stage connection bridge (Y01, Appendix C).

Figure 3.10 Assembly of the XYZz-stage

(A) Brackets and joints were attached to the backside of the Z-stage. (B) The Z-stage was mounted on the aluminium profiles in the back of the frame. The connection plate and angles were attached to the Z-stage. (C) The X-stage was mounted onto the angles attached to the Z-stage. (D) The Y-stage was mounted onto the X-stage, and the Z-fine stage was attached to the aluminium profile on the left side of the frame. (E) Top view of the XYZz-stage. (F) The microscope was placed on the bottom of the frame and mounted to the aluminium profiles. (G) CAD-drawing of the XYZ-stage (H) Front view (X-Z) of the XYZ stage. Scale bar (in (C) and (H)) = 100 mm

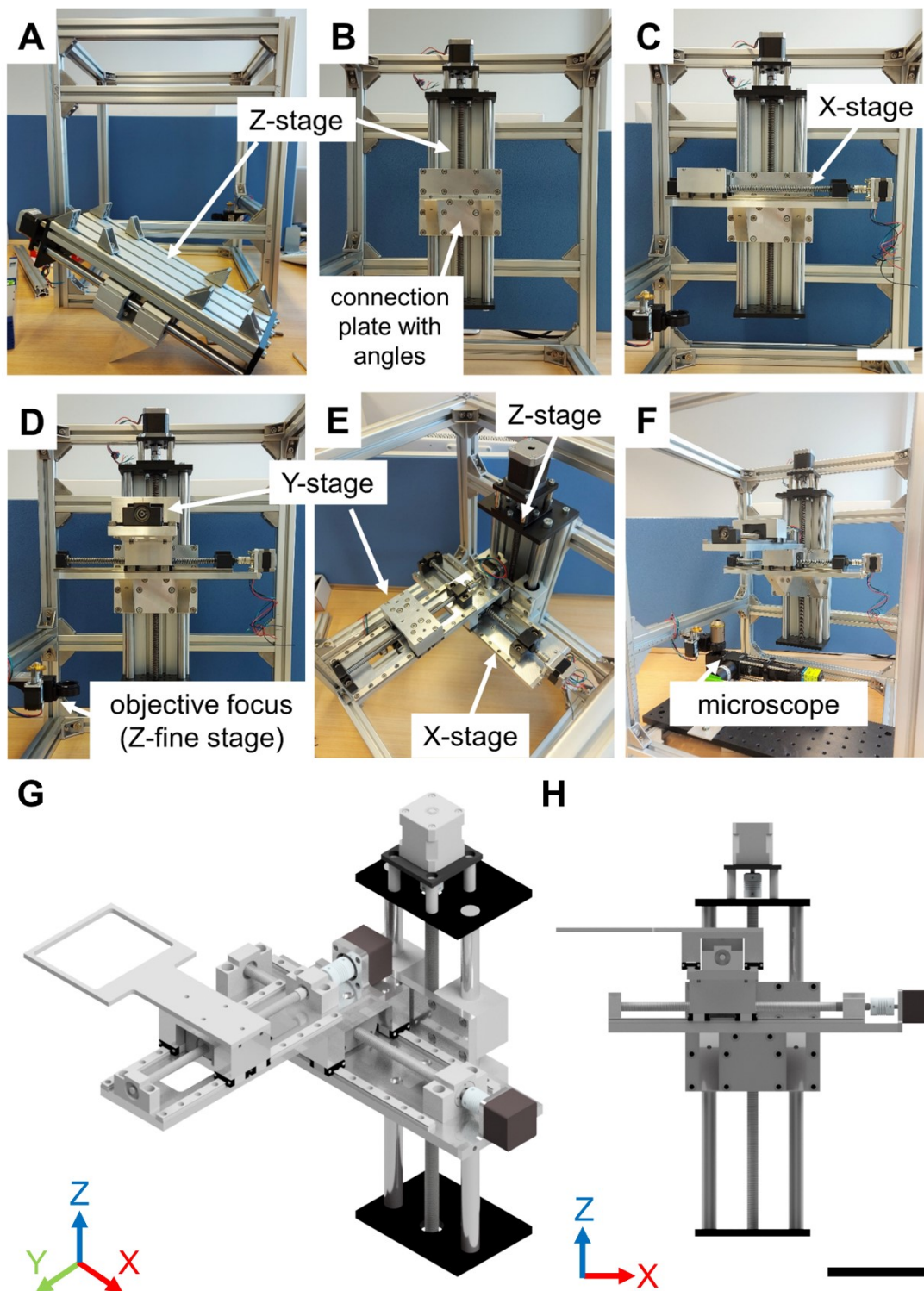


Figure 3.10 Assembly of the XYZz-stage

3.2.2.2 Validation of the XYZz-stage

The spatial resolution, accuracy and positioning repeatability were measured to validate and verify the theoretical resolution of the motorised XYZz-stage.

The spatial resolution was determined by moving the stage one step and acquiring an image of a USAF 1951 test target. Then, the stage was moved another step forward, and another image was taken. This was repeated 50 times for the X- and Y-axis in each direction. The resolution was quantified by calculating the drift of the test target in recurrently taken images [104]. Spatial resolution is the smallest travelling distance possible. The theoretical spatial resolution is calculated by dividing the pitch of the spindle by the number of steps:

$$Resolution_{theoretical} = \frac{Pitch_{Spindle}}{No.of\ Steps_{Motor}} \quad \text{Equation 3.5}$$

To evaluate whether the theoretical resolution equals the practical resolution, the drift of one axis was measured by moving the axis repeatedly one step back and forth and acquiring images of the USAF 1951 test target. The drift was quantified using the ImageJ plugin “Register Virtual Stack”.

The accuracy of an axis refers to the difference between the targeted position $x_{targeted}$ and practical distance $x_{measured}$ as quantified by a measurement device. The positioning accuracy is also referred to as the systematic error e_s and is calculated by:

$$accuracy = e_s = x_{targeted} - x_{measured} \quad \text{Equation 3.6}$$

Repeatability refers to the range of positional deviations obtained by a series of unidirectional movements to a targeted position. It is also referred to as the random error e_r or sample standard deviation and is calculated by:

$$repeatability = e_r = s = \sqrt{\frac{\sum_{i=1}^n (x_i - \bar{x})^2}{n-1}} \quad \text{Equation 3.7}$$

with x_i as the individual measured positional deviation (in μm), \bar{x} as the arithmetic means of measured positional deviations (μm) and n the number of measurements.

In order to obtain accuracy and repeatability, the axis was repeatedly moved 20 times from zero-point calibration to a specific point of the axis, where an image of the

USAF 1951 test target was acquired. Images were processed with the ImageJ plugin “Register Virtual Stack Slices”, and displacement information was quantified.

3.2.3 Integration and software

A graphical user interface (GUI), or optionally a python code, on a Raspberry Pi Model 3B (reichelt Raspberry PI 3B+ All-in-Bundle, reichelt elektronik GmbH & Co KG, Sande, Germany) controls the opto-mechatronic screening module. The camera is directly connected to the camera port of the Raspberry Pi computer. The LEDs are wired to the Raspberry Pi’s general purpose input output (GPIO) pins. The XYZZ-stage is controlled via a controller board for a 3D printer, which is connected via a universal serial bus (USB) to the Raspberry Pi (Figure 3.11).

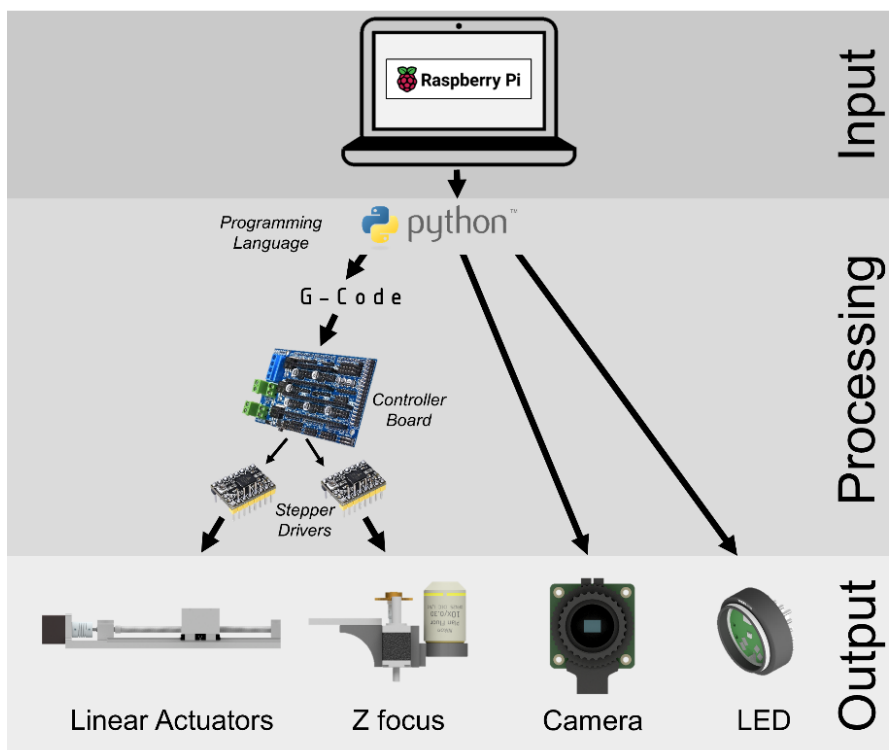


Figure 3.11 Process workflow of the OMSM-module

All components are connected to a RaspberryPi Model 3B+, which receives the input from the user. A python interface sends the G-Code commands via pySerial to a controller board that communicates via stepper drivers with the linear actuators and the Z-focus. The camera is directly connected to the Raspberry Pi via the camera port. The LEDs are connected via the GPIO pins to the Raspberry Pi. Both the camera and the LED can be directly controlled via Python commands.

3.2.3.1 Electrical engineering

XYZz-stage

A Reprap Arduino Mega Polulu Shield 1.6 plus (RAMPS 1.6+, BigTreeTech, Shenzhen, China) was used as a controller board for the XYZ-stage and the Z-focus. RAMPS 1.6+ simplifies the installation of SilentStepStick motor drivers TMC2130 and TMC2209 (SilentStepStick, Watterot electronic GmbH, Leinefelde-Worbis, Germany). TMC2130 is used for the X- and Y-stage as well as for the Z-fine stage. TMC2209 is used for the Z-coarse stage.

Wiring

The RAMPS 1.6+ board was attached to an Arduino Mega 2560 (Arduino) microprocessor. Short circuit caps were installed according to serial peripheral interface (SPI) instructions for the X- and Y-stage and the E0 spot for the Z-focus. Shortly, 1 and 11, 2 and 12, 3 and 5, 4 and 6 respectively, were connected using four short circuit caps (Figure 3.12 A). The Z-stage uses the motor driver TMC2209, where STEP/DIR mode is required. Hence, 11 and 10, 12 and 9, 5 (MS3) and 8 (high level) were connected using a short circuit cap.

The motor drivers were installed into the designated spots X, Y and Z of the RAMPS 1.6+, one for each stage. The motor driver of the Z-fine stage was installed into the E0 spot of the board. The mechanical limit switches (RepRap Mechanical Endstops) were connected to X min, Y min and Z min spots of the board. Heat sinks were attached to each motor driver as well as onto the RAMPS 1.6+ board. A 12 V/DC 5 A power supply (GST60A12-P1J, Mean Well Enterprises Co., LTD, New Taipei City, Taiwan) was attached. (Figure 3.12 B).

3.2.3.2 Software modifications

Firmware of RAMPS

In order to allow G-Code commands controlling the XYZz-stage, firmware needed to be installed on the RAMPS board. Here, a modified version of the 3D printer software Marlin 2.0 (<https://marlinfw.org>) was installed onto the Arduino Mega. Marlin is an open-source 3D printer firmware for platforms based on Arduino, allowing G-Code commands to be used to control the machine. For the XYZz-stage, the “Marlin-bugfix-2.0x” version was adapted to the specific properties of the XYZz-stage, such as stepper drivers and linear actuators. Detailed changes made to “Marlin-bugfix-2.0x” are described in Appendix D.

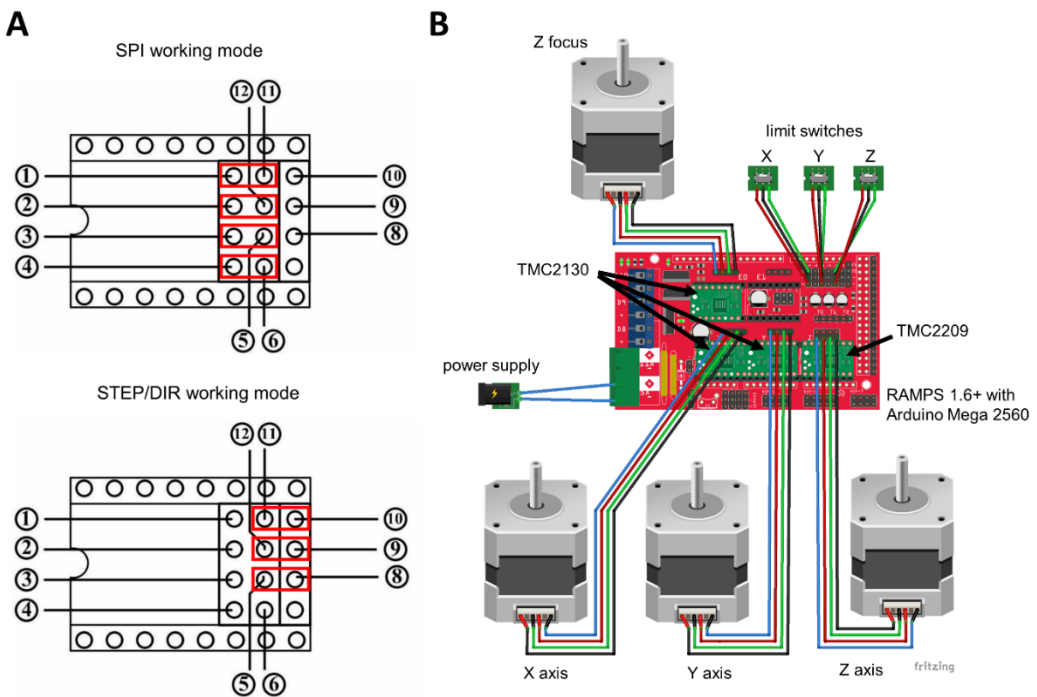


Figure 3.12 Electronics of the XYZZ-stage

(A) Selection of driving SPI and STEP/DIR working mode. The red markings indicate pins, which need to be connected by short circuit caps on the RAMPS 1.6+ board for each working mode. (adapted from RAMPS 1.6+ Datasheet). (B) Wiring diagram of RAMPS 1.6+ with connected motor drivers, stepper motor and mechanical limit switches.

Software of the OMSM

A graphical user interface (GUI) was developed to control the opto-mechatronic screening module. The GUI was written with Tkinter in Python. Two modes of the GUI were programmed; one for creating a protocol for automated imaging of up to six microwell plates and one for testing and validation experiments with a direct output. Additionally, for users with coding experience, a Python code can be written and executed as well. The XYZZ-stage is assessed by G-Codes sent via pySerial to the Arduino MEGA, connected via USB to the Raspberry Pi.

3.3 AIM 3: PROOF-OF-CONCEPT STUDY

In order to demonstrate the feasibility of the imaging module, drug response assays with established protocols were conducted on 3D tumour models. The plan was to automate the whole process from the production of hydrogels to 3D tumour model

formation, staining and imaging on the biomanufacturing platform. However, due to the Covid-19 pandemic and ongoing border closures, it was impossible to unite the biomanufacturing, located at QUT, Australia, and the opto-mechatronic screening module, located at FAU, Germany. Hence, the steps from producing the hydrogels, 3D tumour model formation, drug addition and staining procedures were done manually. Automated imaging was done on the newly developed opto-mechatronic screening module.

3.3.1 Live/dead viability assays

The same cell culture protocols were used for all experiments. Prostate cancer cells (PC-3; kindly provided by Regine Schneider-Stock, Experimental Tumorpathology, University Hospital Erlangen, Germany) were grown in RPMI 1640 cell culture medium (ThermoFisher Scientific) with 10% FBS (ThermoFisher Scientific) and 5% Penicillin/Streptomycin (Life Technologies Ltd.) in a humidified atmosphere at 37°C, 5% CO₂ until 80% confluence was reached. Cells were trypsinised with Trypsin-EDTA (0.25%, ThermoFisher Scientific), centrifuged and mixed with GelMA stock solution (150 mg/ml), PBS and photo-initiator to a 4% (w/v) GelMA-stock solution with 0.15% LAP concentration and 4x10⁵ cells per ml precursor solution and distributed to a 96 microwell plate (TPP 96 well plate, flat bottom, polystyrene, TPP Techno Plastics Products AG, Trasadingen, Switzerland). Cell-laden hydrogels were crosslinked for 4 min with a crosslinker (LunaCrosslinker, Gelomics, Brisbane, Australia) and immersed with cell culture medium. Cells were incubated in a humidified atmosphere at 37°C, 5% CO₂. Cell growth was monitored by transmission light microscopy (Nikon Eclipse TS 100, Nikon Corporation, Tokyo, Japan).

3.3.1.1 Time-dependent live/dead viability assay

After culturing the cells for one, respectively, six and eight days, cells were stained with a Live/Dead staining kit (PromoCell GmbH, Heidelberg, Germany) and imaged.

The staining kit consists of Calcein-AM to stain live cells and Ethidium Homodimer III (EthD-III) to mark dead cells. Calcein-AM is a cell-permeable dye cleaved by intracellular esterases into membrane-impermeant Calcein. While Calcein-AM is non-fluorescent, Calcein is a green-fluorescent dye with absorption and

emission maxima of 494 and 517 nm. EthD-III is a red fluorescent nucleic acid dye that stains dead mammalian cells and bacteria with absorption and emission maxima of 532 and 625 nm. It is membrane-impermeant and hence, only stains nucleic acids of cells with damaged cell membranes.

First, the cell culture medium was removed, and the gels were washed with PBS. Then, 75 μ l of staining solution containing 2 μ M Calcein-AM and 6 μ M EthD-III was added to each sample and incubated for one hour at room temperature in the dark. Z-stacks of each sample were recorded with a step size of 10 μ m with the newly developed microscope. The blue LED was used to excite Calcein AM, and the mint LED was used to excite EthD-III. The corresponding Python code to control the XYZz-stage and the microscope can be found in Appendix E.

3.3.1.2 Comparison with conventional technology

PC-3 cells were cultured as described in section 3.3.1. 4% (w/v) GelMA precursor solutions with 0.15% LAP concentration were prepared and mixed with cells to a final concentration of 5×10^5 cells/ml precursor solution. Additionally, 40,000 cells were transferred into a well of a 96 microwell plate to grow as a 2D monolayer. Cells were cultured for three days. 80 μ l of staining solution (2 μ M Calcein-AM, 4 μ M EthD-III) was added to each well and incubated for one hour at room temperature.

2D monolayers were imaged with the OMSM and a commercial microscope (Nikon Eclipse Ti, Nikon Corporation, Tokyo, Japan). For imaging of Calcein-AM, a combination of excitation filter with a bandwidth of 485/70 nm and an emission filter with 525/30 nm and for EthD-III, a combination of an excitation filter with 560/25 nm and emission filter with 607/36 nm were used on the Nikon Eclipse Ti imaging system. Images of cell-laden hydrogels were taken as Z-stacks with a step size of 10 μ m and a total Z-distance of 600 μ m on both systems.

3.3.2 Drug-response study

Two drug-response studies were performed on the OMSM to demonstrate the drug screening capabilities of the module. One endpoint drug-response study and time-dependent drug-response study, including a comparison of the influence of docetaxel on PC-3 cells on 2D and 3D cell cultures, were conducted.

3.3.2.1 Endpoint drug-response study

PC-3 cells were cultured as described in section 3.3.1. 4% (w/v) GelMA precursor solutions with 0.15% LAP concentration were prepared and mixed with cells to a final concentration of 5×10^5 cells/ml precursor solution. 60 μl of cell-laden hydrogel were distributed on a 96-microwell plate. Cell-laden hydrogels were crosslinked for four minutes with a crosslinker (LunaCrosslinker, Gelomics, Brisbane, Australia) and immersed with 200 μl cell culture medium. Cells were incubated in a humidified atmosphere at 37°C, 5% CO₂. Cell growth was monitored by transmission light microscopy.

After three days, the cell culture medium was exchanged, and docetaxel, a standard chemotherapeutic, was added. Docetaxel was dissolved in dimethyl sulfoxide (DMSO), a common solvent for drugs, and then diluted with PBS until the required concentration was reached. Docetaxel was added as triplicates in a three-point dilution series (docetaxel: 10, 100 and 1,000 μM) to the cell-laden hydrogels. As a control, DMSO and PBS were added to additional samples. After three days of incubation, the viability of the cells was assessed with a live/dead staining kit (PromoKine Live/Dead Cell Staining Kit II, PromoCell GmbH, Heidelberg, Germany). Calcein-AM was used to stain live cells and ethidium homodimer III (EthD-III) to stain dead cells.

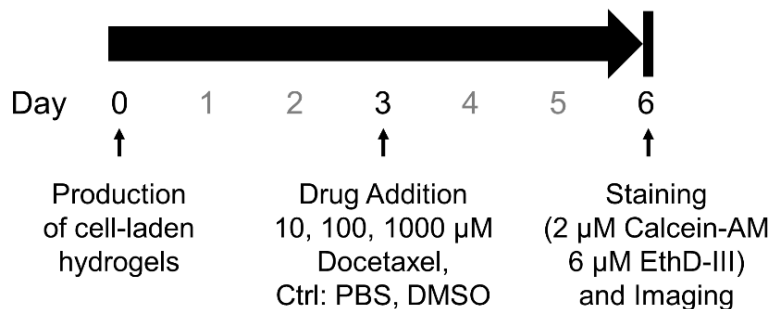


Figure 3.13 Timeline of the endpoint drug-response study

PC-3 cells were embedded in 4% (w/v) GelMA on day 0. After three days of incubation, docetaxel (10, 100 and 1000 μM), PBS and DMSO were added. Again, three days later, staining solution (2 μM Calcein-AM, 6 μM EthD-III) was added, and samples were imaged.

First, cell-laden hydrogels were washed with PBS to remove the cell culture medium. Then, Calcein AM (2 μM) and EthD-III (6 μM) were diluted in PBS, added to the cell-laden hydrogels, and incubated for 60 minutes at room temperature.

Afterwards, cells were imaged with the newly developed imaging module of the biomanufacturing workstation as described below.

3.3.2.2 Time-dependent drug-response study

PC-3 cells were cultured as described in sections 3.3.1 and 3.3.2.1. For 2D cell culture, 25,000 cells per well ($77.639 \text{ cells/cm}^2$) were seeded into a 96-microwell plate, immersed with 200 μl cell culture medium and incubated for three days at 37°C with 5% CO₂. For 3D cell culture, hydrogel precursor solutions were prepared according to the manufacturer's instructions (LunaGel™, porcine skin gelatin, photocrosslinkable extracellular matrix, low stiffness 0 – 6.5 kPa, Gelomics, Brisbane, Australia) and mixed cells to a final concentration of 1×10^6 cells/ml. 50 μl of cell-laden hydrogel were distributed to a 96-microwell plate, crosslinked (LunaCrosslinker, Gelomics) for four minutes to achieve a stiffness of approximate 4 kPa and immersed with 200 μl cell culture medium. Cell-laden hydrogels were incubated at 37°C, 5% CO₂ for six days before drug addition (Figure 3.14), with one media exchange in between. 5 mg docetaxel were dissolved in 2 ml DMSO and diluted with cell culture medium to final concentrations of 0.01, 0.1, 1, 10, 100 and 1,000 μM . Cell culture media was removed and exchanged for the docetaxel solutions. As a positive control, 40% DMSO was added, and as a negative controls, 0.4% DMSO and pure cell culture medium without drugs were used. Each experiment was performed in triplicates and repeated two times. After three, six, nine and fourteen days of drug treatment (Figure 3.14), cells were stained with a live/dead staining kit containing Calcein AM and EthD-III and imaged as described in 3.3.2.1.

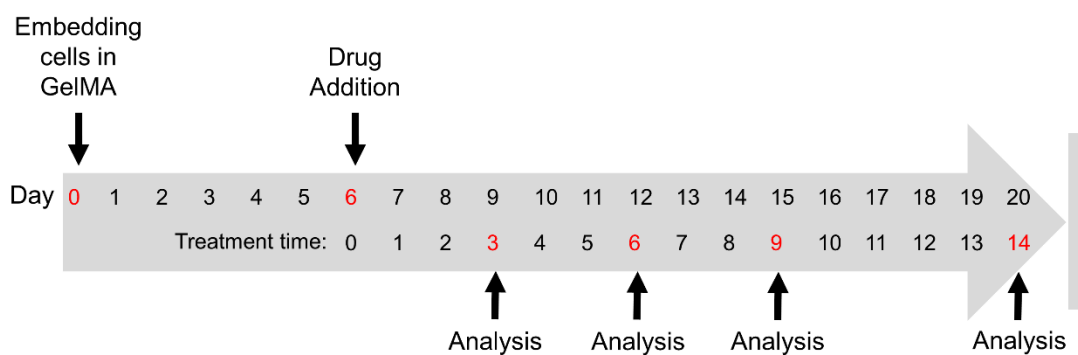


Figure 3.14: Timeline of time-dependent drug-response study

PC-3 cells were embedded in low stiffness (approx. 4 kPa) LunaGel on day 0. After six days of incubation, docetaxel (0.01, 0.1, 1, 10, 100 and 1000 μM) and DMSO (0.4%, 40%) were added. Samples were analysed after additional three, six, nine and fourteen days.

3.3.3 Imaging and image analysis

Images were taken automatically as Z-stacks, a series of XY images in Z-direction, of each sample with a fixed step size of 10 µM. At each Z-distance, an image was taken with the blue light turned on to excite Calcein-AM, and one image, with the mint LED turned on, to excite EthD-III. The corresponding code can be found in Appendix E.

Post-imaging processing is required to reduce background and out-of-focus signals. All images were analysed using ImageJ software (Fiji, NIH). Each image stack was imported as an image sequence and converted to 8-bit grayscale images. Z-projections of the individual fluorescence channels were created with max intensity, and brightness and contrast were adjusted. The background was subtracted with a rolling ball radius of 50 pixels to reduce background noise. The maximum intensity Z-projections of the image stacks, recorded with blue light, were analysed to determine the number of live cells. First, fluorescence maxima of the Z-projection were determined with the tool “Find Maxima” and “Segmented Particles” for better recognition of individual cells and segmentation of larger spheroids. Additionally, the Z-projections were binarised by defining a threshold. Before analysing the particles, the binary image and the fluorescence maxima were combined with the “Image Calculator”. For the green channel, particles with a size greater than 70 µm² to minimise detection of background noise and false detection of dead cells due to fluorescence bleed-through of red into the green channel and a circularity between 0 and 1 were analysed. For the red channel, particles with a size greater than 10 µm², to exclude noise, a circularity between 0 and 1 were analysed. The results were saved as XML files and plotted with SigmaPlot. The viability was calculated as the number of live cells as the percentage of the sum of live and dead cells per image or Z-stack, respectively:

$$Viability = \frac{count_{live\ cells}}{count_{live\ cells} + count_{dead\ cells}} \quad \text{Equation 3.8}$$

3.3.4 Statistical analysis

Statistical analysis was performed using SigmaPlot 14.0. One Way ANOVA was used for comparison between treatment groups and null hypothesis tests (endpoint drug-response study n = 10; time-dependent drug-response study n = 12). Tukey-test was used for all pairwise multiple comparisons if the normality test (Shapiro-Wilk)

failed. Nonlinear regression for the determination of the half maximal inhibitory concentration (IC_{50}) of docetaxel was performed using SigmaPlot based on a four-parameter logistic curve:

$$y = min + \frac{max - min}{1 + \left(\frac{x}{IC_{50}}\right)^{-Hillslope}} \quad \text{Equation 3.9}$$

with min = minimum possible value, max = maximum possible value, IC_{50} = half maximal inhibitory concentration, $Hillslope$ = slope factor for the steepness of the curve and the following constraints: $IC_{50} > 0$, $0 < min < max$, $max_{viability} < 100$.

Chapter 4: Results

This chapter describes the results of the methods detailed in Chapter 3: Section 4.1 shows the results of aim 1, the validation of the biomanufacturing workstation, with the implementation of an automated and reproducible workflow for the manufacturing of GelMA-based hydrogels (4.1.2), a parameter library based on a DoE approach (4.1.2), and an algorithm, *MechAnalyze*, for the automated analysis of unconfined compression test data (4.1.3). The results of aim 2, the integration of an imaging module, are described in chapter 4.2. Section 4.2.1 specifies the OMSM and its integration into the biomanufacturing workstation. The validation of the microscope and the XYZz-stage are summarised in sections 4.2.2 and 4.2.3, respectively. Section 4.2.4 presents the software-based integration and the graphical user interface of the OMSM. The last section 4.3 of this chapter, shows the results of the proof-of-concept studies. Time-dependent live/dead cell viability assays and their comparison with conventional technology are pictured in 4.3.1. Section 4.3.2 presents the results of an endpoint and a time-dependent drug-response study.

4.1 AIM 1: VALIDATION OF THE BIOMANUFACTURING WORKSTATION

4.1.1 Implementation of an automated and reproducible workflow for manufacturing of gelatin methacryloyl (GelMA)-based hydrogels

4.1.1.1 *Influence of microwell plate type*

The compressive modulus of GelMA hydrogels (5%, 10%) manufactured in different kinds of microwell plates (transparent, white, black/clear bottom) was compared. The compressive modulus of 5% GelMA hydrogels crosslinked for six minutes in a white microwell plate was 7.4 ± 2.1 kPa, in a black/clear bottom plate 5.6 ± 0.5 kPa and in transparent one 12.9 ± 7.0 kPa. For 15% GelMA hydrogels, the compressive modulus was in a white plate 48.7 ± 8.9 kPa, in a black one 36.3 ± 10.2 kPa and in a transparent one 49.7 ± 5.4 kPa (Figure 4.1). The data were analysed with SPSS (IBM SPSS Statistics 25) using a 2-way-ANOVA. There were no significant differences between the kinds of plates within one hydrogel concentration. Therefore, we decided to use transparent microwell plates for further experiments since these are inexpensive and suitable for imaging.

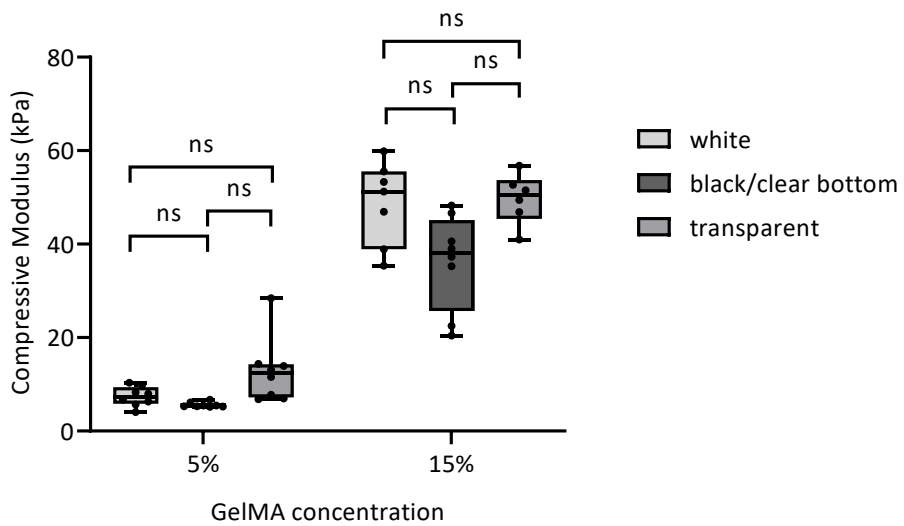


Figure 4.1 Influence of three different microwell-plate types on the compressive modulus of GelMA hydrogels

The boxplot indicates the median (line), 25th and 75th percentile (box), the minimum and the maximum value (whiskers) of eight replicates (ns = not significant, ANOVA).

4.1.1.2 *Influence of LAP concentration*

In order to assess the influence of the photo-initiator concentration, the compressive modulus was measured of GelMA hydrogels with 0.15% and 0.30% LAP concentration. Both concentrations are within a range which is also commonly used for bioprinting [111]. Figure 4.2 shows that the compressive modulus increased significantly ($p < 0.001$, ***) with increasing LAP concentration.

Interestingly, there was no significant difference between the three different exposure times in this system. This indicates that full crosslinking has been achieved following two minutes of exposure, and no further influence of the exposure time on the compressive modulus was observed.

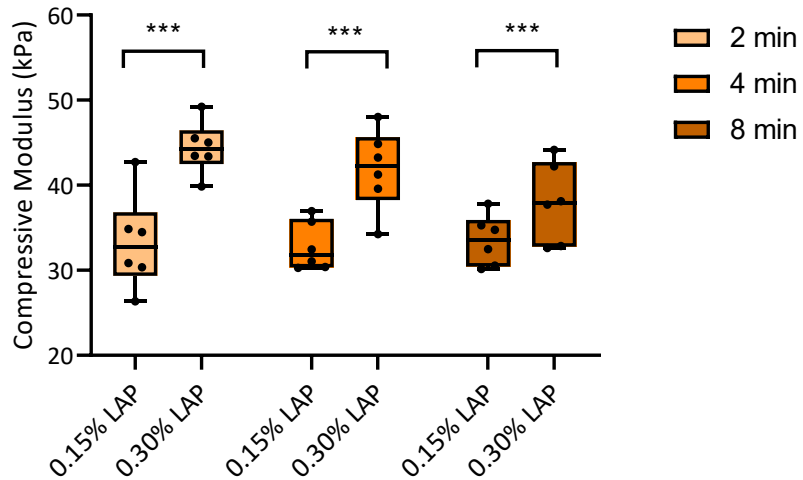


Figure 4.2 Compressive moduli of 10% GelMA and 0.15% (0.30%) LAP concentration crosslinked for 2, 4 and 8 min

The boxplot indicates the median (line), 25th and 75th percentiles (box), minimum and maximum value (whiskers) of six replicates (** p < 0.001, ANOVA).

4.1.1.3 Optimisation of mixing step

Initial trials of manufacturing hydrogels demonstrated variability of the compressive modulus caused by incomplete mixing of the GelMA stock solution, PBS and photo-initiator; hence optimisation of the mixing step was necessary. To increase reproducibility and minimise the variation of manufactured hydrogels, the mixing of 20% GelMA stock solution with PBS and LAP to produce hydrogels of lower polymer concentration was optimised.

The standard mixing command of the OpenTrons OT-1 pipetting unit consists of an aspiration step immediately followed by a dispensing step of a specified volume at a fixed position in the tube. This aspiration and dispensing step can be repeated as many times as specified. This can be described with the following command line:

```
pipette.mix(4, 1000, heatingblock.wells('A2').bottom(5)) [84]
```

This means, 1000 µl of the solution is aspirated and dispensed in well ‘A2’ of the heating block 5 mm above the calibration point. Therefore, the plunger of the pipette moves up and down while the pipette itself does not move.

In order to optimise the mixing of viscous materials, the manual movement of a pipette during mixing was mimicked. While aspirating, the pipette moves with the falling liquid level down and then moves up again while dispensing the liquid from

the pipette. For further reference, this movement is named ‘smooth mixing’. To implement smooth mixing into the pipetting robot, not only the plunger but also the pipette itself have to move at the same time. To operate smooth mixing, the function ‘smoothMix’ has been written in python (Appendix F).

The results of the absorbance measurements of the mixing optimisation are shown in Figure 4.4. A detailed overview of all mixing step optimisation experiments and their protocols can be found in Appendix G.

In experiment 1 (Figure 4.4, 1) are three controls: Protocol 1 is only PBS without Orange G, protocol 8 is PBS and PBS + Orange G of a ratio 1:1 and protocol 7 has been manually mixed. Protocols 2 – 6 were produced automatically according to different mixing procedures resulting in insufficient mixing. The samples taken in the upper part of the tube (sample positions 1 and 2) have a higher absorption of Orange G than the samples taken in the lower part of the tube (sample positions 3 and 4). This means that in the upper part of the tube was more PBS, and the concentration of GelMA is lower than at the bottom of the tube, and therefore, the applied mixing protocol distributed GelMA not sufficiently throughout the tube. Therefore, an additional aspirating and dispensing step was introduced into the mixing protocol. The upper layer of the solution, with a low GelMA concentration, is aspirated, dispensed further down and immediately mixed at this position by aspirating and dispensing two more times. Figure 4.4, 2 shows that no trend in the tube is observable anymore. Nevertheless, the relative standard deviations were still around 6 to 30%. In Figure 4.4, 3 the mixing protocols were extended by introducing more aspirating and dispensing steps at various positions reducing the CV down to 3.7% for sample number 17a and 4.7% for 17b, which was mixed with the same protocol in another tube. It was observed that small amounts of hydrogel attached to the outside of the tip influenced the amount of hydrogel dispensed into a well. Therefore, a cleaning step was introduced thus, removing excess hydrogel. The excess hydrogel was absorbed by moving the tip for a second onto a sheet of lint-low tissue (Kimwipes, Kimtech Sciences). Sample 21a, 22a and 23a in Figure 4.4, 4 are without and samples 21b, 22b and 23b are with this cleaning step, which reduced CV down to 3.5% for sample 23b. To further minimise the standard deviation and shorten the duration of the mixing step, the aspiration and dispensing speed was increased (Table 4.1). By increasing the

dispensing speed, the CV could be reduced to less than 5% for all samples, and the duration of the mixing step could be reduced by more than half of the time.

Table 4.1 Mixing optimisation experiment 5 – decrease in duration of mixing step by increasing dispension speed

Sample Number	Dispension Speed (mm/min)	CV	Time (min:sec)
24	800	4.5%	07:30
25	800	2.0%	05:42
26	1000	2.5%	04:47
27	1200	2.8%	04:10
28	1400	2.2%	03:56
29	1000	2.0%	03:10
30	1200	1.5%	03:00
31	1400	2.5%	02:45

The optimised mixing step (Figure 4.4) consists of a smooth mixing, which is operated ten times, then 1000 µl of the upper layer are aspirated and dispensed further down. At this position, 1000 µl are mixed two times by pipetting up and down, which is repeated at two more positions further up in the tube. Then, the upper layer of 1000 µl is aspirated again, dispensed further down and mixed two times. The entire mixing step is then finished with ten times of the smooth mixing step (Appendix H).

To study if the optimised mixing step not only mixes 10% GelMA gels well but also higher and lower concentrations, the protocol was also applied for 5% and 15% GelMA hydrogels. Sample 32 and 33 in Figure 4.5 are 5%, and samples 34 and 35 are 15% GelMA gels with a CV between 2 and 5%. This implies that the same mixing protocol can also be applied for gels of higher and lower GelMA concentrations.

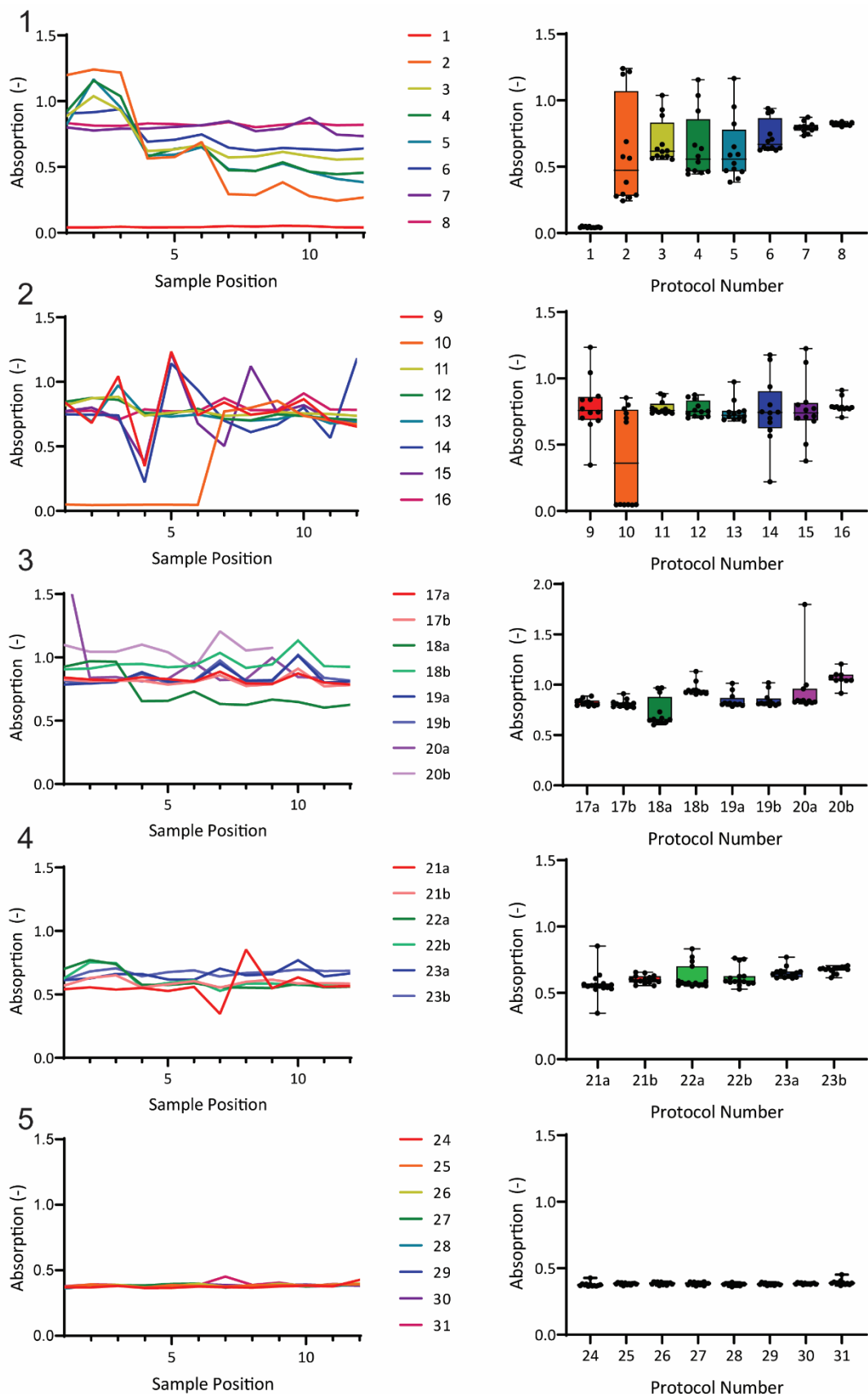


Figure 4.3 Mixing optimisation – absorption measurements of 10% GelMA manufactured with PBS mixed with Orange G

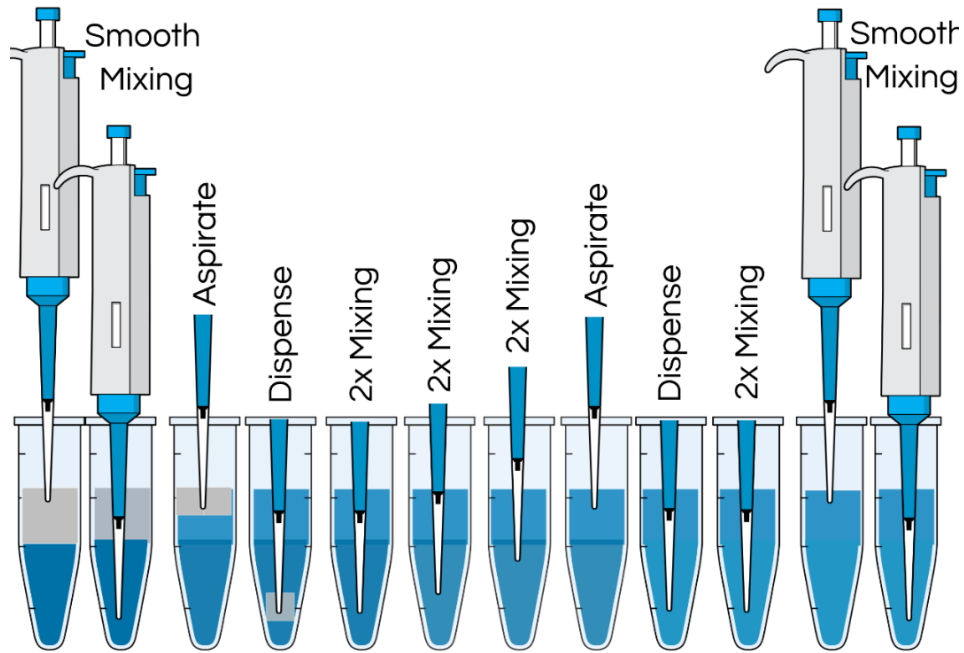


Figure 4.4 Optimised automated mixing step

The optimised mixing step consists of smooth mixing, repeated ten times, an aspirating and dispensing step, three standard mixing steps, each two times in the lower, middle and upper part of the tube, another aspirating/dispensing step followed by a standard mixing step two times and finished with smooth mixing for ten times. Schematic only.

So far, the efficiency of mixing has been analysed by absorbance measurement of Orange G. In Figure 4.6, the compressive modulus of 5%, 10% and 15% GelMA hydrogels manufactured with the optimised mixing protocol was determined. The CV is with 6%, 10% and 30%, respectively, higher than in the absorbance measurements, but these values are comparable with STD from manually produced hydrogels from the literature [29], [112]–[114] and experiences in our group. In a replicate, the mean compressive modulus could be reproduced with $R^2 = 1$ (Figure 4.6, C and D), indicating an increase in reproducibility.

Figure 4.3 Mixing optimisation – absorption measurements of 10% GelMA manufactured with PBS mixed with Orange G

The graphs in the left column indicate the individual absorption at each position, where the sample has been taken for better visualisation of trends throughout the tube, e.g. sample positions 1, 2 and 3 are in the upper layer of the tube, 10, 11 and 12 are on the bottom. Boxplots in the right column illustrate the distribution and their deviation. Please refer for the conditions of experiments (1) to (5) to the main text and Appendix G. Boxplot indicates median (line), 25th and 75th percentile (box), minimum and maximum value (whiskers) of three replicates from four positions within one sample ($n = 12$).

(Adapted from Eggert et al. [115])

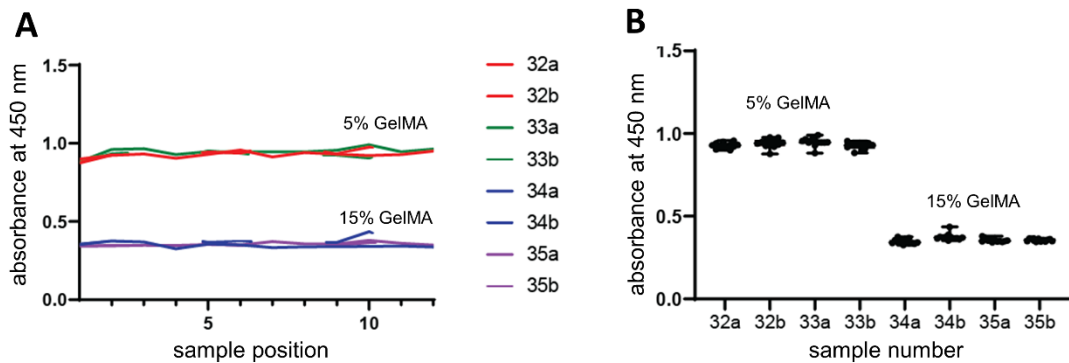


Figure 4.5 Optimised mixing protocols for 5% and 15% GelMA hydrogels

5% gels were produced according to protocols 32 and 33, 34 and 35 refer to 15% gels. The graph (A) on the left side indicates the absorption of each individual sample and the boxplot on the right side (B) displays the variation of the absorption. The boxplot indicates the median (line), 25th and 75th percentile (box), the minimum and maximum value (whiskers) of three replicates from four positions within one sample ($n = 12$, adapted from Eggert et al. [17]).

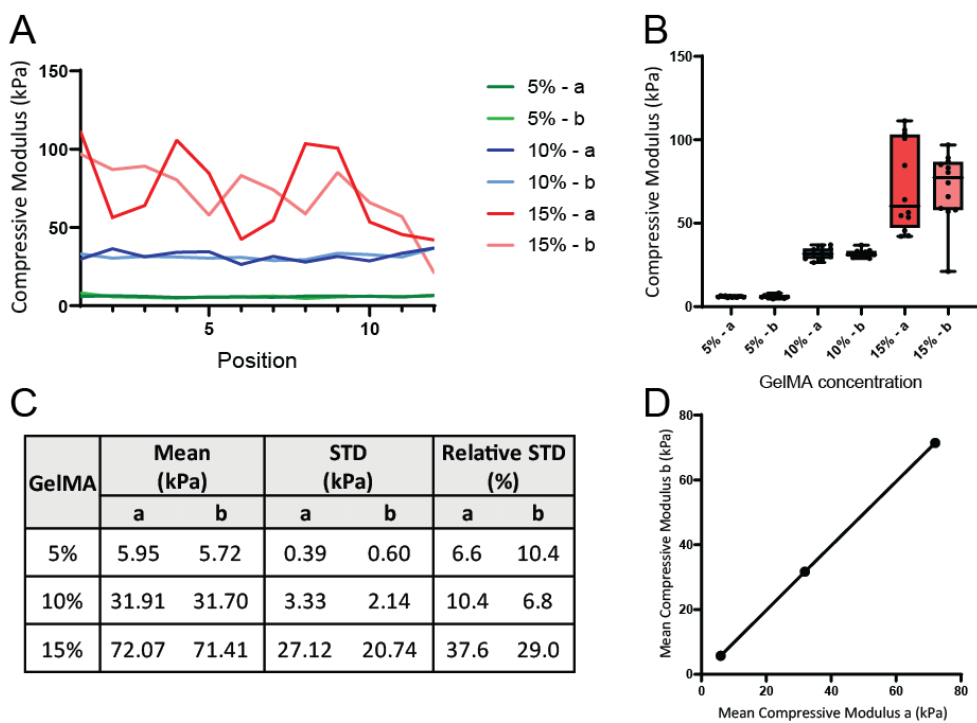


Figure 4.6 Reproducibility of crosslinked GelMA hydrogels

(A) Compressive modulus of each individual sample of 5%, 10% and 15% GelMA hydrogels according to their position taken. (B) Variation of the compressive modulus is shown in (A). The boxplot indicates the median (line), 25th and 75th percentile (box), the minimum and maximum value (whiskers) of three replicates from four positions within one sample ($n = 12$). (C) Mean, STD and relative STD of compressive modulus for 5%, 10% and 15% gels of experiment a and its replication b. (D) Correlation of the means of compressive moduli of experiment a with experiment b.

4.1.2 Conception of a parameter library to produce GelMA-based hydrogels with specific mechanical properties

Figure 4.7 shows the 4D response contour plot of the compressive modulus as a function of curing light intensity, exposure duration and GelMA concentration. The prediction of the compressive modulus is mapped for three light intensities 0.5 mW cm^{-2} , 2.25 mW cm^{-2} and 4 mW cm^{-2} . By using this diagram, the compressive modulus for each combination of GelMA concentration and exposure time for a given light intensity can be determined. The diagram indicates that the concentration of GelMA has the strongest influence on the compressive modulus, and exposure time and light intensity only have a minor influence.

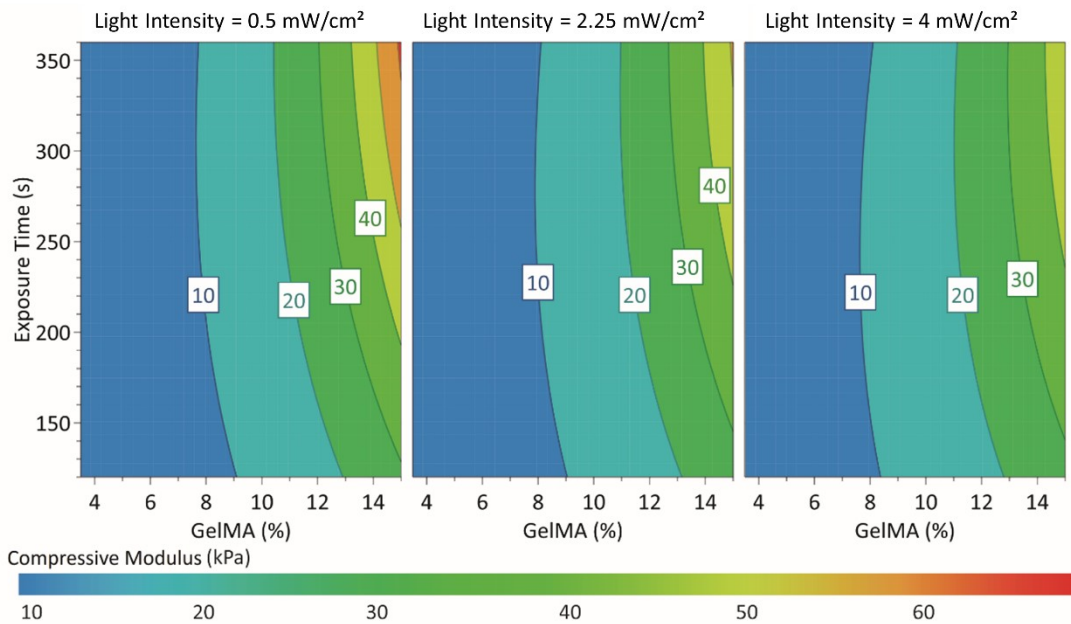


Figure 4.7 Parameter library

4D Response Contour Plot of the compressive modulus (kPa) for a constant light intensity of 0.5 mW/cm^2 (left), 2.25 mW/cm^2 (middle) and 4 mW/cm^2 (right)
(adapted from Eggert et al.[115]).

The results of the model analysis are shown in Appendix I. The data showed a positive skewness; therefore, the response data were log-transformed to a normal distribution. The coefficient plot also shows that the GelMA concentration had the strongest influence on the compressive modulus, the light intensity had no influence, and the exposure time had only a minor influence. From the interaction of these parameters, only the interaction of the GelMA concentration with the exposure influences the compressive modulus. The model fit R² is significant, with a value of

0.917. An estimate about the future prediction precision had a Q2 value of 0.895, which means it will be a good model. The model validity of 0.827 indicates that there are no diverse model problems. The reproducibility, which is the variation of the replicates compared to the overall variability, is 0.907.

4.1.3 Automated analysis of compression test data with *MechAnalyze*

All results presented in this chapter are published in “*MechAnalyze*: An Algorithm for Standardization and Automation of Compression Test Analysis” by Kahl et al. [108]. This study aimed to evaluate the suitability of the newly developed algorithm *MechAnalyze* to analyse unconfined compression test data in an automated manner. For this purpose, a total of 711 mechanical testing data, of which 465 were compressed until failure, were analysed. The dataset, which was divided into 5 subsets, each provided by an individual researcher, was analysed both manually by each researcher, who provided the data, and automatically with *MechAnalyze*, and then the results were compared with each other.

As outlined in section 3.1.1.2, *MechAnalyze* determines the sample height from the force-displacement data generated in unconfined compression tests as the displacement value at which the force starts deviating from the baseline. Then, this value is defined as 0% strain. The algorithm calculates the corresponding stress, normalised to the sample’s surface area. In a first run, the sample height of all data was determined by *MechAnalyze*. Visual QC identified the correct determination of sample height in 90% of the cases. The sample height of the remaining samples was determined by visual inspection and corrected for re-analysis.

4.1.3.1 Comparison of manual and automatically analysed data

Figure 4.8 shows the linear regression between manual and automated data analysis as well as the corresponding Bland-Altman plots to assess the mean difference between both analysis methods. For this purpose, each dataset of each individual researcher is colour-coded.

R^2 of 0.897, 0.928, 0.943, and 0.645 were calculated with linear regression analysis for sample height (Figure 4.8 A), compressive moduli (Figure 4.8 C), failure stress (Figure 4.8 E), and failure strain (Figure 4.8 G), respectively, indicating good conformity of both analysis methods across all user datasets.

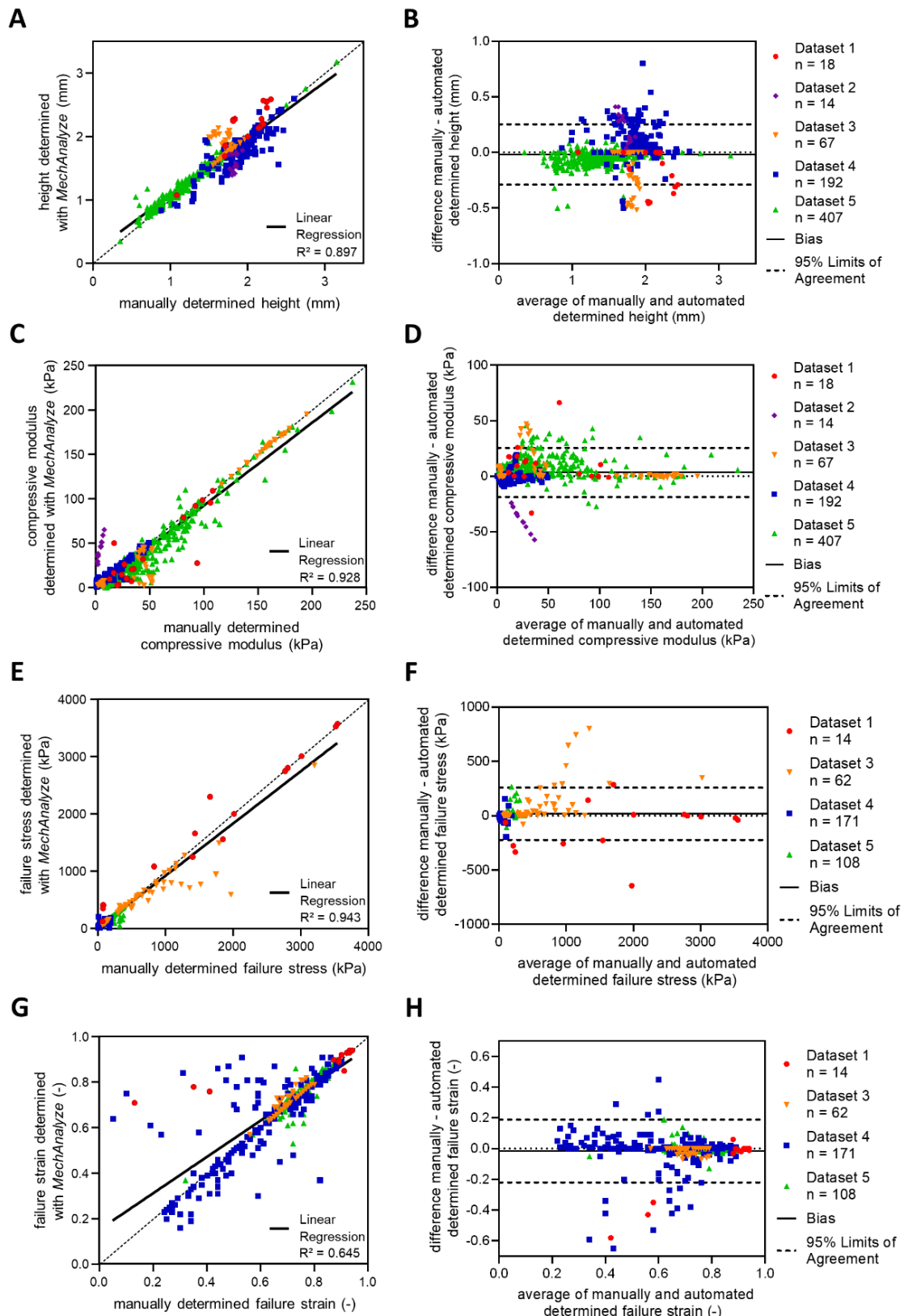


Figure 4.8 Comparison of manual and automatically analysed compression test data

The differences in the determined mechanical parameter values were plotted against their respective averages in Bland-Altman plots to examine the agreement of manual and automated analysis methods (Figure 4.8). The mean difference between both analysis methods for each parameter was identified with the Bland-Altman plot. For the determination of the sample height, the mean difference was -0.02 mm, which corresponds to an error of 1% (Figure 4.8 B). This means that, on average, the automated analysis determined a 0.02 mm lower sample height than manual analysis. For compressive moduli ranging between 1 and 200 kPa, the mean difference was 3.34 kPa, corresponding to a mean error of 10%, indicating that *MechAnalyze* calculated a slightly higher compressive modulus than manual analysis methods. The mean difference for failure stress determination, for values ranging between 0 and 3,000 kPa, was 17.92 kPa with an error of 7%. The mean difference for the determination of failure strain was 2% with an error of -2% strain.

4.1.3.2 Variability of datasets between manual analysis of independent researchers and MechAnalyze

An independent analysis of goodness of fit for each user dataset shows that the R^2 varied substantially between users and their analysis of mechanical parameters. This indicates a high user-to-user variability with a bias of manual workflows. Interestingly, the coefficient varied most between users for the determination of sample height, as this parameter is highly dependent upon the user's interpretation of the raw data.

Figure 4.8 Comparison of manual and automatically analysed compression test data

(A) Linear regression between manually determined height (mm) and height determined with *MechAnalyze* (mm) of dataset 1 – 5 ($n = 698$) with R^2 of 0.8965 and (B) its corresponding Bland-Altman plot with the difference and average of both methods with a mean difference of -0.02 mm. The *black line* indicates the mean difference, and the *dashed line* the 95% confidence interval. (C) Linear regression between both methods for the determination of the compressive modulus ($n = 698$) with R^2 of 0.9280 and (D) its corresponding Bland-Altman plot with a mean difference between methods of 3.34 kPa. (E) Linear regression of failure stress ($n = 355$) with R^2 of 0.9425 and (F) its corresponding Bland-Altman plot with a mean difference of 17.92 kPa. (G) Linear regression of the failure strain ($n = 355$) with R^2 0.6452 and (H) its corresponding Bland-Altman plot with a mean of -0.02. Each colour corresponds to one dataset analysed manually by one independent researcher: red = dataset 1, purple = dataset 2, orange = dataset 3, blue = dataset 4, green = dataset 5
 (adapted from Kahl et al. [108]).

The user-specific R^2 values for the analysis of the compressive modulus were in the range between 0.750 and 0.968, for failure stress between 0.591 and 0.967 and for failure strain between 0.577 and 0.909 (Figure 4.9). The corresponding errors (Figure 4.9) varied between -9% and 13% for the determination of height, between -167% and 22% for the compressive modulus, between -11% and 20% for failure stress, and between -12% and 0% for the determination of failure strain (Figure 4.9 B).

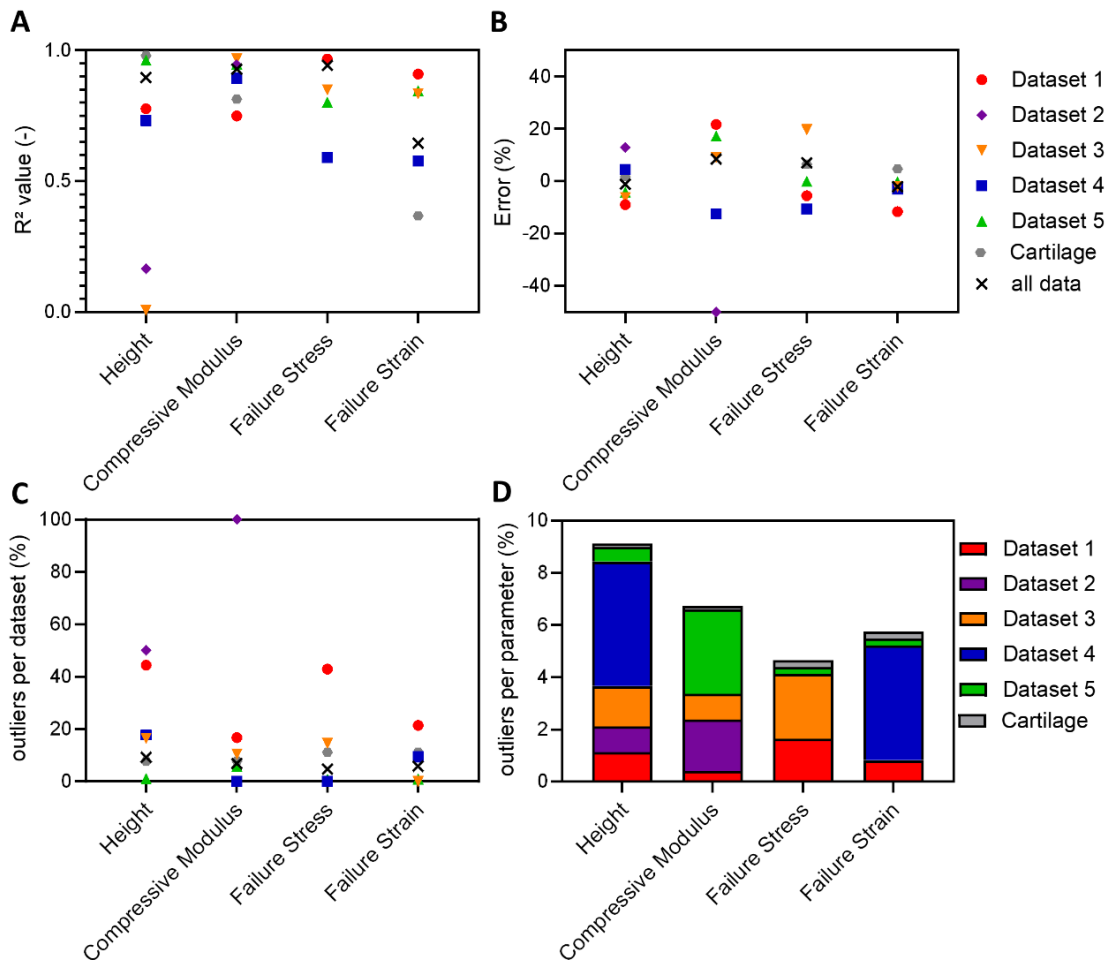


Figure 4.9 Variability of manually analysed datasets between individual researchers and *MechAnalyze*

(A) R^2 values of the correlation between analyses performed using *MechAnalyze* and by independent researcher providing datasets generated in compression tests of hydrogels, engineered tissues and native cartilage and **(B)** the corresponding error for each parameter. The black cross indicates the mean R^2 , respectively error, of all datasets together (n [height, compressive modulus] = 698, n [failure stress, failure strain] = 355). **(C)** Relative abundance of outliers for each mechanical parameter per dataset/user. **(D)** The relative contribution of outliers of each dataset/user to the total number of determined outliers. (Dataset 1: GelMA- and alginate-based hydrogels and engineered tissues; dataset 2, 3, and 5: GelMA-based hydrogels and engineered tissues; dataset 4: placenta-derived hydrogels)
(adapted from Kahl et al. [108]).

Additionally, the presence of outliers, which are defined as values outside the 95% confidence interval, was similarly dependent on users and parameters, as the data suggested. Some users and/or datasets had a substantially higher number of outliers in their manually analysed data than other users, whose data corresponded better with the results of the *MechAnalyze* algorithm (Figure 4.9 C, D).

4.2 AIM 2: INTEGRATION OF AN IMAGING MODULE

This chapter describes the opto-mechatronic screening module (OMSM) and its integration into the biomanufacturing workstation. The results of the microscope validation, as well as the image and axial resolution, are presented in section 4.2.2, and the results of the validation of the XYZz-stage are described in section 4.2.3. A graphical user interface to operate the OMSM is presented in section 4.2.4. The design of the OMSM and its application with the time-dependent drug-response study have been also published in “A fluorescence-based opto-mechatronic screening module (OMSM) for automated 3D cell culture workflows” by Kahl et al. [116].

4.2.1 The opto-mechatronic screening module and its integration into the workstation

The OMSM is a stand-alone device for automated fluorescence imaging. Since it was initially developed as an analysis module for the biomanufacturing workstation, it can be easily integrated and added to the workstation in line with the linear assembly approach (Figure 4.10). The module consists of a custom-engineered inverted widefield fluorescence microscope and an XYZz-stage. The XYZz-stage is comprised of an X-stage, Y-stage, Z-coarse (indicated as an uppercase Z in “XYZz-stage”) and Z-fine stage (indicated with a lowercase z in the notation “XYZz-stage”). The X-stage moves tissue culture plates in and out of the storage rack and is responsible for moving the plate between individual wells for imaging. The Y-stage moves tissue culture plates between individual wells for imaging. The tissue culture plates are placed on a gripper mounted onto the Y-stage. The Z-coarse axis, on which the X- and Y-stages are mounted, moves tissue culture plates from the storage rack above the microscope and back. The Z-fine stage, on which the objective of the microscope is mounted, moves the objective to allow focusing and Z-stacking. The body of the microscope, comprised of an illumination unit with two LEDs, a filter cube, a tube lens and a camera, is attached to an optical breadboard, which is mounted on the aluminium profiles of the bottom of the frame.

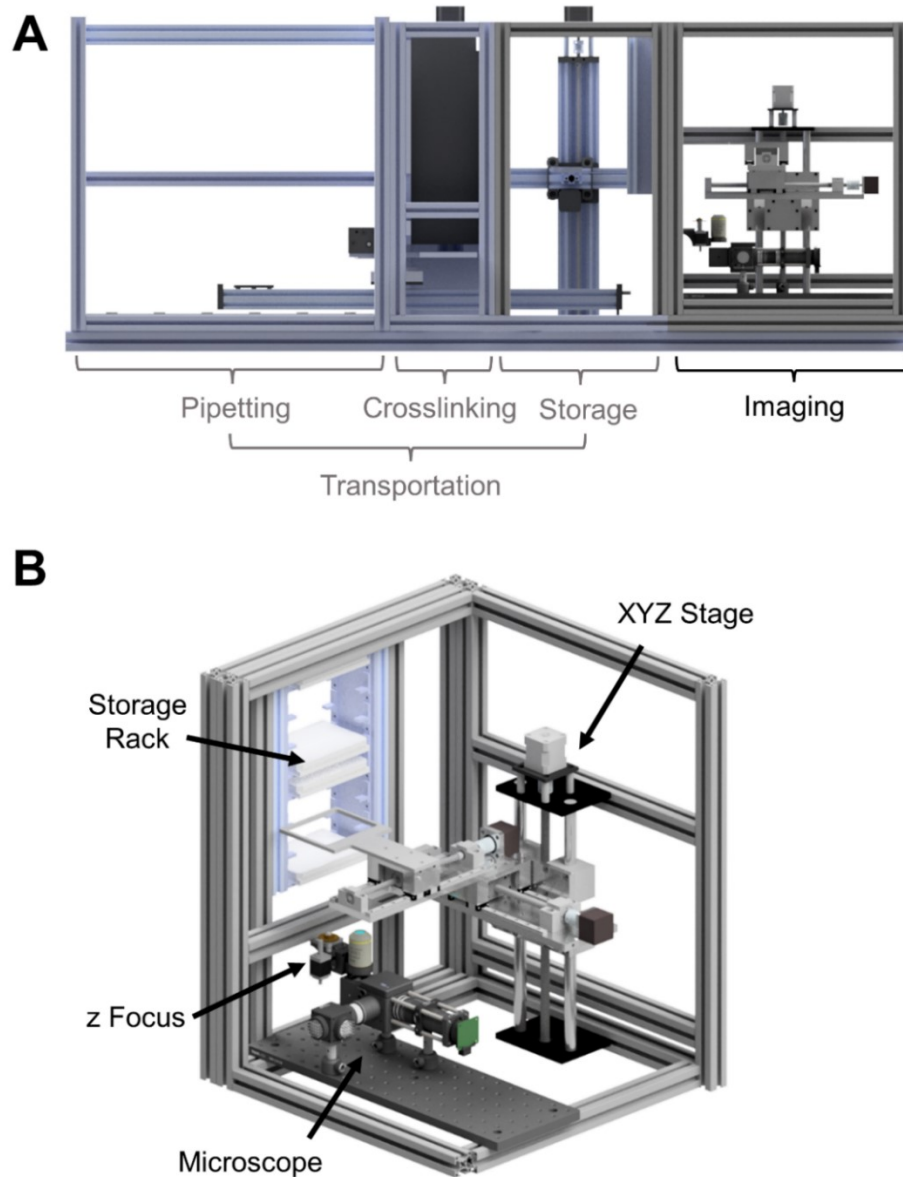


Figure 4.10 Opto-mechatronic screening module and its integration into the biomanufacturing workstation

(A) Integration of the OMSM into the biomanufacturing workstation. The workstation consists of a pipetting, crosslinking and storage module connected through a transportation unit. The OMSM can be connected to the right side of the storage module and access the tissue culture plates stored in the storage rack. **(B)** Detailed view of the OMSM with the XYZ-stage, z-focus and microscope. (Some aluminium profiles in the front were removed in the CAD drawing to better illustrate of the other components).

4.2.2 Validation of the microscope

Since the microscope was built from individual components, the resolution and fluorescence capabilities of the microscope had to be explicitly measured. The image

resolution and contrast capabilities, measured with a 1951 USAF test target, are described in 4.2.2.1. The axial resolution was measured with image recordings of microspheres embedded in GelMA, described in 4.2.2.2. Imaging and analysis of fluorescent microspheres embedded in GelMA to demonstrate the microscope's capability of fluorescence imaging and Z-stacking are shown in 4.2.2.3.

4.2.2.1 Image resolution and contrast

To measure the microscope's resolution and contrast capacity, a 1951 USAF test target was imaged. As all line pairs, up to the smallest ones of group 7, element 6, are resolvable, the maximum resolution is greater than 228.0 line pairs per millimetre (Figure 4.11A). The red line marks the measurement of the contrast, displayed in Figure 4.11 B, as grey values against distance in pixels. By measuring the line length of one element, the pixel size and field of view were determined. Having a camera setting with a resolution of 2,028 pixels by 1,520 pixels, the size of one pixel is 0.619 μm by 0.619 μm (Figure 4.11 C).

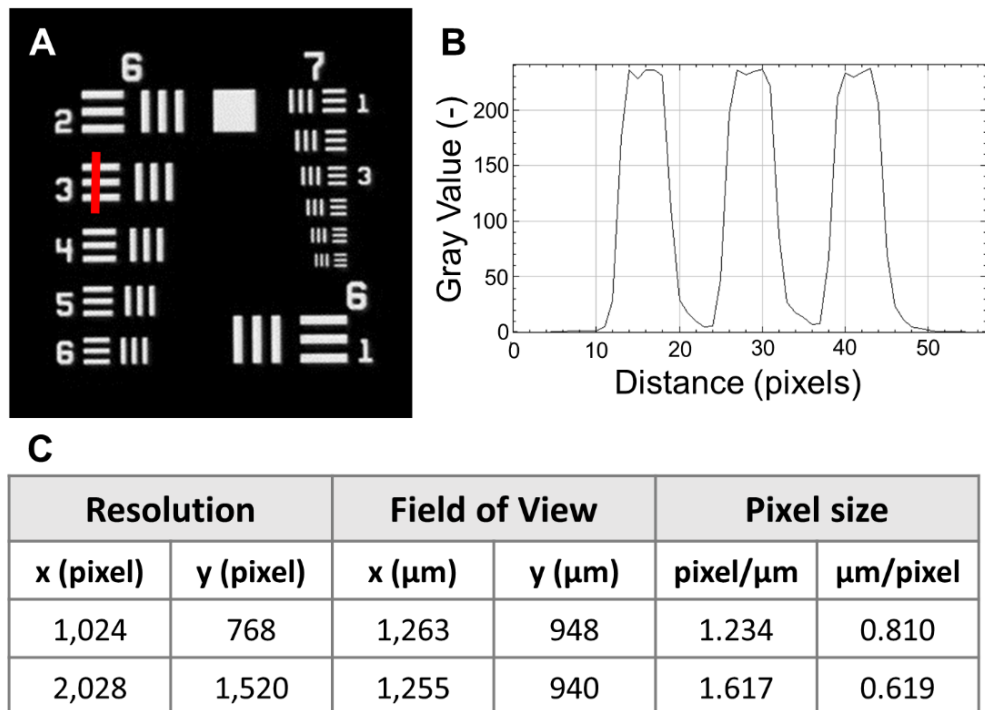


Figure 4.11 Resolution and contrast of the Raspberry Pi HQ camera

(A) Image of a 1951 USAF test target, taken with a 10X objective and the Raspberry Pi HQ camera. The red line indicates the area in which the contrast was measured. (B) Grey values of the area of the test target marked in A. (C) Table of the field of view and pixel size for two resolution settings of the camera.

4.2.2.2 Axial resolution

In order to determine the axial resolution, Z-stacks of fluorescent microspheres with a defined diameter ($2.5\text{ }\mu\text{m}$) embedded in 5% GelMA were imaged (Figure 4.12 A), and X-Z planes were generated with the “Reslice” function of ImageJ (Figure 4.12 D).

The average width in X direction was $3.9\text{ }\mu\text{m}$ ($n = 10$), which is $1.5 \times$ of the actual size of the microsphere. The average length (in Z-direction) was $57.5\text{ }\mu\text{m}$, which is 23 times greater than the actual size. This is also recognisable in the X-Z of a recorded microsphere, showing an elliptical shape with a tail in the lower part (Figure 4.12 D). In X-direction, a full width of half maximum (FWHM) of $1.1\text{ }\mu\text{m} \pm 0.1\text{ }\mu\text{m}$, in the Y-direction an FWHM of $1.2\text{ }\mu\text{m} \pm 0.1\text{ }\mu\text{m}$ and in Z-direction an FWHM of $16.8\text{ }\mu\text{m} \pm 0.0\text{ }\mu\text{m}$ (Figure 4.12 B) was determined using ImageJ’s plugin PSFj [110].

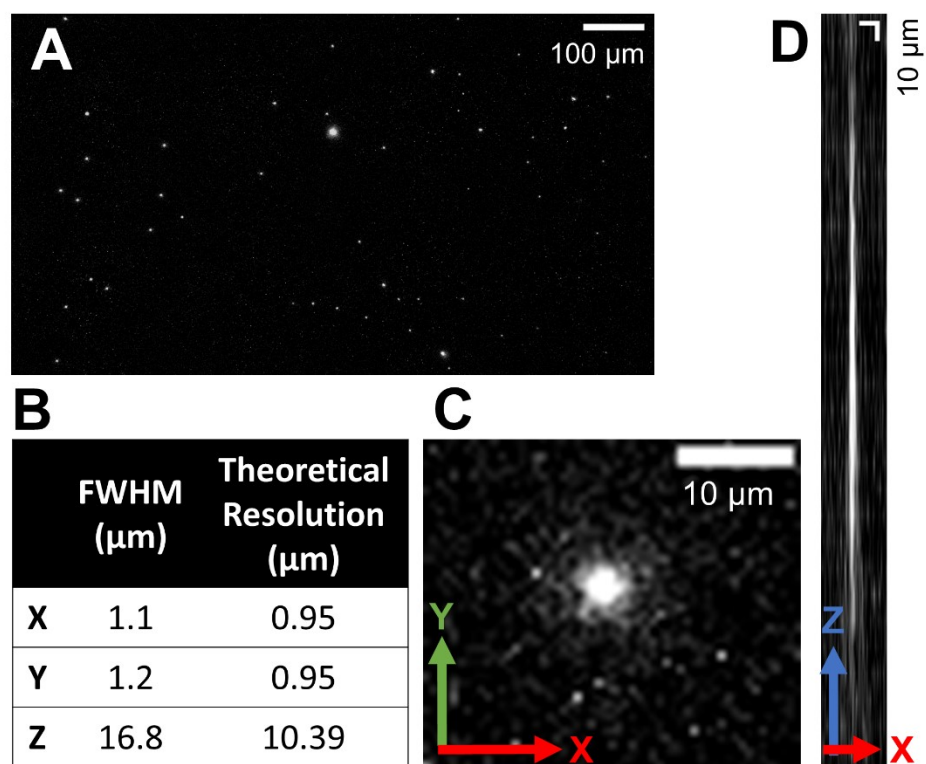


Figure 4.12 Axial resolution of the microscope

(A) XY view of a maximum Z-projection of the complete Z-stack of embedded microspheres. Scale bar = $100\text{ }\mu\text{m}$. (B) Full-Width-at-Half-Maximum (FWHM) and theoretical resolution for X, Y and Z (C) Maximum Z-projection of an XY view of a fluorescent microsphere with a diameter of $2.5\text{ }\mu\text{m}$. Scale bar = $10\text{ }\mu\text{m}$. (D) Maximum Y-Projection of an XZ view of the same microsphere with a step size of $12.5\text{ }\mu\text{m}$. Scale bar = $10\text{ }\mu\text{m}$.

4.2.2.3 Microsphere validation

Green fluorescent microspheres in concentrations between 50 and 1,000 microspheres/ μl were mixed with GelMA precursor solution, distributed to wells of 96 micowell plate and imaged as Z-stacks to generate a calibration curve and validate the imaging capabilities of multiple concentrations of fluorescent particles.

The number of particles in the Z-projection images of the recorded Z-stacks increases with the initial concentration of microspheres in the hydrogel precursor solution (Figure 4.13). Linear regression analysis between the counted particles of a Z-projection image and the initial microsphere concentration in the hydrogel resulted in an R^2 of 0.986, indicating a strong correlation between the initial microsphere concentration and the number of analysed particles in the Z-projections of the recorded images.

4.2.3 Validation of the XYZz-stage

In order to determine the XYZ-stage's repeatability and accuracy, the carriage of each axis was moved from the calibration point to the measurement point 20 times, as shown in Figure 4.14 A, and the deviation between each repetition was measured. The X- and Y-axis deviation was measured by taking images of a 1951 USAF test target with the microscope setup and subsequent image analysis with ImageJ. However, this method was not possible in Z-direction. Hence, the deviation of the Z-fine axis was measured by using a dial gauge, and the deviation of the Z-coarse axis was measured by using a calliper due to the greater travel distance between calibration and measurement point.

The determined repeatabilities (mean) were between 0 μm for the Z-fine axis and 1.7 μm for the Y-axis (Figure 4.14 B, C). The Z-fine axis has the highest accuracy (standard deviation) with 1.4 μm ; the accuracy for the X-axis was 2.4 μm and the Y-axis 2.6 μm , respectively (Figure 4.14 B, C).

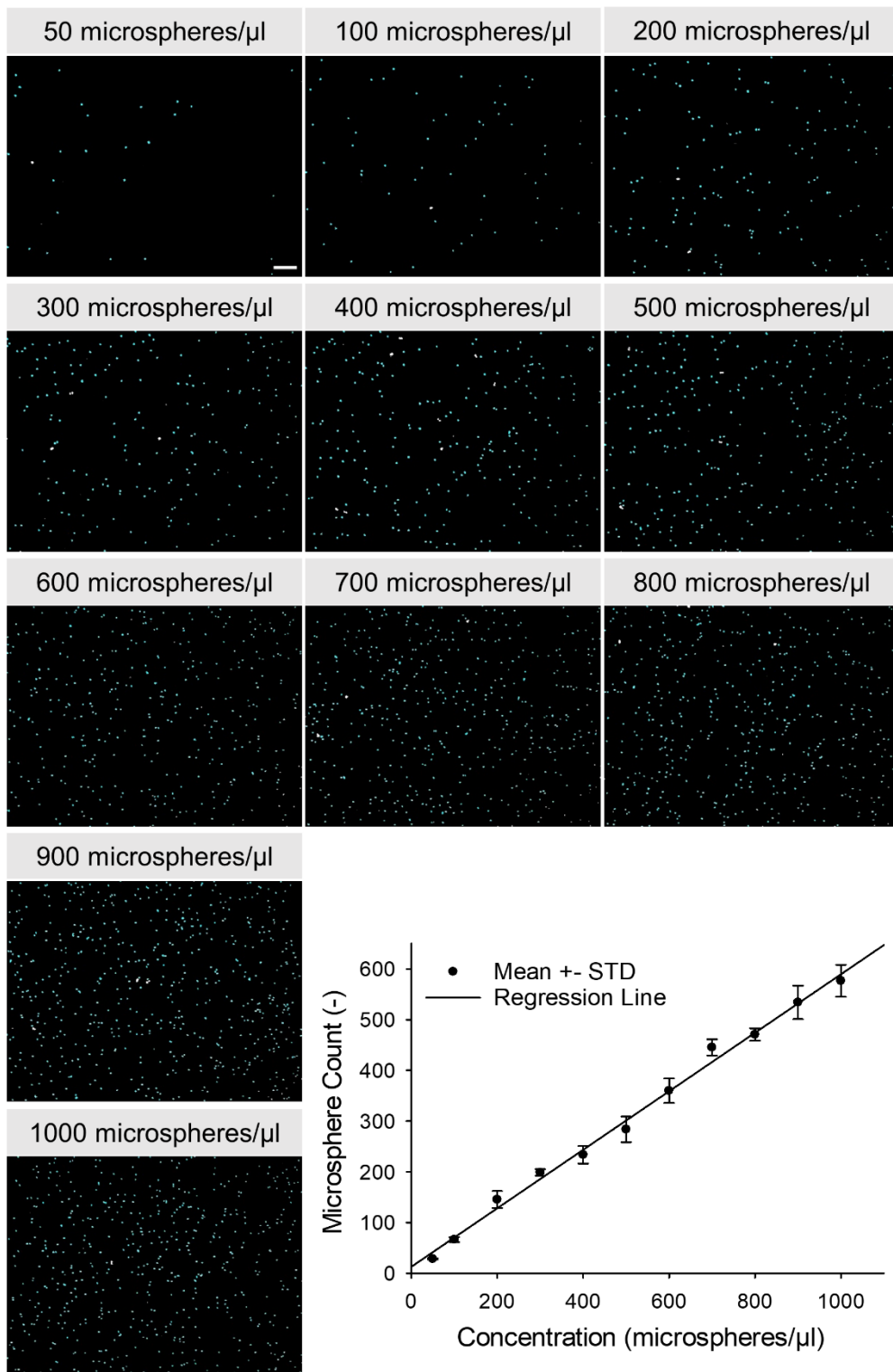


Figure 4.13 GFP microsphere calibration

The figure shows representative maximum intensity Z-projection images of recorded Z-stacks of green fluorescent microspheres embedded in GelMA in concentrations between 50 and 1,000 microspheres/ μ l (scale bar = 100 μ m). The graph shows the correlation of analysed microspheres per recorded image with the initial concentration of microspheres per μ l of hydrogel precursor solution. The linear regression line has an $R^2 = 0.986$ and its equation is $y = 0.5769 x + 12.823$ ($n = 3$).

The theoretically smallest possible step size of the X-axis is 5 µm, respectively 2.50 µm (Y-axis) and 3.75 µm (Z-coarse) in $\frac{1}{4}$ micro-stepping mode. However, to verify the smallest possible step size, which can be physically achieved, the spatial resolution was determined by measuring the distance between the start and endpoint of the travelled distance for a given step size (Figure 4.15 A). Step sizes between 1 µm and 62.50 µm were given, and the travelled distances of the X- and Y-axis were measured by taking images of a 1951 USAF test target. Additionally, images of the test target were taken without moving the stage in between to determine the systematic error of the imaging setup.

A minimum step size of 10 µm was determined for the X-axis, as smaller step sizes are within the standard deviation of the control (Figure 4.15 C). Increasing given step sizes correspond to the travelled step sizes very well, as shown by the linear regression with an r^2 of 0.984.

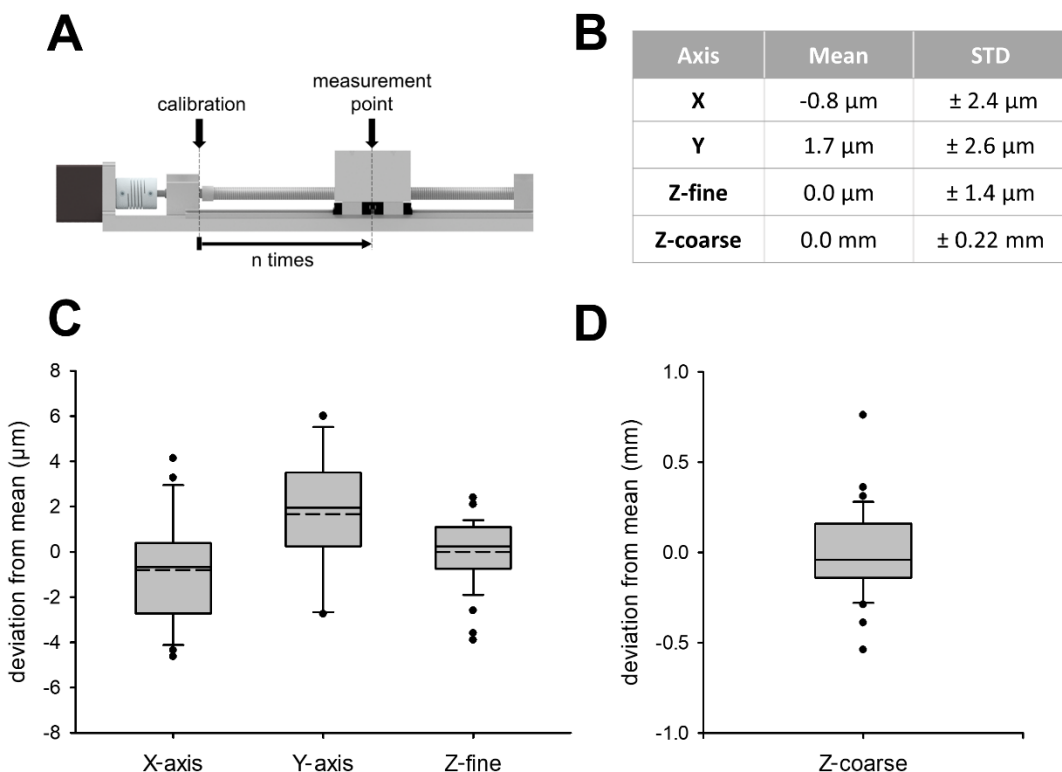


Figure 4.14 Repeatability and accuracy of the XYZz-stage

(A) Measurement method. (B) Repeatability (means) and accuracy (standard deviation) of X-, Y-, Z-fine and Z-coarse axis. (C) Boxplots of the repeatability of the X-, Y- and Z-fine axis. (D) Boxplots of the repeatability of the Z-coarse axis ($n = 20$).

For the Y-axis, a minimum step size of 5 µm and a linear regression between given and travelled step sizes with an r^2 of 0.999 was achieved (Figure 4.15 D).

The step size of the Z-fine axis was determined by placing the needle of the dial gauge onto the stage and measuring the displacement of the gauge while lowering and lifting the stage. Four different step sizes between 10 µm and 250 µm were determined, resulting in a good fit with an r^2 of 0.999 of the linear regression for step sizes between 10 and 50 µm (Figure 4.16 C). The step size of the Z-coarse axis was determined by measuring the distance between the carriage and the bearing with a calliper for each step taken by the stage. Three step sizes between 63 µm and 313 µm were given by the code. With a given step size of 63 µm, the stage travelled 40 µm \pm 21 µm on average. With a given step size of 125 µm, the stage travelled 90 µm \pm 26 µm, and with a given step size of 313 µm, the stage travelled 295 µm \pm 28 µm (Figure 6D).

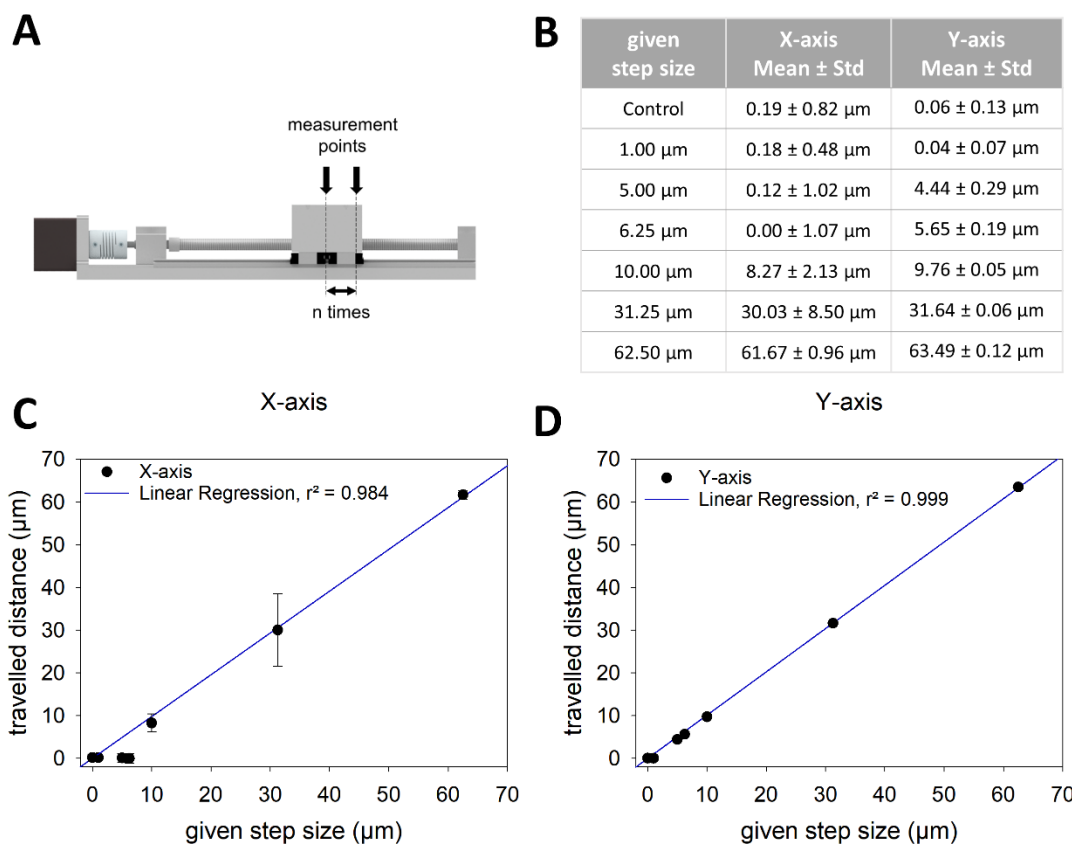


Figure 4.15 Spatial resolution of the X- and Y-axis

(A) Measurement method. (B) Mean and standard deviation of the X- and Y-axis for given step sizes. (C) Travelled distances in µm for given step sizes and linear regression of the X-axis. (D) Travelled distances in µm for given step sizes and linear regression of the Y-axis ($n = 20$).

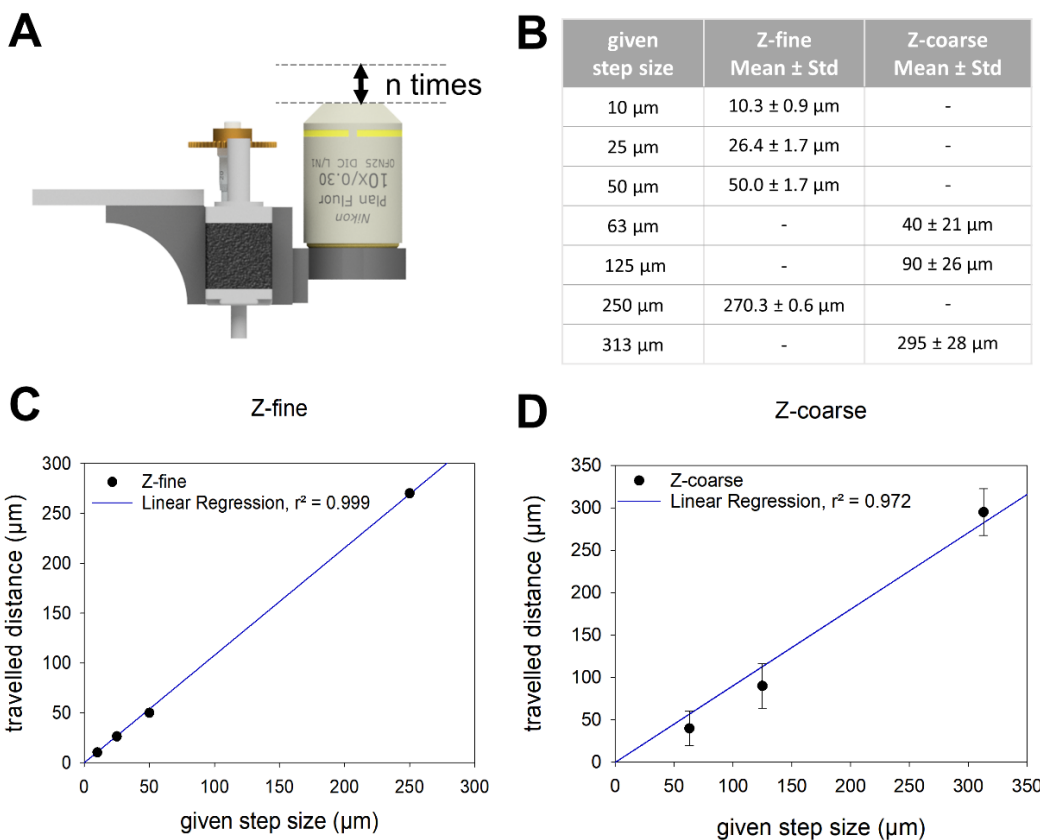


Figure 4.16 Spatial resolution of the Z-fine and Z-coarse axis

(A) Measurement procedure of Z-fine axis **(B)** Mean and standard deviation of given step sizes of Z-fine and Z-coarse axis **(C)** Travelled distances in μm for given step sizes and linear regression of the Z-fine axis **(D)** Travelled distances in μm for given step sizes and linear regression of the Z-coarse axis ($n = 20$).

4.2.4 Software and graphical user interface

A graphical user interface (GUI) was developed to control the system. The GUI was written in Python with Tkinter. There are two GUI's: one direct control of the OMSM, which is helpful for validation and testing. The other is a protocol generator app, where all settings are defined before running the whole protocol to image one or more microwell plates.

In the “Manual Settings and Control” GUI (Figure 4.17 A), camera settings can be adjusted, such as the ISO value and shutter speed. Saving options for the snapshots, each with the blue, mint or both LEDs on, and a pre-determined Z-Stack can be determined. A live image of the camera can be started and stopped.

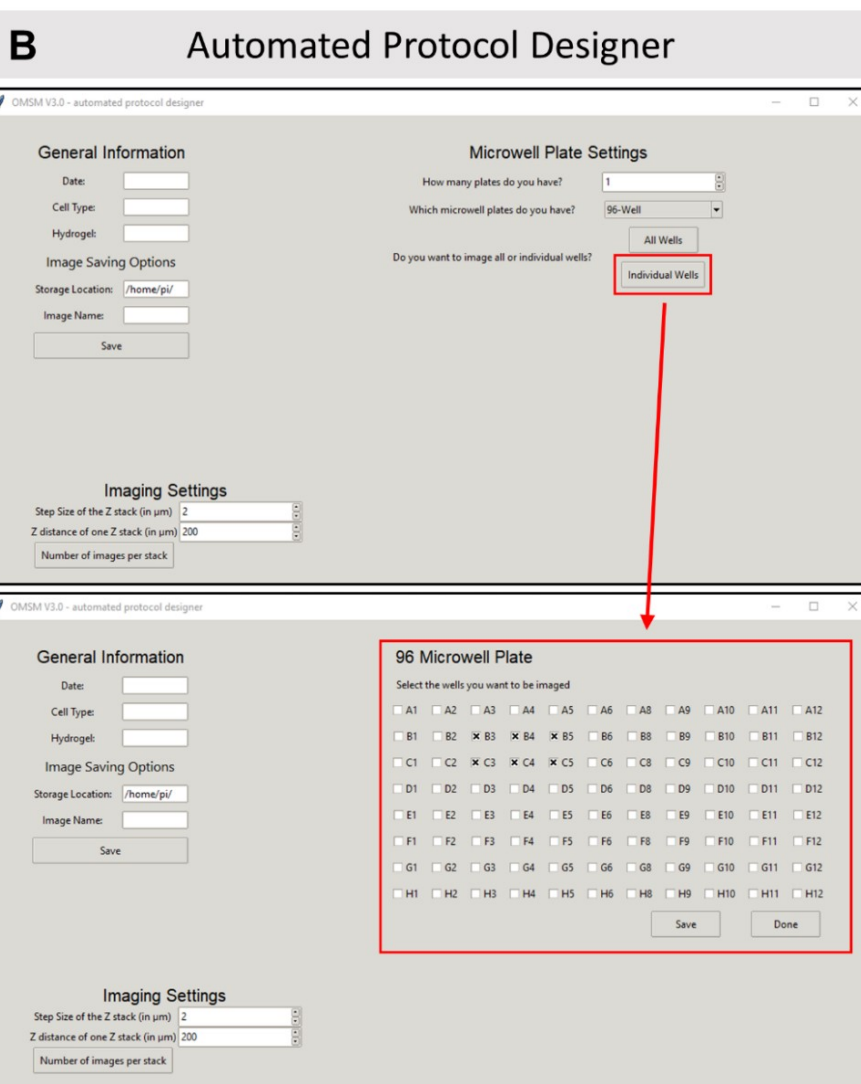
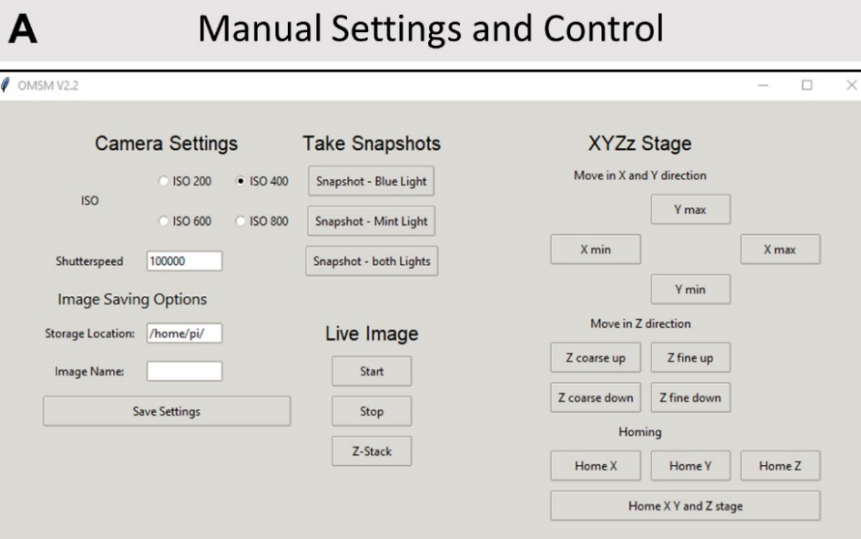


Figure 4.17 Graphical user interface

(A) Manual settings and control of the XYZZ-stage and the microscope. (B) “Automated Protocol Designer” with the possibility to select individual wells for imaging.

Moreover, the XYZZ-stage can be homed and moved, in pre-determined step sizes, in all directions. In the “Automated Protocol Designer” (Figure 4.17 B), general information about the experiments can be entered, which will be saved in a separate text file for the documentation of the experiment. The imaging settings for the Z-stacks, e.g. the step size and overall Z-distance, can be determined, and the number and type of microwell plate can be defined. Additionally, it is possible to either image a whole microwell plate or selected wells of a plate, if not all wells need to be imaged.

4.3 AIM 3: PROOF-OF-CONCEPT STUDY

The opto-mechatronic screening module was developed and built to automate the analysis of 3D tumour models. To prove the capabilities of the module, a live dead assay, alongside a comparison with conventional technology, described in section 4.3.1 and an endpoint drug screening assay, presented in section 4.3.2, were conducted on the opto-mechatronic screening module.

4.3.1 Live/dead cell viability assays

In order to demonstrate the microscope’s fluorescence capabilities of stained 3D cell cultures, PC-3 cells, embedded in GelMA-based hydrogels, were cultured for up to six days and imaged both with the OMSM and a commercial fluorescence microscope.

4.3.1.1 Time-dependent live/dead cell viability imaging

PC-3 cells embedded in 4% GelMA were stained with a live/dead assay kit and imaged on day one, six and eight after encapsulation (Figure 4.18). Live cells were stained with Calcein-AM, marked in green and dead cells were stained with EthD-III, shown in red.

The whole field of view of the microscope is shown in the first row of Figure 4.18 (A, B, C), overviewing the cell population in an area of approximately 1 by 1 mm. Here, both live and dead cells, as well as individual cells and cell clusters, are recognisable in the images. However, the spheroids did not increase substantially in size over a time period of six days. The second row of Figure 4.18 (D, E, F) shows magnified regions of interest of selected samples. Here, cells stained with EthD-II are better visible than in the original-sized images. Additionally, differences in fluorescence intensity of Calcein are recognisable in some cell clusters (Figure 4.18 D, F).

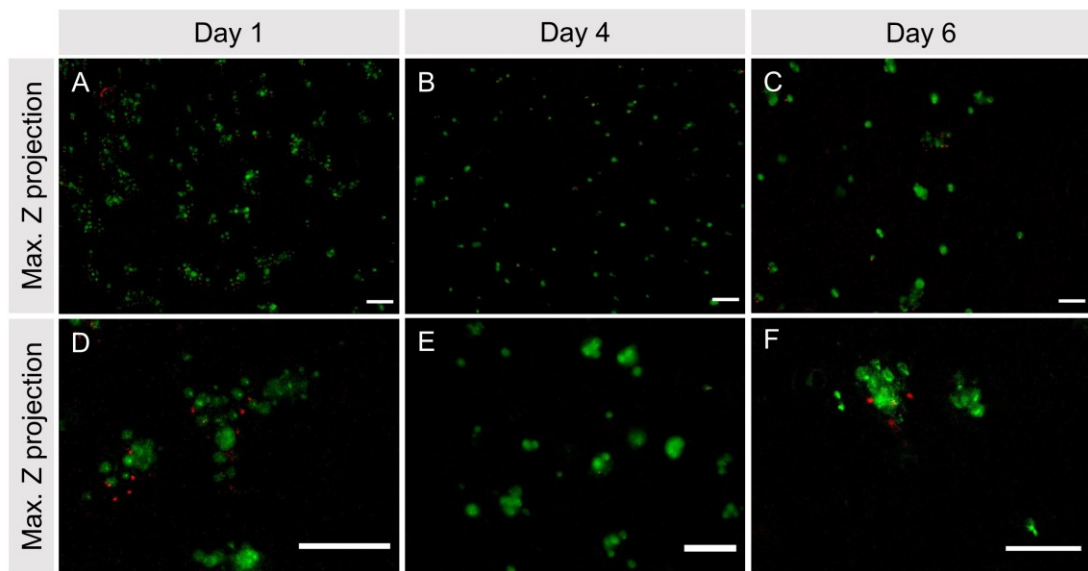


Figure 4.18 **Fluorescence images of the live/dead viability assay**

On day 1 (**A, D**), 4 (**B, E**) and 6 (**C, F**) of cultivation of PC-3 cells in 4% GelMA cells were stained with Calcein AM to stain live cells (green) and EthD-III to stain dead cells (red). The images in the upper row cover the whole field of view. In the second row are detailed views of selected samples. All images are maximum intensity Z-projections of Z-stacks covering a Z-distance of 500 µm (scale bar = 100 µm).

4.3.1.2 Comparison with conventional technology

Fluorescence images of live/dead staining of 2D cell layers and cells embedded in GelMA (3D) were taken with the opto-mechatronic screening module and a conventional fluorescence microscope to compare both technologies. Images on both systems were taken with a similar objective (Nikon 10x, 0.3 NA) from the same sample but not the same field of view. Hence, differences in the distribution of cells might appear. In both images of 2D monolayers, individual cells are recognisable (Figure 4.19 A, B) and the images look similar. The fluorescence signal of dead cells, stained with EthD-III, is weaker in the images taken with the OMSM than in the images taken with a conventional microscope, both in the 2D and 3D images (Figure 4.19 A, C). However, the fluorescence signal is still strong enough and sufficient for automated image analysis. To assess viability, the images captured using both microscopes were subjected to the same analysis method outlined in section 3.3.3. Analysis of the viability of images obtained from the OMSM and the conventional microscope respectively revealed similar rates: 94% for cells cultured in 2D for both microscopes and 87% and 90% for cells cultured in 3D (Table 4.2). Despite the calculated

comparable viability rates, it is worth noting that the standard deviation of viability, based on images taken with the OMSM, was slightly higher. This discrepancy may be attributed to the OMSM's smaller field of view in comparison to the conventional microscope

Table 4.2: Viability of PC-3 cells cultured in 2D and 3D calculated on the basis of image taken with OMSM and Nikon Eclipse Ti, respectively ($n = 6$)

	OMSM	Nikon Eclipse Ti
2D	94 % \pm 6 %	94 % \pm 3 %
3D	87 % \pm 9 %	90 % \pm 3 %

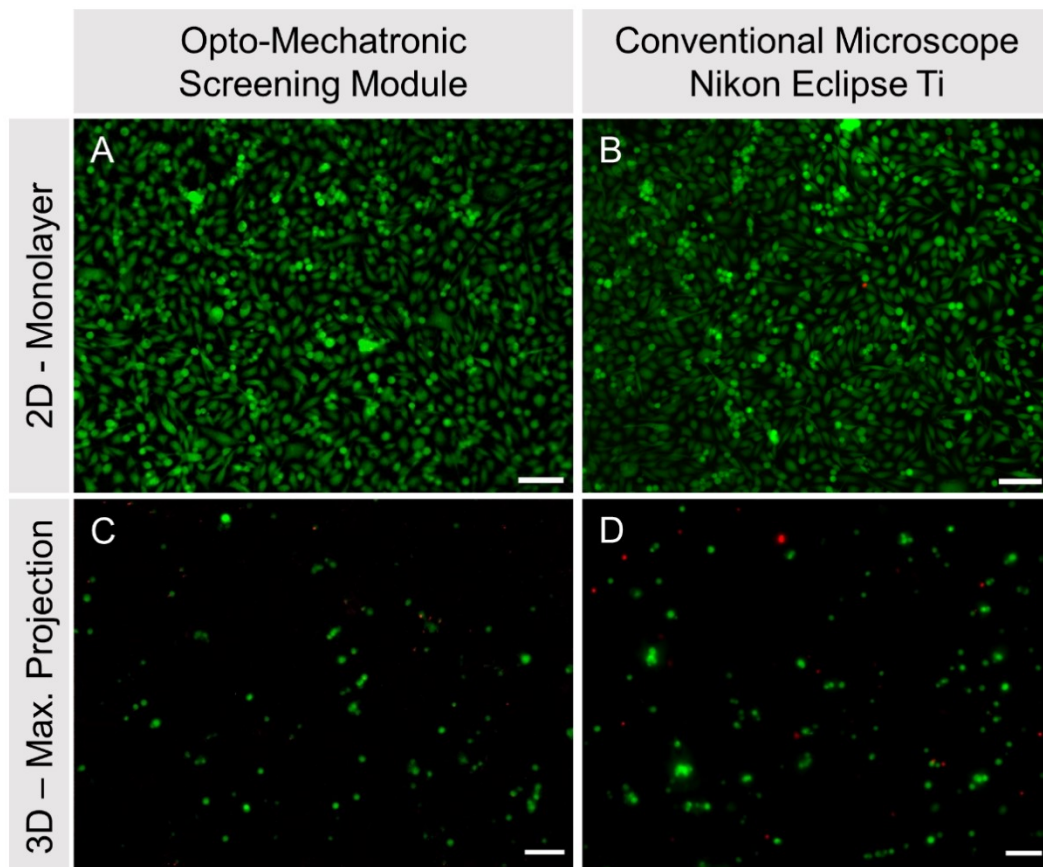


Figure 4.19 Comparison of opto-mechatronic screening module with a conventional fluorescence microscope

PC-3 cells were stained with a live/dead cell viability kit. **(A, B)** The first row shows PC-3 cells cultured as 2D monolayers without hydrogel. **(C, D)** In the second row are maximum intensity Z-projections of Z-stacks of PC-3 cells cultured in 4% (w/v) GelMA, imaged with a step size of 10 μm , covering a total Z-distance of 700 μm . Both images, each 2D and 3D, are taken from the same sample but not from the same region (scale bar = 100 μm).

4.3.2 Drug-response study

In order to demonstrate the capabilities of the OMSM to perform drug screenings, an endpoint and a time-dependent drug-response study were conducted. Additionally, the influence of docetaxel on PC-3 cells cultured in 2D and 3D was studied.

4.3.2.1 Endpoint drug-response study

PC-3 cells embedded in GelMA were grown for three days, treated with docetaxel and stained with Calcein-AM and EthD-III after three days of treatment to demonstrate the drug screening capability of the OMSM. PBS and DMSO were added as controls.

The samples ($n = 10$) were recorded as Z-stacks with a step size of 10 μm over a Z-distance of 600 μm per well. In subsequent image analysis, the Z-stacks were merged into maximum intensity Z-projections. Representative images of drug condition and control are presented in Figure 4.20. As described in 4.3.2.1, live cells stained with Calcein-AM are shown in green and dead cells stained with EthD-III are shown in red.

Live cells were clearly visible as individual cells and cell clusters, both in the controls and docetaxel treatments (Figure 4.20). Dead cells were not as clearly visible as live cells, but they were still recognisable and, more importantly, could be analysed with image processing software (Figure 4.21). The cells were distributed throughout the hydrogel; however, there were accumulations of cells within some areas rather than an even distribution throughout the whole hydrogel specimen.

The absolute cell numbers of each recorded Z-projection, both live and dead cells, within one treatment or control group, varied considerably (Figure 4.21 A), e.g. between six and 107 live cells within the samples treated with PBS (Mean absolute number of live cells for PBS: 33.8 ± 33.5 , DMSO: 23.4 ± 23.3 , 10 μM docetaxel: 28.5 ± 16.8 , 100 μM docetaxel: 13.4 ± 12.2 , 1,000 μM docetaxel 1.3 ± 1.9 ; mean absolute number of dead cells: PBS: 4.8 ± 7.7 , DMSO: 8.0 ± 17.2 , 10 μM docetaxel 6.8 ± 6.1 , 100 μM docetaxel 3.4 ± 5.7 , 1,000 μM docetaxel: 7.5 ± 8.9). Despite the substantial variation in absolute cell numbers, there were significant differences between the group treated with 1,000 μM docetaxel and the PBS control group ($p = 0.002$), the DMSO control group ($p = 0.009$) and the group treated with 10 μM docetaxel ($p <$

0.001). However, there were also significant differences between any other groups of live and dead cells for the absolute cell number.

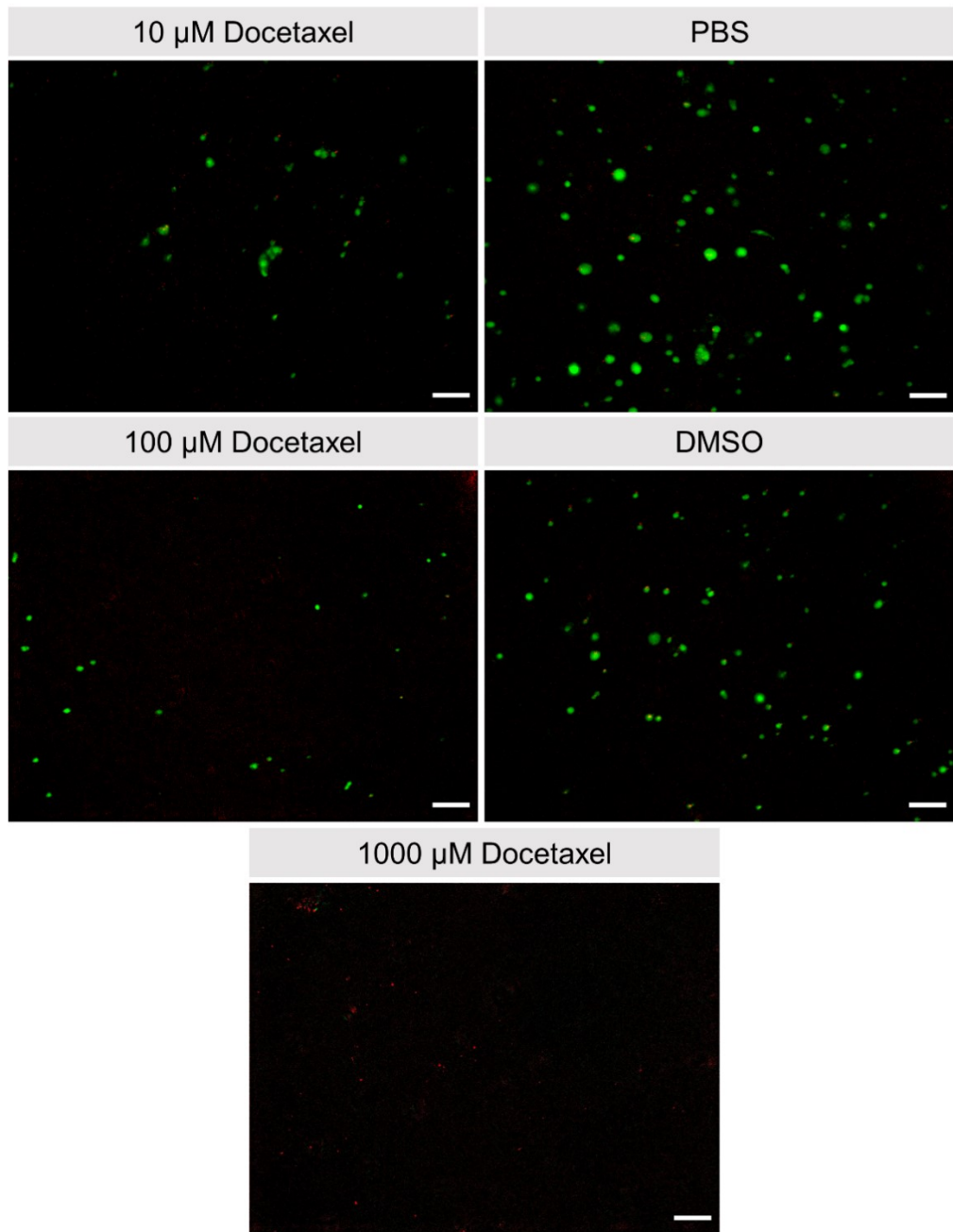


Figure 4.20 Endpoint (3 days) drug-response study of PC-3 cells treated with docetaxel

Representative images of max. Z-projections of each drug concentration respectively control. Green: Calcein AM, red: EthD-III (scale bar = 100 μm).

Due to the variation in absolute cell numbers, the relation between live and dead cells for each sample was calculated as the relative cell/spheroid number (Figure 4.21 B). The mean relative cell number and standard deviation for each group was calculated (relative cell number of live cells: PBS: $77.1 \pm 30.3\%$, DMSO: $83.2 \pm$

17.6%, 10 μ M docetaxel: 80.3 \pm 16.1%, 100 μ M docetaxel 70.9 \pm 35.5%, 1,000 μ M docetaxel: 10.6 \pm 18.8%; relative cell number of dead cells: PBS: 12.9 \pm 14.3%, DMSO 16.8 \pm 17.6%, 10 μ M docetaxel: 19.7 \pm 16.1%, 100 μ M docetaxel 29.1 \pm 35.5%, 1,000 μ M docetaxel: 69.4 \pm 40.7%). There were significant differences between the group treated with 1,000 μ M with each of the other groups, both for live and dead cells.

The average size of each cell or cell cluster was determined as well (Figure 4.21 C), which is more interesting for the live cells since Calcein distributes in the cell plasma and not so informative for dead cells, since EthD-III only binds to nucleic acids and does not stain the whole cell. The average particle size of live cells in the group treated with PBS was 423 \pm 261 μm^2 , DMSO: 245 \pm 193 μm^2 , 10 μ M docetaxel: 335 \pm 180 μm^2 , 100 μ M docetaxel 229 \pm 162 μm^2 , 1,000 μ M docetaxel: 18 \pm 3 μm^2 and the average size of dead cells in the group treated with PBS was: 27 \pm 21 μm^2 , DMSO: 29 \pm 20, 10 μ M docetaxel 25 \pm 21 μm^2 , 100 μ M docetaxel 26 \pm 13 μm^2 , 1,000 μ M docetaxel 17 \pm 5 μm^2 . There were significant differences between the group treated with 1,000 μ M docetaxel and PBS ($p = 0.003$) and between those treated with 1,000 μ M and 10 μ M docetaxel ($p = 0.007$).

Lastly, the total area of the fluorescence signal of both live and dead cells was determined (Figure 4.21 D). The mean total area of live cells of the group treated with PBS was 14,331 \pm 20,980 μm^2 , DMSO: 5,178 \pm 9,262 μm^2 , 10 μ M docetaxel 7,859 \pm 3,360 μm^2 , 100 μ M docetaxel: 3114 \pm 4,595 μm^2 , 1,000 μ M docetaxel 22 \pm 31 μm^2 and of dead cells of the group treated with PBS: 125 \pm 235, DMSO: 257 \pm 654 μm^2 , 10 μ M docetaxel 239 \pm 386 μm^2 , 100 μ M docetaxel: 89 \pm 171 μm^2 , 1,000 μ M docetaxel 133 \pm 169 μm . There were significant differences in the total area of live cells between the group treated with 1,000 μ M docetaxel and the PBS-group ($p < 0.001$), the DMSO group ($p = 0.035$) and the group treated with 10 μ M docetaxel ($p < 0.001$).

4.3.2.2 Time-dependent drug-response study

PC-3 cells were grown as 2D and 3D cell cultures, exposed to docetaxel (0.01, 0.1, 1, 10, 100 and 1,000 μ M) for three, six, nine and fourteen days and analysed with a live/dead staining kit on the OMSM.

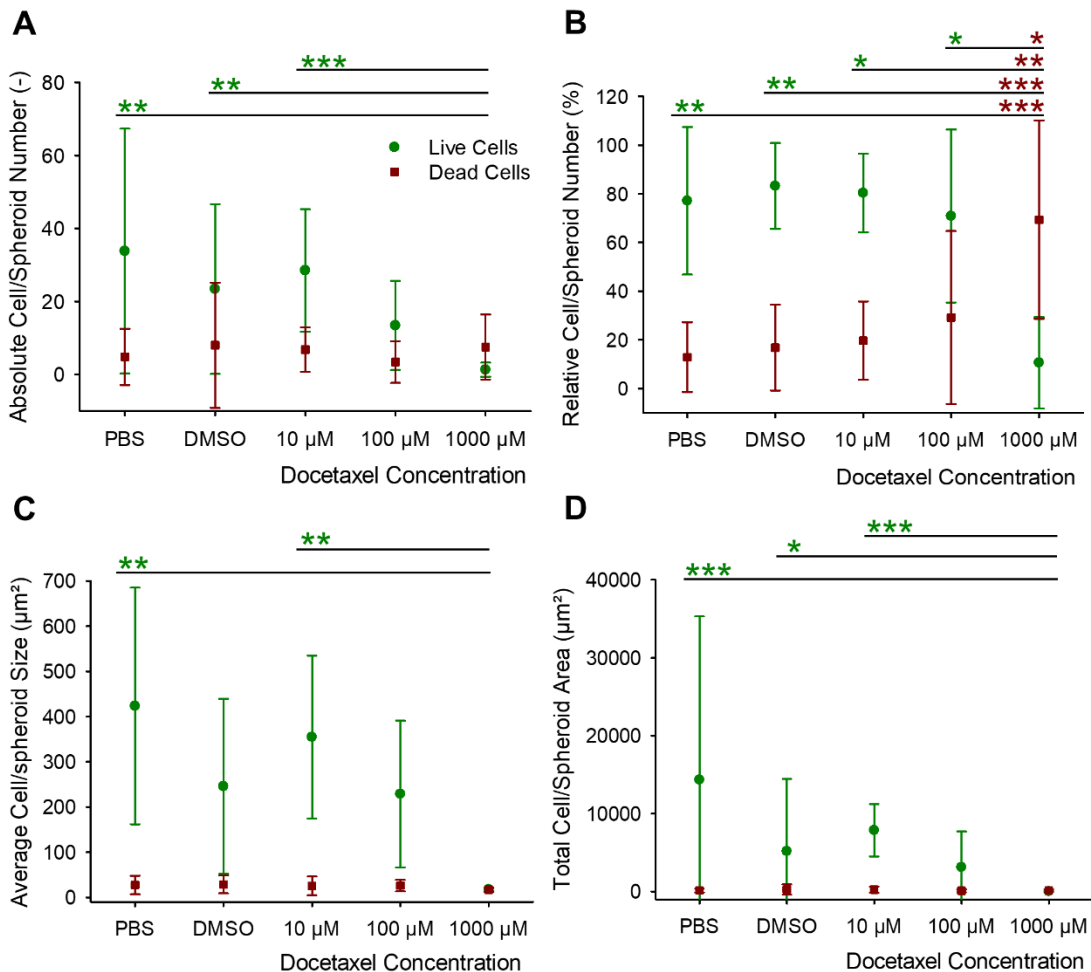


Figure 4.21 Analysis of endpoint drug-response study

(A) Average total cell number of each control and treatment group. (B) Average relative cell number (%) of each control and treatment group. (C) Average total area (μm^2) summed up of all cells and spheroids within the image for each control and treatment group. (D) Average cell size (in μm^2) of each control and treatment group. Significant differences (* $p < 0.05$, ** $p < 0.01$, *** $p < 0.001$, ANOVA) are marked on the left side in green for live cells and in red on the right side of each bar, non-significant results are not marked for better clarity.

Determination of cell number and size are based on image segmentation analysis as described in 3.3.3 ($n = 10$).

Figure 4.22: Representative images of the time-dependent drug-response study of PC-3 cells cultured in 2D

Representative images of each drug concentration, respectively control. Green: live cells stained with Calcein AM, red: dead cells stained with EthD-III (scale bar = 100 μm).

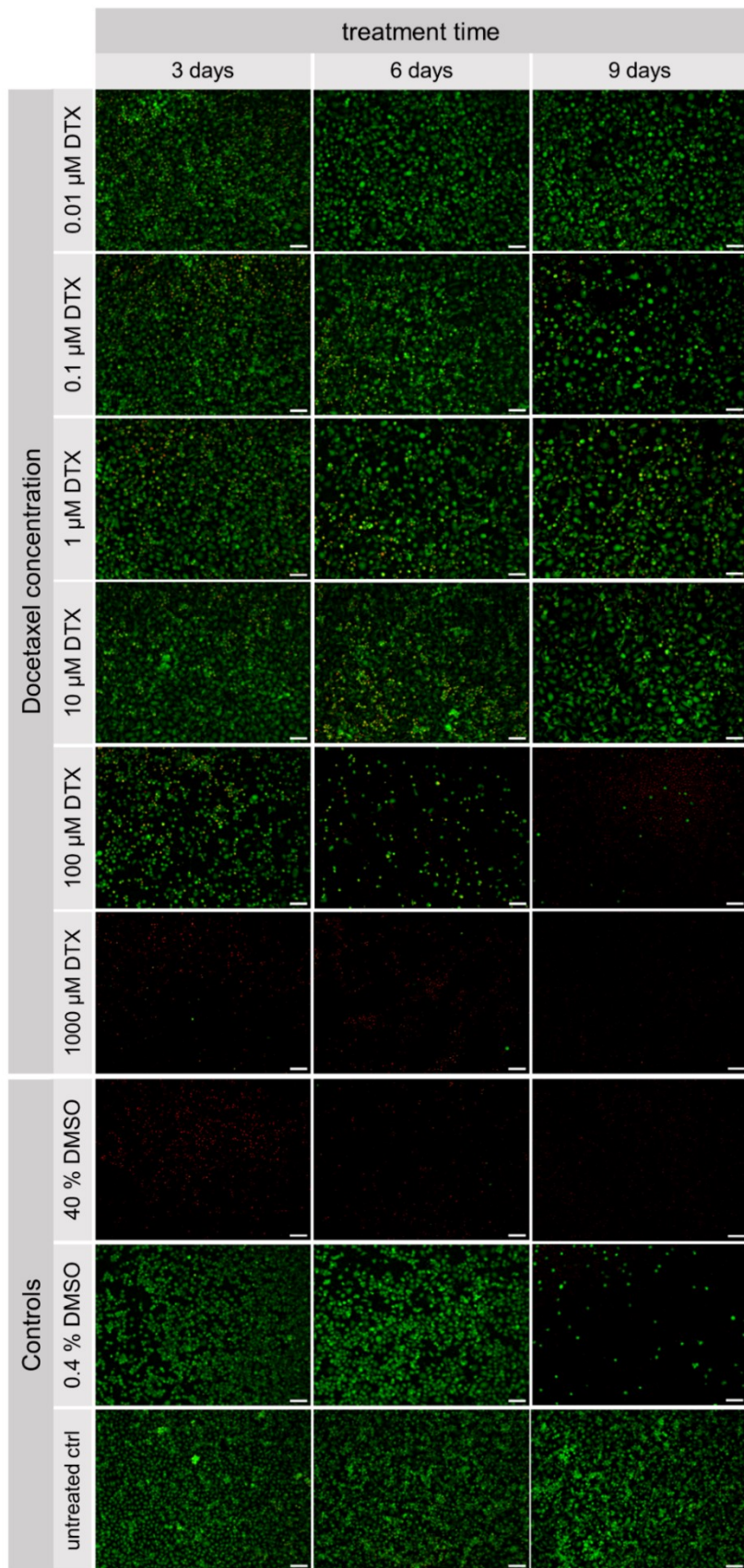


Figure 4.22: Representative images of the time-dependent drug-response study of PC-3 cells cultured in 2D

Qualitative analysis of 2D cell culture

For the 2D cell culture, representative images of each drug condition are shown in Figure 4.22. After three days of drug treatment, the bottom of the wells exposed to $0.01\text{ }\mu\text{M} - 10\text{ }\mu\text{M}$ docetaxel was covered with live cells, with a few dead cells in between, similar to the untreated control and the negative control (0.4% DMSO). In the sample treated with $100\text{ }\mu\text{M}$ docetaxel, fewer live cells were in the recorded area than in the samples exposed to lower drug concentrations. Almost only dead cells were visible in the samples treated with $1,000\text{ }\mu\text{M}$ docetaxel. Only dead cells were visible in the positive control (40% DMSO). The samples treated with docetaxel for six days look similar to those treated for three days. However, the number of live cells in the specimen exposed to $100\text{ }\mu\text{M}$ docetaxel decreased noticeable, which further continued with a drug treatment time of nine days. In general, after nine days of drug treatment, the overall number of live cells seemed to decrease. It is particularly striking that in the negative control (0.4% DMSO), the number of live cells decreased substantially.

Qualitative analysis of 3D cell culture

Representative images of maximum Z-projections of recorded Z-stacks of 3D cell cultures are displayed in Figure 4.23. In general, the cells were mostly distributed isolated and in smaller spheroids throughout the hydrogel.

For three days of drug treatment, there was no noticeable difference in the number of live cells for samples exposed to $0.01\text{ }\mu\text{M} - 10\text{ }\mu\text{M}$ docetaxel, but there was a slight decrease for $100\text{ }\mu\text{M}$ and $1,000\text{ }\mu\text{M}$ docetaxel. The number of dead cells increased with increasing docetaxel concentration up to a concentration of $100\text{ }\mu\text{M}$, and then it decreased slightly. In the samples treated for six, nine and fourteen days, the number of live cells remains relatively constant up to a drug concentration of $10\text{ }\mu\text{M}$, and then, the number decreased. However, for a drug treatment time of fourteen days, the overall number of live cells was lower than for shorter drug treatment times.

Figure 4.23: Representative images of the time-dependent drug-response study of PC-3 cells cultured in 3D

Representative images of max. Z-projections of each drug concentration, respectively control of PC-3 cells cultured in LunaGel. Green: live cells stained with Calcein AM, red: dead cells stained with EthD-III (scale bar = $100\text{ }\mu\text{m}$).

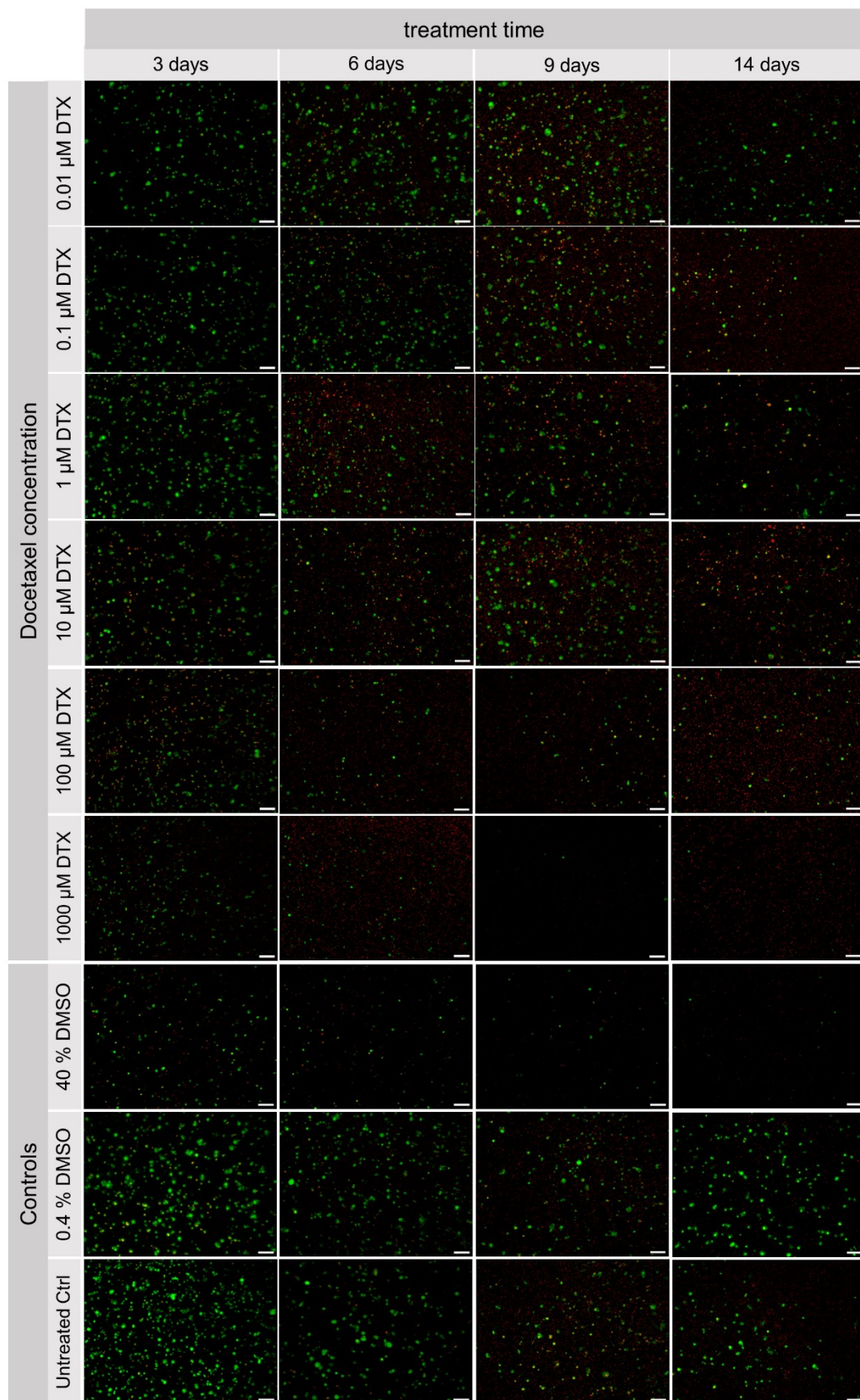


Figure 4.23: Representative images of the time-dependent drug-response study of PC-3 cells cultured in 3D

The number of live cells in the positive control decreased with treatment time, while the number of dead ones did not change noticeably. The number of live cells in the negative and untreated control also decreased with time.

Quantitative viability analysis of 2D cell culture

In the 2D cell culture, the viability of PC-3 cells exposed to 0.01 μM – 10 μM docetaxel for three and six days was about 80%, while the viability in the samples exposed to docetaxel for six days was slightly lower with a viability of 70% (Figure 4.24 A). With a concentration of 1,000 μM docetaxel, the viability converged to zero for three and nine days; and to around 20% for six days of drug treatment. The null hypothesis was rejected for each treatment time; hence, there were significantly differences ($p < 0.001$) between the treatment groups within one treatment time. Looking at the absolute cell numbers (Figure 4.24 B), the cell numbers decreased with increasing drug treatment time for each drug condition, and the null hypothesis was rejected for each treatment time ($p < 0.001$). Looking at the negative controls, the cell number of the negative control (0.4% DMSO) also substantially decreased with increasing treatment time. Based on the viability, an IC₅₀ of 181 μM was calculated for a drug treatment time of three days, an IC₅₀ of 40 μM for six and an IC₅₀ of 100 μM for nine days of drug treatment (Table 4.2), respectively. However, the data for the drug treatment times of six and nine days did not pass the normality test. An IC₅₀ of 204 μM docetaxel was calculated for a drug treatment time of three days, based on the number of live cells per mm². Nonlinear regression failed for six and nine days of drug treatment.

Quantitative viability analysis of 3D cell culture

The viability of PC-3 cells cultured in 3D was between 50 and 75% for the lowest drug concentration and converged to around 57% for three days of drug treatment, to 45% for six and nine days, and to zero for fourteen days of drug treatment (Figure 4.24 C). The null hypothesis was rejected for a treatment time of fourteen days ($p < 0.05$) but not for three, six and nine days. The live cell number per mm² decreased with the drug treatment time after nine days of drug exposure, similar to the 2D cell culture (Figure 4.24 D). Similarly, also the cell number within the negative controls, both the untreated control and the one treated with 0.4% DMSO, decreased with increasing treatment and culture time, respectively (Figure 4.24 H).

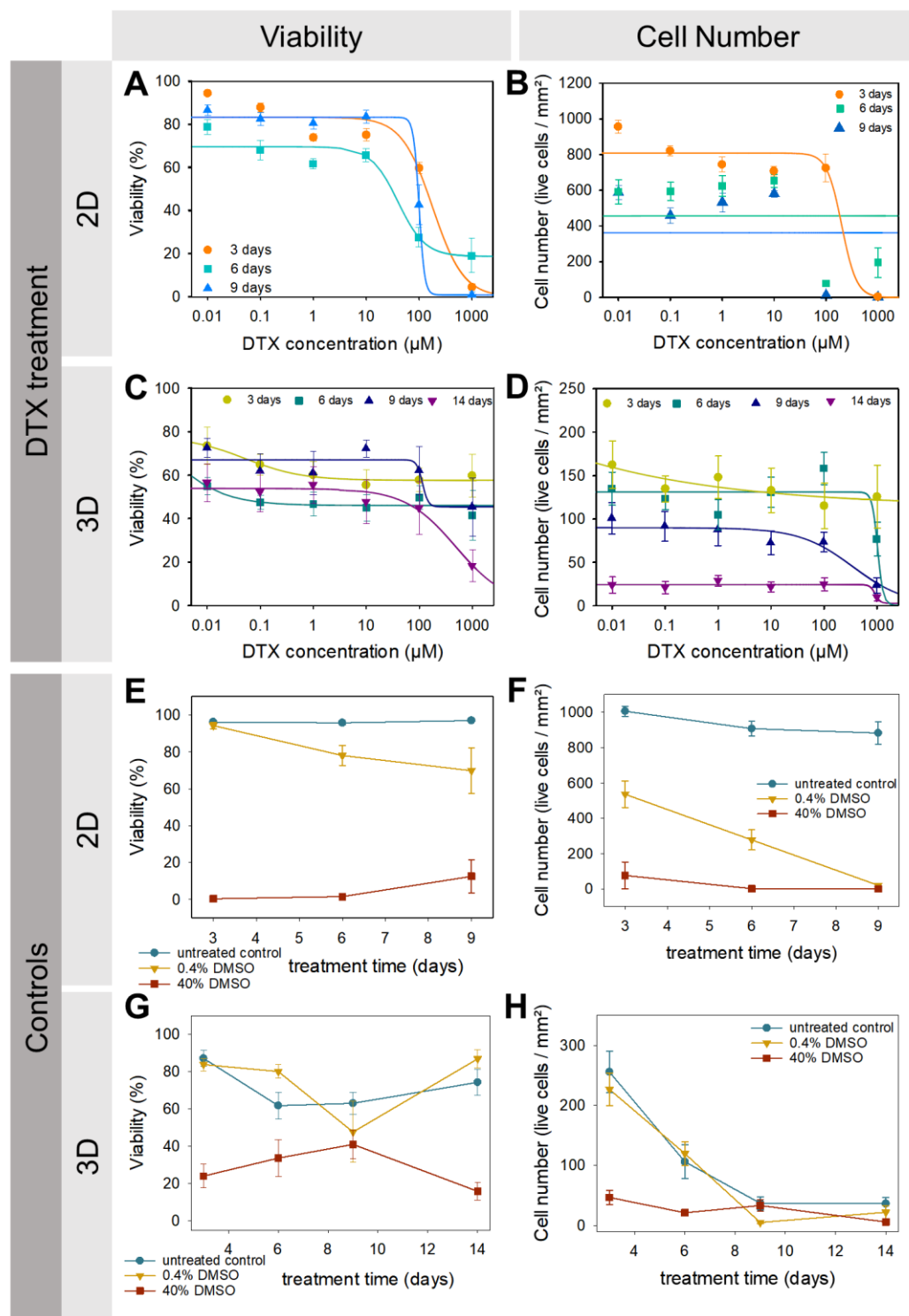


Figure 4.24: Viability and cell number of the time-dependent drug-response study

Nonlinear regression based on a four-parameter logistic curve for each drug treatment time (orange: three days, turquoise: six days, blue: nine days, violet: fourteen days) for (A) the viability of 2D cell cultures, (B) the cell number/ mm^2 of 2D cell cultures, (C) the viability data of 3D cell cultures, and (D) the cell number/ mm^2 of 3D cell cultures. The viability and cell number of the controls with an untreated sample (blue), 0.4% DMSO (yellow) and 40% DMSO (red) for (E) the viability of 2D cell cultures, (F) the cell number/ mm^2 for 2D cell culture, (G) the viability of 3D cell cultures, and (H) the cell number/ mm^2 for 3D cell culture (mean \pm standard error are given for each dataset; $n = 12$).

Based on the number of live cells per mm², the null hypothesis was rejected for the treatment groups of six ($p < 0.05$) and nine days ($p < 0.01$), but there were no statistically significant differences between drug treatment for three and fourteen days of drug treatment.

For the calculation of the IC₅₀ value, drug treatment times of three, six and nine days, the normality test failed. An IC₅₀ of almost 500 µM was determined for a drug treatment time of fourteen days based on the viability (Table 4.2). An IC₅₀ of 360 µM was determined for a drug treatment time of nine days based on the number of live cells per mm². The data of the other drug treatment times failed the normality test.

Table 4.3: IC₅₀ values for docetaxel and results of the null hypothesis test for 2D and 3D cultured PC-3 cells

(P = p value for statistically significant difference among the treatment groups (one-way ANOVA), * $p < 0.05$, ** $p < 0.01$, *** $p < 0.001$, - not statistically significant difference)

Calculation based on	2D cell culture				3D cell culture			
	viability		cell number per mm ²		viability		cell number per mm ²	
Treatment time (days)	IC ₅₀ (µM)	P	IC ₅₀ (µM)	P	IC ₅₀ (µM)	P	IC ₅₀ (µM)	P
3	180.86	***	203.75	***	0.05	-	< 0.01	-
6	40.28	***	< 0.01	***	< 0.01	-	1042.12	*
9	100.34	***	< 0.01	***	116.43	-	360.22	**
14	-	-	-	-	499.34	*	929.29	-

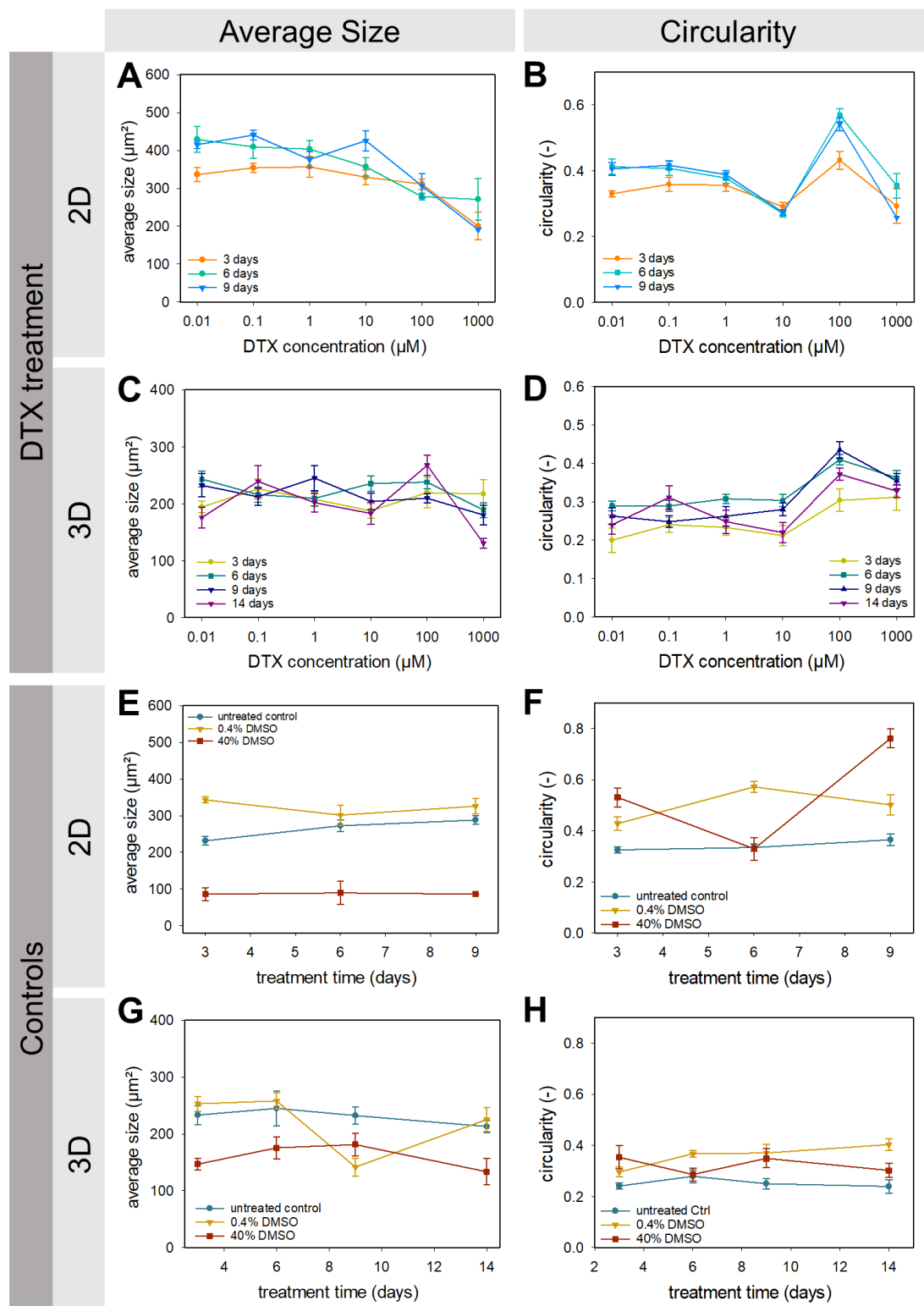


Figure 4.25: Analysis of morphology

Analysis of morphology

The morphology of the cells is described by determining the average size and the circularity of each cell or spheroid (Figure 4.25). The average size of the samples cultured in 2D decreased slightly with a docetaxel concentration higher than 100 μM (Figure 4.25 A). In comparison, the circularity reached a maximum at a docetaxel concentration of 100 μM (Figure 4.25 B).

There were no differences in the average cell or spheroid size for cells cultured in 3D between drug treatment time or drug concentration (Figure 4.25 C). At the same time, there was a slight increase in the circularity with a docetaxel concentration of 100 μM or higher (Figure 4.25 D). The average size across all samples of 2D cell cultures was $335 \mu\text{m}^2 \pm 100 \mu\text{m}^2$, and for 3D cell cultures, the average size was lower with $220 \mu\text{m}^2 \pm 61 \mu\text{m}^2$. In 2D, the average size (Figure 4.25 E) and the circularity (Figure 4.25 F) of the controls remained relatively constant over time, except for the circularity of the positive control, which increased after nine days of treatment. In 3D, the average size of the cells in the positive control was lower than the average size of the cells in the untreated control (Figure 4.25 G). At the same time, there are fewer differences in the circularity between the control groups (Figure 4.25 H).

Figure 4.25: Analysis of morphology

- (A) Average size (mean \pm standard error) of cells treated with docetaxel for three (orange), six (turquoise) and nine (blue) days cultured in 2D and (B) their corresponding circularity. (C) The average size of cells exposed to docetaxel for three (orange), six (turquoise), nine (blue) and fourteen (violet) days cultured in 3D and (D) their corresponding circularity. (E) Average size and (F) circularity over time of the controls (blue: untreated control, yellow: negative control with 0.4% DMSO, red: positive control with 40% DMSO) groups cultured in 2D. (G) Average size and (H) circularity of the control groups cultured in 3D (mean \pm standard errors are given for each dataset; n = 12).

Chapter 5: Discussion

This chapter discusses the results presented in Chapter 4 and evaluates the outcomes in the context of the requirements and the literature outlined in Chapter 2. Section 5.1 discusses the results obtained in the validation of the biomanufacturing workstation. Section 5.2 discusses the OMSM and its validation and compares the results with current open-source and low-cost microscopy systems. Section 5.3 evaluates the findings of the proof-of-concept studies.

5.1 AIM 1: VALIDATION OF THE BIOMANUFACTURING WORKSTATION

The here validated biomanufacturing platform overcomes the drawbacks of commercial systems for handling viscous solutions in a high-throughput manner. Contrary to commercial hardware, which can either handle viscous solutions, e.g. bioprinters, or which have a higher degree of automation and throughput capabilities, e.g. liquid handling robots, the here facilitated biomanufacturing platform combines the features of both, including additional features necessary for handling viscous and photo-crosslinkable materials such as temperature docks and LED panels for photo-crosslinking.

5.1.1 Automated and reproducible workflow

In order to establish an automated and reproducible workflow for the production of hydrogel-based 3D tumour models, it is necessary to investigate the parameters influencing the outcome of the workflow.

Since the stiffness of the surrounding microenvironment of cells influences their physiological behaviour, the compressive modulus is a crucial parameter for designing a hydrogel-based tissue culture platform. However, various parameters influence the compressive modulus, such as polymer concentration and crosslinking parameters. Hence, it is essential to identify them and their range of influence in order to establish an automated and reproducible workflow for hydrogel production with defined stiffness.

The whole workflow of the biomanufacturing workstation for 3D tumour models is based on 96-microwell plates. Thus, their influence on the compressive modulus

was investigated. Three commonly used flat-bottom microwell plates were included in this study: Transparent microwell plates, which are often used for drug screenings and cell-based assays in microscopic and optic measurements; white microwell plates with a maximum reflectivity and minimal autoluminescence, used for luminescence measurements and black microwell plates, with a clear bottom, which are optimised for fluorescence measurements due to a minimum of back-scattered light and background fluorescence. The type of microwell plate had no significant influence on the compressive modulus.

Several studies [57], [58] already reported that the crosslinking parameters also influence the compressive modulus of a hydrogel. Hence, the influence of the photo-initiator concentration and exposure time was also studied here. It was shown that the compressive modulus increases with increasing photo-initiator concentration. However, higher concentrations of photo-initiator might be toxic for cells, in particular the presence of unreacted radicals affects cell viability [57], [65]. Therefore, it is not advisable to increase the compressive modulus of a hydrogel by increasing the photo-initiator concentration. In addition, the influence of exposure time on the compressive modulus was studied. Here, three different exposure times, two, four and eight minutes, were used to crosslink the samples. Under the given circumstances (polymer concentration, polymer volume, photo-initiator), there was no significant difference in the compressive modulus between samples crosslinked for two, four or eight minutes, indicating that full crosslinking of the samples for this specific conditions was achieved after two minutes. Indeed, my findings contradict studies such as the one conducted by Schuurman et al, which reported a dependence between crosslinking time and hydrogel stiffness [58]. However, it is important to note that their findings were not solely based on crosslinking time, but rather on the combination of time and light intensity during crosslinking. High light intensity reduces the required time for crosslinking until reaching a saturation point based on the amount of polymer present in the sample. Additionally, Fairbanks et al demonstrated that the initiation of polymerization with LAP occurs earlier compared to the use of Irgacure 2959, which was utilized in the study by Schuurman et al [58], [65]. This highlights the influence of the photo-initiator and the wavelength used in the crosslinking process. These factors contribute to the differences observed between my study and previous research, emphasizing the complexity of hydrogel crosslinking dynamics.

Optimised mixing step

The preparation of hydrogel precursor solution includes a series of steps; one of them is mixing the required substances, such as the stock solution of hydrogel prepolymers, the diluent, and the photo-initiator, to a homogenous solution. A common issue here is mixing the viscous hydrogel stock solution with a non-viscous diluent. As this is already challenging for manual handling, the mixing is not trivial for automated handling. Hence, the mixing behaviour for GelMA-based hydrogels was investigated and optimised to ensure reproducible production of GelMA precursor solution.

The diluent was stained with Orange G to verify the workflow, enabling spectrophotometric absorbance measurements of the samples, which were taken from different immersion depths (2 mm) throughout the prepared precursor solution. 10% (w/v) GelMA was facilitated for the mixing optimisation procedure.

Before the mixing has been optimised, the mixing was performed with a single aspiration and dispersion step at a fixed position, repeated four times (referred to as “without optimised mixing”). This procedure resulted in insufficient mixing since more diluent remained in the upper part of the reaction tube and more GelMA was in the lower part of the reaction tube, filled with the solution. This insufficient mixing led to high coefficients of variation (CV) ranging from 10.6 to 63.1%. Thus, more aspiration and dispersion steps were added to the mixing procedure in an iterative process. Additionally, a specific movement of the pipette was added to the repertoire: inverse pipetting. Here, the pipette moves down with the falling liquid level while aspirating and moves up while dispensing liquid from the tip. In addition to the inverse pipetting, the overall aspiration and dispersion speed was increased so that the final CV was decreased to between 1.4 and 2.7%. All in all, the optimised mixing procedure resulted in a better mixture of GelMA and its diluent, which significantly improved the reproducibility, and outperformed manual pipetting, which suffers under intra- and inter-individual imprecision as demonstrated in a previous study [117]. Manual pipetting is influenced by uneven rhythm, incorrect tip immersion depth and deviation from the verticality [118], [119]. These factors are diminished by automated liquid handling.

In addition, it was shown that the optimised mixing protocol is not only applicable for one kind of GelMA concentration but also for lower (5% (w/v)) and

higher (15% (w/v)) polymer concentrations. In an experiment with four independent replicates, the CV ranged between 1.8 and 5.3%, highlighting a highly reproducible mixing procedure for a range of GelMA concentrations.

5.1.2 Parameter library

The characterisation of the mechanical properties of hydrogels is commonly done on a trial and error basis using one-factor-at-a-time (OFAT) experiments. However, this approach is time- and labour-consuming and neglects the interactions and dependencies between various material and process parameters.

Instead, a DoE approach identifies the dependencies between various input factors and their effects on output factors and provides a more detailed understanding of the influence of each parameter [120], [121]. For example, Moshayedi et al. used a surface response methodology to optimise growth factor and adhesion protein concentrations in an HA-based hydrogel for human neural stem cell proliferation and differentiation. The authors demonstrated that DoE enables systematic alterations of various hydrogel components to determine outcome characteristics for further *in vivo* testing [122], [123]. Although statistical DoE approaches have been already employed for the multifactorial analysis of hydrogel-based systems, demonstrating the benefits, their throughput has been low, and they lack automation technology [122], [124], [125].

Therefore, we used the DoE to systematically and efficiently investigate the material factors and establish a parameter library for GelMA-based hydrogels in an automated manner using the *Biomanufacturing Workstation*. Beforehand, three key parameters regulating the stiffness of a hydrogel were identified: the polymer concentration (in (w/v)) and two crosslinking parameters, which are the light exposure duration (in seconds) and the light intensity (mW/cm^2). As a measure of stiffness, the compressive modulus (in kPa) was defined as an output parameter.

This systematic study revealed that the GelMA concentration strongly influences the compressive modulus. The exposure time duration has minor effects, and the light intensity does not influence the compressive modulus of the hydrogel. Additionally, the interaction of the GelMA concentration with the exposure time duration also influences the compressive modulus. In line with these results, previous studies reported a strong power-law dependence of the GelMA precursor concentration on the

compressive modulus. Contrary to the here presented results, the authors also showed that the variation of the modulus with the crosslinking time appeared to follow first-order kinetics [58]. However, the authors used a UV-light based crosslinking system in combination with the photo-initiator Irgacure 2959, which is different from the here used crosslinking system using light with a wavelength of 400 nm and the photo-initiator LAP, emphasizing the importance of studying the influence of each parameter in a multifactorial system.

The statistical analysis of the model used to study these parameters resulted in an accurate fit with an R^2 value of 0.917 and a good prediction precision. The software calculated a good model validity of 0.827, indicating that there were no diverse models problems, such as the presence of outliers, an incorrect model or transformation problems. In addition, the model shows a high reproducibility of 0.907, where the variation of the replicates was compared to the overall variability.

Overall, the presented DoE approach is a user-friendly and straightforward methodology for systematically studying the combinatorial effects of the material and crosslinking parameters of hydrogels. Additionally, DoE can be used to establish a parameter library for a given hydrogel system, accelerating the production of mechanically defined hydrogel without tedious preliminary experiments.

5.1.3 Automated analysis of unconfined compression test data using *MechAnalyze*

The need for automated and reproducible analysis arises with the capability of automated production of hydrogels with various mechanical properties. So far, the here presented mechanical data of hydrogels underwent unconfined compression testing with subsequent automated analysis to determine each sample's compressive modulus and failure properties. However, manual assessment of compression test data is tedious, not standardised and suffers from user-to-user bias. Hence, we developed an algorithm, *MechAnalyze*, for the automated and user-independent determination of compressive moduli, failure stress and failure strain from load-extension raw data of unconfined compression tests [108].

MechAnalyze reduced the analysis time 96-fold (711×5 min per sample) to around 36 min (711×3 s + 60 s initial set up) and showed excellent agreement between manual and automated analysis of compression test data. A large inhomogeneous dataset of hydrogels, engineered and native tissues, provided by five independent

researchers, was the basis for validating the algorithm. The results of the analysis of this dataset were compared and correlated with the manual analysis of the same data. However, the user bias limits the value of using manually analysed data as a benchmark for validating automated analysis. As a perfect control does not exist, a large variety of datasets were sampled to minimise the influence of the user-to-user variability.

The analysis and comparison of the datasets also revealed a more considerable user-to-user variability, particularly for the sample height, and a bias of low correlation between manual and automated analysis towards individual researchers (Figure 4.9). The sample height is a crucial parameter for determining the compressive modulus due to the non-linear stress-strain behaviour of hydrogels and tissues. The height directly influences the strain region used to calculate the compressive modulus because it defines the point of 0% strain [126]. In the here presented manual analyses, the sample height has been determined visually from the force-displacement data as the point where the curve substantially starts deviating from the baseline. In other studies, callipers [60], [113] or optical measurements were used, or the depth of the casting mould [30], [127] used to prepare the sample was assumed as the sample height. Using callipers to determine the sample might be applicable for high modulus materials, but soft biomaterials deform on contact, and hence, it is difficult to reliably determine the contact point of the material and the calliper itself. While optical measurement methods to determine the sample height are contactless and precise, they are also time-consuming and tedious, as each sample must be imaged individually in a calibrated setting. The easiest way to determine the sample height might be to assume the depth of the casting mould as the sample height. However, this is only advisable for materials that are not expected to swell, but hydrogels and other water-containing biomaterials can swell substantially after preparation and thus, the sample height cannot be reliably assumed from the casting mould geometry [112], [128].

MechAnalyze determines the sample height from the extension-load curve of the measurement data [56]. Thus, no additional measurements, such as callipers or optical methods, are necessary, minimising hands-on time and increasing reproducibility by using a standardised method. However, the force signal-to-noise ratio must be sufficiently large to determine the sample height and ensure accurate automated analysis precisely. Thus, choosing a load cell with the lowest capacity suitable to

assess the expected mechanical sample parameters is recommended because noise usually scales with total force capacity.

In the analysis of user-to-user variability, interestingly, users, who produced a low coefficient of determination for one parameter, scored, on the other hand, relatively high in other parameters, indicating that the determination of specific parameters is highly subjective. For example, users 2 and 3 had a low coefficient of determination for the sample height but a high coefficient for compressive moduli. Considering the other assessed mechanical parameters, a bias of low correlation between manual and automated analysis towards individual researchers is revealed by both dataset-specific R^2 values and errors. For example, dataset 4 has an R^2 value of 0.5774 for the determination of failure strain. Additionally, 15 out of 18 outliers were associated with this dataset, emphasising the user-dependent variability in the manual analysis of compression test data. For this reason, it is crucial to diminish the user-dependent variability in the manual analysis of compression data between individual researchers by an automated and standardised method.

Indeed, some attempts were already made to automate the analysis of mechanical testing data, but the developed algorithms are limited to tensile [129] or indentation tests [130] and are not suitable for unconfined compression test data, although compression tests are the most common and straightforward mechanical test in tissue engineering [131]. For example, hydrogels tend to tear easily because they are soft and brittle at the same time [128], [132]; hence, sample preparation for tensile testing is difficult and time-consuming [133], [134]. In addition, in tensile testing, the samples are limited to specific geometries [135], while unconfined compression tests facilitate the use of more possible geometries such as cylinders [32], [136] or cubes [137], [138]. However, since the sample geometry itself can influence the measurement of the compressive modulus, the sample geometry and height needs to be accounted into the strain rate dependency by choosing 10% of the initial sample height per minute to increase the comparability of the results between different studies [139].

MechAnalyze calculates the compressive modulus and failure properties using the load and extension data, including the sample geometry as the surface area and height. The comparison of manually and automatically generated data demonstrates that *MechAnalyze* can calculate reliably mechanical parameters from datasets originating from different experimental settings and users. *MechAnalyze* was applied

for a broad range of biomaterials, including hydrogels, engineered tissues and ex vivo human cartilage samples covering compressive moduli from less than 1 kPa to almost 4,000 kPa.

However, for the determination of failure properties, comparatively lower R^2 values across all sample types were found, which might be caused by the subjectivity of the manual analysis but also by the intrinsic differences in failure mechanism between covalently and ionically crosslinked hydrogels. Covalently crosslinked hydrogels, such as GelMA, are intrinsically brittle and usually fracture into two or more parts prior plastic deformation [140], [141]. Hence, the failure can be easily identified in the corresponding stress-strain curve, both manually and automatically, as a sudden drop. In contrast, ionically crosslinked hydrogels, such as alginate, exhibit intermediate behaviour and yield when the elastic deformation limit is reached [142]. This failure mode is more difficult to identify, both by users and the algorithm of *MechAnalyze*, because it is characterised by a relative decrease in the slope of the stress-strain curve rather than a sudden drop of the absolute stress. Typically, *MechAnalyze* identifies the failure of yielding materials as the first local maximum. However, in some cases, the decrease in the slope of the stress-strain curve in the yielding point is too small to be recognised by the software. Therefore, visual quality control of the markers of each mechanical parameter in the software-generated graphs ensures correct data analysis.

5.2 AIM 2: INTEGRATION OF AN IMAGING MODULE

5.2.1 The opto-mechatronic screening module and its integration into the workstation

The OMSM was designed in line with the assembly-line approach of the biomanufacturing workstation developed by Eggert et al. [16]. Hence, it can be easily connected to the workstation enabling automated imaging of up to eight tissue culture plates without the need for manual intervention. Due to the connection of the biomanufacturing station, the samples can be transported from the storage rack to the pipetting module, e.g. for cell culture media change, the addition of drugs or staining procedures, and back to the imaging module. This system enables even multitasking by using the pipetting module and the OMSM simultaneously due to the module's independence, though still being connected.

The XYZz-stage combines a robotic gripper arm and a motorised XY scanning stage for microscopes. This combination diminishes the need to move the tissue culture plates from one system to another, thus minimising the sample's movement, vibrations, and disruption. Additionally, it saves material and space by minimising the overall footprint and eliminates the need to orchestrate two different systems, thus simplifying the module's control. However, due to the combination of the two systems, the X-stage has a greater travel range than a conventional XY scanning stage for microscopy. In addition, as a rule of thumb, the longer a linear actuator is, the less precise is the positioning. However, the validation of the X-stage revealed an accuracy of 0.8 µm and repeatability of 2.4 µm, which is still sufficient for imaging cells and spheroids.

The OMSM was designed for imaging 96-microwell plates. Nevertheless, it also enables imaging for a wide range of tissue culture plates and dishes. The gripper of the XYZz-stage is suitable for standardised well plates, such as 6-, 24-, 96- and 256-microwell plates, with the outer dimension of 85.6 x 127.8 mm, according to AMS/SLAS standards. In addition, microscopy slides and petri dishes can be placed onto the gripper with the help of conventional petri dishes or slide holders, which are quickly 3D printed or bought at any microscope supply shop.

The microscope is optimised for digital fluorescence imaging. Therefore, an eyepiece was waived to save costs and keep the overall footprint as small as possible. The illumination and filter setup is optimised for imaging of fluorophores in the green and red spectra. Here, the use of GFP, Calcein AM and EthD-III have been shown, but also any other fluorophore that matches the excitation and emission spectra can be used with the same setup. For example, cell tracker assays, used for cell movement and location studies, with the dyes Green CMFDA and Orange CMRA or CellTracker CM/Dil (ThermoFisher Scientific), and cell cycle assays, such as Premo FUCCI Cell Cycle Sensor (ThermoFisher Scientific), are suitable as well. Additionally, all studies involving the expression of GFP or red fluorescent protein (RFP) and assays using the fluorescent dye tetramethylrhodamine (TRITC), which is commonly conjugated to antibodies and proteins, can be used with the here presented LED and filter setup.

The filter setup comprises a multi-band dichroic mirror and multi-band emission filter and, thus, allows automated switching between fluorescence channels, while in other open-source microscopes, the filter cubes have to be swapped manually [101],

[143]. In combination with a colour camera, these multi-band filters enable even simultaneous imaging of multiple fluorophores. Nuñez et al. used this approach to image up to three fluorophores, excited by one single blue LED [144]. However, thereby the system is limited to very few specific fluorophores and subsequent colour channel separation is necessary to distinguish between multiple fluorescent proteins. In addition, the probability of crosstalk and background noise increases due to multiple transmission bands of the filters. In order to minimise crosstalk, LEDs with narrow emission bands are used so that only one fluorophore at one time is excited. This method also enables super-fast switching between two “fluorescence channels” within milliseconds without the need to mechanically switch filters. Thereby, additional mechanical movements, and thus vibrations and disruptions, and possible error sources are reduced to a minimum [145].

In addition to the installed filter sets and LEDs, other filter settings are also conceivable by exchanging the filters sets and using LEDs with other wavelength spectra. Thereby, any desired fluorophores can be imaged with the OMSM.

The entire system costs around 5,325€, from which the microscope costs 3,508€, the XYZ-stage 1,475€ and other components such as electronics and frame cost 340€ (Appendix B). Compared to other open-source microscopes and XYZ-stage systems, the price is in the middle range. There are more inexpensive systems such as the fluorescence microscope presented by Maia Chagas et al. with around 200€ [100], the “UC2” by Diederich et al. with costs between 100 and 600€ [101] and the Incubot which costs approximately 1,000€ [99]. However, these low-cost systems are based on 3D-printed components, which are not very durable and do not include an XYZ-stage or any other kind of automation. On the contrary, the Flexiscope costs around 16,000€ [143] and, hence, is around four-fold more expensive than the OMSM. Although the Flexiscope is a highly flexible microscope capable of oblique infrared illumination imaging, 3D-scanning, and multi-channel fluorescent imaging, automated features, such as switching between fluorescent channels and scanning whole microwell plates, are missing.

One unique feature of the OMSM is the integrability into a biomanufacturing workstation, including a liquid handling robot for viscous and non-viscous materials. On the contrary, the open-source and low-cost microscopes, which have been

developed so far, are standalone systems without the feasibility of being easily connectable to liquid handling robots.

However, Ouyang et al. presented a modular framework for automated pipetting and imaging applications based on the open-source pipetting robot Opentrons OT2 and a standalone microscope, called “OpenmiTronScope”, for transmission brightfield and a modified version of the UC2 microscope for fluorescence imaging [101], [146]. The authors integrated either one of the microscopes, each equipped with an XY stage, onto the working deck of the OT2, enabling simultaneous pipetting and imaging of tissue culture plates and providing a space-saving solution. Nevertheless, the system is limited to automated imaging of only one microwell plate with one fluorescence channel, and it does not fulfil the requirements for hydrogel-based 3D cell cultures such as viscous material handling and photo-crosslinking capability.

5.2.2 Validation of the microscope

The imaging resolution of the microscope was determined using a 1951 USAF test target. All line pairs of the test target, up to 228 line pairs per millimetre, were resolvable with high contrast. A pixel size of 0.6 by 0.6 μm was determined, indicating that the optics rather than the camera sensor limit the resolution of the system. By resolving Group 7/Element 6 of the 1951 USAF test target, the microscope yields a resolution $d_{\min} < 2.19 \mu\text{m}$, indicating that the microscope can resolve subcellular features [101].

The resolution of the OMSM is similar to other open-source imaging systems, i.e. the resolution of the Incubot [99] and Flexiscope [143] for all subregions is at least 228 lp/mm as well. However, a direct comparison with other systems is not reasonable due to the inherent dependency of the resolution on the employed optical components, i.e. objective, which is mainly chosen, depending on the intended purpose. For example, Diederich et al. determined three different practical resolutions depending on the employed camera. They measured for their UC2 fluorescence microscope, equipped with a 100x objective with an NA of 1.25 and with a Raspberry Pi V2 camera a resolution of $d_{\text{Rasp}} = 1.13 \mu\text{m}$, a better resolution was measured with a cell phone camera of $d_{\text{cellphone}} = 0.6 \mu\text{m}$, which already clearly resolved the plasma membrane of bacteria. For comparison, a cutting-edge research-grade microscope (Zeiss Axiovert TV, Germany) achieved a resolution of $d_{\text{Zeiss}} = 0.27 \mu\text{m}$ [101]. Hence, the resolution can be increased by exchanging individual components of the microscope, such as the

objective or camera. Nevertheless, it remains always a cost-benefit consideration if the achieved resolution is sufficient for the desired application.

The X-Z view of round microspheres revealed an asymmetric PSF, indicating spherical aberration of the optical system [147]. However, the axial resolution is still sufficient for the intended purpose of imaging whole cells and spheroids to analyse cell populations. Several studies demonstrated the use of widefield fluorescence microscopes for the determination of cell viability of 3D spheroids [14], [148], [149]. For detailed in-depths 3D views of spheroids, cell agglomerates and 3D structures, dedicated equipment, such as confocal or multiphoton microscopes, would be more suitable.

In order to demonstrate the fluorescence and Z-stacking capability of OMSM, green fluorescent microspheres embedded in GelMA were imaged and analysed. The initial concentration of microspheres in the hydrogel precursor solution and the number of counted particles correlated very well with an R^2 of 0.986, demonstrating the use of representative Z-stacks for cell analysis. Additionally, it could be shown that the illumination of the microscope is sufficient to illuminate the whole sample and excite fluorescent microspheres throughout the whole sample. However, airy patterns are visible without background correction due to the three-dimensional nature of the point-spread function [150].

All in all, the microscope's resolution might be insufficient for observing sub-cellular features; however, it was developed to overview the viability and growth of a cell population in a microwell. The ability to image on cell level offers a valuable tool for initial fast screening purposes, such as evaluating the overall toxicity of different drugs or cell migration assays. This level of imaging allows for the assessment of cellular responses in a relatively quick and cost-effective manner. For this purpose, the resolution is sufficient. In order to achieve higher resolutions and to provide additional detailed information about intracellular processes and structures, objectives with greater magnification and higher numerical apertures or more advanced imaging systems with subcellular resolution capabilities would be necessary.

5.2.3 Validation of the XYZz-stage

The accuracy, repeatability and minimum step size of the XYZz stage were determined using a USAF 1951 test target for X- and Y-stage, a calliper gauge for the Z-coarse stage and a dial gauge for the Z-fine stage.

The X-axis has an accuracy of $-0.8 \mu\text{m}$, a repeatability of $2.4 \mu\text{m}$ and a minimum step size of $10 \mu\text{m}$. The Y-axis has an accuracy of $1.7 \mu\text{m}$ and a similar repeatability of $2.6 \mu\text{m}$ but a smaller step size of $5 \mu\text{m}$. Compared to the repeatability between 0.2 and $2 \mu\text{m}$ of commercially available microscope stages [102], the repeatability of the X- and Y-axis is quite good, considering a ten times lower price and up to two times greater travel range. In particular, the repeatability is substantially higher than in other open-source microscopy stages; i.e. Wijnen et al. reported repeatability of $156 \mu\text{m}$ and an accuracy of less than $30 \mu\text{m}$ for their 2D microscope stage [102]. The minimum step sizes of the Incubot, which was developed to scan a whole tissue culture plate as well, are 0.1 mm , and hence much higher than the OMSM. They reported a variation of $<5\%$ from the requested motion [99], which is still $500 \mu\text{m}$ for a requested motion of 10 mm and hence, substantially higher than the OMSM's repeatability. The Y-axis achieved a similar accuracy and repeatability as the Y-axis of the XYZ-positioning system, developed by Campbell et al., with a mean deviation of $2.1 \pm 1.4 \mu\text{m}$ while having a similar travel range of 150 mm [105]. However, their X-axis, which is 430 mm long, with a mean deviation of $61.0 \pm 47.3 \mu\text{m}$, was not as good as the accuracy and repeatability of the X-axis of the OMSM module. Additionally, Campbell et al. did not overcome the minimum step size of $100 \mu\text{m}$ pre-determined by the firmware Marlin, which they used as well. The positioning stage for automated high-content screening microscopy, developed by Schneidereit et al., has roughly half of the spatial resolution of X- and Y-axis with $5.1 \pm 1.8 \mu\text{m}$, respectively $3.5 \pm 2.2 \mu\text{m}$, but their average repeatability is three-fold higher with $3.9 \mu\text{m}$ for the X-axis and $5.4 \mu\text{m}$ for the Y-axis [104].

The Z-fine axis has the highest accuracy with $< 0.1 \mu\text{m}$ because the accuracy was limited by the smallest resolvable step and the lowest repeatability of $1.4 \mu\text{m}$. It has a travel range of 4 mm and a minimum step size of $10 \mu\text{m}$ or smaller since it was impossible to measure smaller values with the dial gauge. Courtney et al. implemented a Z-stage based on a stepper motor into their open-source microscope as well [143]. First, the authors used a piezoelectric system, but the repeatability and speed were too

low. Hence, they replaced it with a stepper system, which improved these parameters. However, their system has a minimum step size of $2.5\text{ }\mu\text{m}$, and the travel range of 13 mm is higher than the travel range of the Z-fine axis, but their system is also around four-fold more expensive (1,666€ compared to 377€) than the Z-fine axis.

For the Z-coarse axis, an accuracy of < 0.01 mm, and a repeatability of 0.22 mm was determined. However, the determination of the accuracy and repeatability was limited by the measurement method using callipers and the smallest resolvable step of the stage. However, the measured accuracy and repeatability are sufficient to transport well plates from the storage rack to the microscope. For finer steps and focus, the Z-fine axis has much better accuracy and repeatability, covering a travel range of 5 mm.

5.2.4 Operation of the OMSM

The aim of the development of OMSM was to control the module within one code or software and allow easy integration into the biomanufacturing workstation. Hence, the control unit of the OMSM is based on a Raspberry Pi 3 Model B computer, just as the biomanufacturing workstation. The controller board of the XYZz-stage, based on an Arduino Mega/RAMPS 1.6+ board, is connected via USB to the RaspberryPi. The electrical components of the microscope, the camera and the LEDs are connected directly to the Raspberry Pi. Therefore, the OMSM can be operated as a standalone module or integrated into the biomanufacturing workstation because all electrical components (the XYZz-stage controller board, camera and LEDs) could also be connected to the Raspberry Pi of the workstation's control unit [16]. Thereby, one script could control all modules of the workstation.

So far, the OMSM has been operated as a standalone module. For this purpose, two GUI's have been developed. One GUI can be used to directly control the OMSM, with a live view of the camera and direct control of each stage. The other GUI is an "Automated Protocol Designer" for generating a script that images up to six tissue cultures plates stored in the storage rack. The generated images are saved as .bmp files on the Raspberry Pi computer, from where they can be transferred via USB to a personal windows- or mac-based computer for further image processing.

5.3 AIM 3: PROOF-OF-CONCEPT STUDY

This chapter discusses the results of the proof-of-concept studies conducted on the OMSM, demonstrating the capabilities of the module to perform cell assays and analyses of 3D cell culture models.

5.3.1 Time-dependent live/dead cell viability assay

Live/dead cell viability assays were performed on PC-3 cells cultured for one, six and eight days in 4% (w/v) GelMA. The maximum intensity Z-projections clearly show cells stained with Calcein and EthD-III. Calcein is distributed throughout the cell, and, hence, individual cells and cell aggregates are visible. EthD-II is a nucleic acid; therefore, only the nucleus of the cells is stained, and, hence, the visible part of the cell is substantially smaller than live cells stained with Calcein. Nevertheless, the red fluorescent dye can be excited by the light of the mint LED, and the camera sensor can record the emitted light of the dye. Both fluorescence dyes were recorded automatically without manually or mechanically switching of filters in between.

To compare the imaging capabilities of the OMSM with a commercial scientific-grade microscope, fluorescence images of PC-3 cells, cultured in 2D and 3D and stained with a live/dead cell viability kit, were taken with the OMSM and with a Nikon Eclipse Ti fluorescence microscope with a similar objective (Nikon Plan Fluor 10x/0.3 NA). The images of both systems look similar, both 2D and 3D projection images, and all relevant information can be obtained from the images of the OMSM and the commercial microscope. Both systems have a similar pixel size, the OMSM has a pixel size of 0.63 µm/pixel, and the Nikon microscope has a pixel size of 0.65 µm/pixel for a resolution of 2,560 by 2,160 pixel. The field of view of the Nikon system is with 2.36 mm², two times greater than the field of view of OMSM with 1.18 mm². However, using a mosaic and tile stitching imaging mode expands the recorded region of the specimen.

5.3.2 Endpoint and time-dependent drug-response studies

An endpoint and a time-dependent drug-response study, using PC-3 cells cultured in GelMA or LunaGel, respectively, and treated with docetaxel, were conducted on the OMSM to demonstrate the capability of the module to perform drug screening assays on 2D and 3D cell culture models. Docetaxel is a common chemotherapeutic that is not only used to treat advanced prostate cancer but also breast,

head, non-small-cell lung cancer and bone cancer metastases [151]. The drug inhibits cell proliferation by preventing mitotic spindle assembly and cell division.

For the endpoint drug response study, PC-3 cells were cultured in 4% GelMA-based hydrogels with a compressive modulus of approx. 4 - 5 kPa, and treated with three different docetaxel concentrations (10 µM, 100 µM, 1,000 µM); after three days of treatment, the cell viability was assessed using a live/dead staining kit to demonstrate the drug screening capability of the OMSM.

The endpoint drug-response study resulted in significant differences between the group treated with 1,000 µM docetaxel and lower-dosed treatment groups and the control, indicating that the highest concentration of docetaxel is toxic to PC-3 cells embedded in 4% (w/v) GelMA. There were no significant differences in the cell viability between the groups treated with 10 µM and 100 µM docetaxel and the control groups. Hence, DMSO can be used in low concentrations as a drug solvent without influencing the viability in the here presented drug assay.

For the time-dependent drug-response study in 2D and 3D, PC-3 cells were cultured as monolayers and in a low stiffness LunaGel with a stiffness of approximately 4 kPa for up to 20 days and analysed three, six, nine and fourteen days after docetaxel addition (0.01 µM, 0.1 µM, 1 µM, 10 µM, 100 µM, 1,000 µM). In 2D cell culture, an IC₅₀ of around 181 µM after three days of drug treatment was determined, which is substantially higher than 0.629 nM [152] or 8 nM [153] as previously reported. Yang et al. demonstrated that docetaxel inhibited the growth and induced the apoptosis of human prostate cancer cells in 2D standard cell cultures in a concentration-dependent manner [154]. However, the authors noted that androgen receptor (AR) independent cells, such as PC-3, had increased resistance to docetaxel compared to AR-dependent cells, such as LNCaP cells.

For PC-3 cells cultured in LunaGel, an IC₅₀ of 360 µM based on cell number measurements and an IC₅₀ of around 500 µM based on viability calculations were determined, which is more than twice the determined IC₅₀ value of PC-3 cells cultured in 2D. These results correspond to different studies, were the inhibitory effect of docetaxel on prostate cancer cells was also decreased in 3D compared to 2D standard cell cultures [73], [155], [156]. Hence, higher concentrations of docetaxel are necessary to decrease the cell viability of 3D cell cultures with docetaxel treatment. Fitzgerald et al. showed that PC-3 cells cultured on 3D porous collagen-

nanohydroxyapatite scaffolds had an increased docetaxel resistance compared to 2D cultures but not between groups cultured in 3D and treated with docetaxel concentrations of 1 nM, 10 nM and 100 nM [73]. In line with the observation that 3D models of PC-3 cells were more resistant to DMSO than monolayer cultures, the IC₅₀ determination indicates that many 3D cell models are more resistant to drugs than 2D cell models and that resistant populations remain in the 3D models [71], [157], [158].

With respect to the overall decreasing number of cells per area within the 3D cell cultures, the cells have been cultured in a low stiffness hydrogel with a compressive modulus of approximately 4 kPa, as described elsewhere [159], [160]. Similarly, a Young's modulus between 0.3 and 6.7 kPa has been described for human PC-3 tumour xenografts explanted from mice [159]. However, in the diagnosis of prostate cancer, cut-off values for the Young's modulus of elasticity between 33 and 62 kPa are used for discriminating cancerous tissue [161]–[163], indicating that the stiffness of the intrinsic prostate cancer tissues is substantially higher than the stiffness of the hydrogels used to cultivate prostate cancer cells. Hence, this difference between the environment of cultivated cells and the intrinsic tumour environment might also affect the viability of 3D tumour models.

One drawback of the employed viability determination is that the viability is calculated as the percentage of live cells of the sum of live and dead cells. This method requires the staining of all live and dead cells and subsequent imaging. Here, EthD-III was used to stain dead cells. Although ethidium dimer is a nucleic acid dye, it only reliably stains double-stranded DNA, whereas the sensitivity for denatured DNA is reduced by half [164]. However, DMSO in high concentrations denatures DNA [165], [166], so that the detection of dead cells in samples with high DMSO concentrations, such as the positive control or the samples treated with 1,000 µM docetaxel, is limited

Regarding the imaging capabilities of the OMSM, differentiations in cell size, shape, circularity and fluorescence intensity can be assessed since live cells were clearly visible in the Z-projection images and subsequent image analysis in regard to average size and circularity with ImageJ. There were high deviations in the absolute cell numbers between individual samples within one group. This might be caused by an accumulation of cells within certain regions of the specimen and uneven distribution of the cells within the hydrogel specimen caused by insufficient manual mixing. By using the optimised mixing procedure, the distribution of the cells in the hydrogel

might be improved, as shown in 4.1.1.3, and thus, the deviation between individual samples could be reduced.

The analysis of the average cell size indicates the formation of cell clusters. Still, it is also an indicator of the presence of fluorescence crosstalk, e.g. the live cells in the sample group treated with 1,000 µM docetaxel had a similar average size as the dead cells. In contrast, the live cells of the control groups were significantly bigger in size. This could be caused by excitation of EthD-III with the light of the blue LED and hence, captured in the “Calcein channel” of the microscope. Comparing the average size of live cells of 2D and 3D cultures, it was determined that the average size of 335 µm² across all samples of cells cultured in monolayers was higher than the average size of 210 µm² of cells cultured in 3D. In 2D, cells are adherent and stretch on the plastic surface while being flat on the ground; whereas, in 3D, cells grow in three dimensions, but here only two dimensions were measured so that their measured average size is smaller than the average size of cells in monolayers.

In general, the proof-of-concept studies demonstrated the capability of the OMSM to perform automated drug-response assays in 2D and 3D cell cultures with a fluorescence-based readout. The assays can be evaluated in regard to cell numbers of live and dead cells, viability and morphological parameters such as average size and circularity. While viability and morphological measurements in 3D cell culture models play a crucial role in cancer drug discovery, they represent only one aspect of assessing the efficacy and potential toxicity of anti-cancer drugs. Other functional assays such as gene expression analysis, migration and invasion assays or immunofluorescence techniques are necessary to fully understand the underlying mechanism. By combining viability measurements with other functional readouts, researchers can gain a comprehensive understanding of the drug's mode of action, its efficacy against cancer cells, and its potential side effects. Thereby, the OMSM connected the biomanufacturing workstation is capable to automate assays with fluorescence-based readouts, not only viability assays but also immunofluorescence or cell invasion assays.

Although the proof-of-concept studies had limitations in repeatability due to manual handling, the repeatability will increase as soon as the OMSM can be connected to the biomanufacturing workstation and the complete workflow can be conducted automatically.

Conclusions

This chapter summarises the findings of this thesis and concludes its results. Additionally, the limitations are discussed, practical recommendations for additional research are suggested, and a general outlook to the future of automation in 3D cell culture is given.

The main objectives of this thesis were the implementation of automated workflows and the development of an opto-mechatronic screening module for the biomanufacturing workstation. A workflow for the automated production of GelMA-based hydrogels was established [17], crucial production steps were analysed and optimised to increase the reproducibility and enable the generation of a parameter library for mechanically defined hydrogels [115]. To handle the amount of automated produced hydrogels, an algorithm, *MechAnalyze*, with an intuitive graphical user interface, was developed for the subsequent fast and user-independent analysis of unconfined compression tests to advance the standardisation, reproducibility and comparability of mechanical data [108].

For the automated analysis of 3D cell culture models, an opto-mechatronic screening module was developed to be added to the biomanufacturing workstation of automated fluorescence-based imaging of 3D cell cultures. Tissue culture plates can be transported from the storage rack to the microscope and imaged with an inverted widefield microscope in the green and red fluorescence spectrum. The resolution of the microscope is comparable to commercial widefield microscopes while substantially being of lower cost and amenable to customised modifications. The proof-of-concept studies demonstrated the capability of the OMSM to perform live/dead cell viability assays on hydrogel-based 3D cell cultures. In conclusion, the OMSM expands the biomanufacturing workstation by an automated fluorescence microscope enabling the production and analysis of hydrogel-based 3D cell culture models in a reproducible manner without manual intervention. Due to the open-source and low-cost approach of this project, the automation of 3D cell cultures is not only affordable for industry and large research laboratories with sufficient funding but also for smaller-sized research laboratories with limited resources. Additionally, the open-

source and modular approach enables customisations and modifications adapted to each research setting and requirements.

Limitations and recommendation for future research

This thesis focused on implementing an automated workflow for GelMA-based hydrogels, from hydrogel precursor solution to the analysis of compression test data, and engineering an opto-mechatronic screening module with proof-of-concept studies for fluorescence-based analysis of 3D cell cultures.

Initially, it was planned to start working at the biomanufacturing workstation at QUT, develop the OMSM at FAU and then return to QUT to unite the modules. However, due to the Covid-19 pandemic, accompanied by border restrictions, and time constraints, the practical integration of the newly developed OMSM with the biomanufacturing workstation could not be realised. Hence, the complete automated workflow from hydrogel precursor solution, cell encapsulation, crosslinking and incubation to drug addition, staining and imaging could not be validated. Therefore, future studies should include the whole automated workflow. Additionally, the DoE study has not been verified by producing samples, using the predicted formulation determined by the parameter library, and validating the achieved compressive modulus. In addition, proof-of-concept studies have been carried out with one kind of hydrogel, cell-type and drug. Hence, other natural, synthetic or semi-synthetic hydrogels and different cell types capable of forming larger spheroids to demonstrate the 3D imaging capabilities of larger cell structures should be included in future studies. Aside from live/dead cell viability assays, further studies should also include live cell imaging of cell cycle and division using FUCCI cell cycle sensor or GFP- or RFP-tagged proteins to demonstrate the fluorescence capabilities of other fluorophores, as described in section 5.2.1. These studies would, in particular, demonstrate the broad application range of the workstation, time savings and increased reproducibility compared to manual handling.

In addition to future studies involving more process parameters, technical additions and modifications of the module could expand the application range and improve the analysis methods. Currently, plates must be manually transported from the storage rack into a conventional incubator and back due to the lack of an environmental chamber tissue culture to keep the cells at 37°C, 5% CO₂ and in a humidified atmosphere. An environmental chamber covering the storage rack and

imaging area would enable long-term live-cell imaging experiments and automated imaging over a time period of several days without any manual intervention. The chamber could also be used for other experimental setups such as culturing cells under hypoxic environmental conditions to mimic specific tumour microenvironments with low-oxygen levels.

In addition, automated upload of the recorded images into cloud-based storage solutions would enable on-the-fly control from the distance, which is, in the background of restricted access to laboratories during the Covid-19 pandemic even more important. In addition, automated image analysis could be implemented into the Python-based code enabling even faster and more user-independent data analysis [167], [168].

Until now, the microscope is limited to fluorescence imaging in the green and red spectra. However, the current multi-band-filter setup has a third transmission band in the UV and blue spectrum, enabling imaging of dyes, which can be excited with UV-light and emit in the blue spectrum, e.g. DNA stains such as DAPI or Hoechst 33342. Therefore, it would be necessary to include a UV-LED into the illumination unit. Besides adding another LED, the complete exchange of the current LED and filter setting is also possible to enable imaging of any required fluorophore. In addition, by implementing a white LED ring above the imaging unit, the addition of a transmission light channel is also conceivable.

General outlook

Summed up, the here presented automated workflows, algorithm, and optomechatronic screening module contribute to the automation of 3D cell culture workflows and thereby leads to a more widespread acceptance and, more importantly, application of 3D cell culture workflows.

There is a growing DIY scientific community developing open-source and low-cost DIY hardware for a wide range of applications from various 3D- and bioprinters [169], [170], microscopes for teaching, field and biomedical applications [97], [99], [100], liquid handling [80] to specialised specific applications such as autosampling [171] or a whole scientific instrument ecosystem [172].

Automation technologies can accelerate and standardise the introduction of existing and new 3D cell culture methodologies by varying the considerable amount

of possible process parameters, such as stiffness, porosity or cell adhesion motifs, more efficiently and with less human intervention to find the optimal conditions for each application. However, there is no one-fits-all solution to automation of 3D cell cultures due to the high variability in 3D cell culture techniques of scaffold-free systems, such as hanging drop and ultra-low attachment microplates, or scaffold-based systems, incorporating hydrogels or polymeric hard materials. Thus, specific requirements, e.g. viscous material handling, have to be met for each technique. Modular and open-source automation approaches adapt to the specific needs and anticipate future scientific developments by modifying existing systems or adding new technology. Especially in an academic research environment projects usually last around two to three years until new techniques come up. Here, open-source and modular technical equipment can quickly adapt to new scientific projects and methods without the need of buying new, expensive equipment, and hence, overcomes the problem of obsolescence.

Bibliography

- [1] V. E. Santo, S. P. Rebelo, M. F. Estrada, P. M. Alves, E. Boghaert, and C. Brito, “Drug screening in 3D in vitro tumor models: overcoming current pitfalls of efficacy read-outs,” *Biotechnology Journal*, vol. 12, no. 1, p. 1600505, Jan. 2017, doi: 10.1002/biot.201600505.
- [2] M. Zanoni, S. Pignatta, C. Arienti, M. Bonafè, and A. Tesei, “Anticancer drug discovery using multicellular tumor spheroid models,” *Expert Opinion on Drug Discovery*, vol. 14, no. 3, pp. 289–301, Mar. 2019, doi: 10.1080/17460441.2019.1570129.
- [3] I. Fraietta and F. Gasparri, “The development of high-content screening (HCS) technology and its importance to drug discovery,” *Expert Opinion on Drug Discovery*, vol. 11, no. 5, pp. 501–514, 2016, doi: 10.1517/17460441.2016.1165203.
- [4] S. M. Czerniecki *et al.*, “High-Throughput Screening Enhances Kidney Organoid Differentiation from Human Pluripotent Stem Cells and Enables Automated Multidimensional Phenotyping,” *Cell Stem Cell*, vol. 22, no. 6, pp. 929-940.e4, Jun. 2018, doi: 10.1016/J.STEM.2018.04.022.
- [5] A. S. Nunes, A. S. Barros, E. C. Costa, A. F. Moreira, and I. J. Correia, “3D tumor spheroids as in vitro models to mimic in vivo human solid tumors resistance to therapeutic drugs,” *Biotechnology and Bioengineering*, vol. 116, no. 1. John Wiley & Sons, Ltd, pp. 206–226, 01-Jan-2019, doi: 10.1002/bit.26845.
- [6] F. Monjaret, M. Fernandes, E. Duchemin-Pelletier, A. Argento, S. Degot, and J. Young, “Fully Automated One-Step Production of Functional 3D Tumor Spheroids for High-Content Screening,” *Journal of Laboratory Automation*, vol. 21, no. 2, pp. 268–280, 2016, doi: 10.1177/2211068215607058.
- [7] R. Lehmann, C. Gallert, T. Roddelkopf, S. Junginger, and K. Thurow, “Biomek Cell Workstation: A Flexible System for Automated 3D Cell Cultivation,” *Journal of Laboratory Automation*, vol. 21, no. 4, pp. 568–578, 2016, doi: 10.1177/2211068215594580.
- [8] F. Madoux *et al.*, “A 1536-Well 3D Viability Assay to Assess the Cytotoxic Effect of Drugs on Spheroids,” *SLAS Discovery*, vol. 22, no. 5, pp. 516–524, 2017, doi: 10.1177/2472555216686308.
- [9] Y. C. Tung, A. Y. Hsiao, S. G. Allen, Y. S. Torisawa, M. Ho, and S. Takayama, “High-throughput 3D spheroid culture and drug testing using a 384 hanging drop array,” *Analyst*, vol. 136, no. 3, pp. 473–478, Jan. 2011, doi: 10.1039/c0an00609b.
- [10] A. I. Neto *et al.*, “A novel hanging spherical drop system for the generation of cellular spheroids and high throughput combinatorial drug screening,” *Biomaterials Science*, vol. 3, no. 4, pp. 581–585, 2015, doi: 10.1039/c4bm00411f.

- [11] S. A. Langhans, “Three-dimensional in vitro cell culture models in drug discovery and drug repositioning,” *Frontiers in Pharmacology*, vol. 9, no. JAN. Frontiers, p. 6, 23-Jan-2018, doi: 10.3389/fphar.2018.00006.
- [12] Y. F. Li and E. Kumacheva, “Hydrogel microenvironments for cancer spheroid growth and drug screening,” *Science Advances*, vol. 4, no. 4, 2018, doi: 10.1126/sciadv.aas8998.
- [13] Y. J. Yu *et al.*, “Hydrogel-incorporating unit in a well: 3D cell culture for high-throughput analysis,” *Lab on a Chip*, vol. 18, no. 17, pp. 2604–2613, Aug. 2018, doi: 10.1039/c8lc00525g.
- [14] O. Sirenko, T. Mitlo, J. Hesley, S. Luke, W. Owens, and E. F. Cromwell, “High-Content Assays for Characterizing the Viability and Morphology of 3D Cancer Spheroid Cultures,” *ASSAY and Drug Development Technologies*, vol. 13, no. 7, pp. 402–414, Sep. 2015, doi: 10.1089/adt.2015.655.
- [15] N. J. Martinez, S. A. Titus, A. K. Wagner, and A. Simeonov, “High-throughput fluorescence imaging approaches for drug discovery using in vitro and in vivo three-dimensional models,” *Expert Opinion on Drug Discovery*, vol. 10, no. 12, pp. 1347–1361, 2015, doi: 10.1517/17460441.2015.1091814.
- [16] S. Eggert, P. Miesczanek, C. Meinert, and D. W. Hutmacher, “OpenWorkstation: A modular open-source technology for automated in vitro workflows,” *HardwareX*, vol. 8, p. e00152, Oct. 2020, doi: 10.1016/j.ohx.2020.e00152.
- [17] S. Eggert, M. Kahl, R. Kent, N. Bock, C. Meinert, and D. W. Hutmacher, “An Open Source Technology Platform to Manufacture Hydrogel-Based 3D Culture Models in an Automated and Standardized Fashion,” *Journal of Visualized Experiments*, vol. e61261, p. In press, 2020, doi: 10.3791/61261.
- [18] E. Henke, R. Nandigama, and S. Ergün, “Extracellular Matrix in the Tumor Microenvironment and Its Impact on Cancer Therapy,” *Frontiers in Molecular Biosciences*, vol. 6, no. January, pp. 1–24, 2020, doi: 10.3389/fmolsb.2019.00160.
- [19] D. Rodenhizer, T. C. L. of 3D I. V. T. M. W. C. H. A. A. for D. D. Dean, E. D’Arcangelo, and A. P. McGuigan, “The Current Landscape of 3D In Vitro Tumor Models: What Cancer Hallmarks Are Accessible for Drug Discovery?,” *Advanced Healthcare Materials*, vol. 7, no. 8, p. 1701174, Apr. 2018, doi: 10.1002/adhm.201701174.
- [20] A. Malandrino, M. Mak, R. D. Kamm, and E. Moeendarbary, “Complex mechanics of the heterogeneous extracellular matrix in cancer,” *Extreme Mechanics Letters*, vol. 21, pp. 25–34, 2018, doi: 10.1016/j.eml.2018.02.003.
- [21] C. A. J. Hoeve and P. J. Flory, “The elastic properties of elastin,” *Biopolymers*, vol. 13, no. 4, pp. 677–686, Apr. 1974, doi: 10.1002/bip.1974.360130404.
- [22] S. Sasikumar, S. Chameettachal, B. Cromer, F. Pati, and P. Kingshott, “Decellularized extracellular matrix hydrogels – cell behavior as function of matrix stiffness,” *Current Opinion in Biomedical Engineering*, May 2019, doi:

- [23] E. E. Antoine, P. P. Vlachos, and M. N. Rylander, “Review of Collagen I Hydrogels for Bioengineered Tissue Microenvironments: Characterization of Mechanics, Structure, and Transport,” *Tissue Engineering Part B: Reviews*, vol. 20, no. 6, pp. 683–696, Dec. 2014, doi: 10.1089/ten.teb.2014.0086.
- [24] M. J. Kratochvil, A. J. Seymour, T. L. Li, S. P. Paşa, C. J. Kuo, and S. C. Heilshorn, “Engineered materials for organoid systems,” *Nature Reviews Materials*, vol. 4, no. 9. Nature Publishing Group, pp. 606–622, 16-Aug-2019, doi: 10.1038/s41578-019-0129-9.
- [25] O. Chaudhuri *et al.*, “Hydrogels with tunable stress relaxation regulate stem cell fate and activity,” *Nature Materials*, vol. 15, no. 3, pp. 326–334, Mar. 2016, doi: 10.1038/nmat4489.
- [26] H. P. Lee, L. Gu, D. J. Mooney, M. E. Levenston, and O. Chaudhuri, “Mechanical confinement regulates cartilage matrix formation by chondrocytes,” *Nature Materials*, vol. 16, no. 12, pp. 1243–1251, Dec. 2017, doi: 10.1038/nmat4993.
- [27] Y. Wu *et al.*, “The influence of the stiffness of GelMA substrate on the outgrowth of PC12 cells,” *Bioscience Reports*, vol. 39, no. 1, p. BSR20181748, Jan. 2019, doi: 10.1042/bsr20181748.
- [28] R. S. Stowers *et al.*, “Matrix stiffness induces a tumorigenic phenotype in mammary epithelium through changes in chromatin accessibility,” *Nature Biomedical Engineering*, p. 1, Jul. 2019, doi: 10.1038/s41551-019-0420-5.
- [29] C. H. Lin, J. J. M. Su, S. Y. Lee, and Y. M. Lin, “Stiffness modification of photopolymerizable gelatin-methacrylate hydrogels influences endothelial differentiation of human mesenchymal stem cells,” *Journal of Tissue Engineering and Regenerative Medicine*, vol. 12, no. 10, pp. 2099–2111, 2018, doi: 10.1002/jterm.2745.
- [30] M. Costantini *et al.*, “Engineering Muscle Networks in 3D Gelatin Methacryloyl Hydrogels: Influence of Mechanical Stiffness and Geometrical Confinement,” *Frontiers in Bioengineering and Biotechnology*, vol. 5, no. April, pp. 1–8, 2017, doi: 10.3389/fbioe.2017.00022.
- [31] L. V Thomas, R. VG, and P. D Nair, “Effect of stiffness of chitosan-hyaluronic acid dialdehyde hydrogels on the viability and growth of encapsulated chondrocytes,” *International Journal of Biological Macromolecules*, vol. 104, pp. 1925–1935, 2017, doi: 10.1016/j.ijbiomac.2017.05.116.
- [32] H. Ko *et al.*, “A simple layer-stacking technique to generate biomolecular and mechanical gradients in photocrosslinkable hydrogels,” *Biofabrication*, vol. 11, no. 2, p. 025014, Mar. 2019, doi: 10.1088/1758-5090/ab08b5.
- [33] I. Levental, P. C. Georges, and P. A. Janmey, “Soft biological materials and their impact on cell function,” *Soft Matter*, vol. 3, no. 3, pp. 299–306, Feb. 2007, doi: 10.1039/B610522J.

- [34] F. H. Silver, G. Bradica, and A. Tria, “Elastic energy storage in human articular cartilage: estimation of the elastic modulus for type II collagen and changes associated with osteoarthritis,” *Matrix Biology*, vol. 21, no. 2, pp. 129–137, Mar. 2002, doi: 10.1016/S0945-053X(01)00195-0.
- [35] D. T. Reilly, A. H. Burstein, and V. H. Frankel, “The elastic modulus for bone,” *Journal of Biomechanics*, vol. 7, no. 3, pp. 271–275, May 1974, doi: 10.1016/0021-9290(74)90018-9.
- [36] A. J. Engler, S. Sen, H. L. Sweeney, and D. E. Discher, “Matrix Elasticity Directs Stem Cell Lineage Specification,” *Cell*, vol. 126, no. 4, pp. 677–689, Aug. 2006, doi: 10.1016/J.CELL.2006.06.044.
- [37] A. Buxboim, K. Rajagopal, A. E. X. Brown, and D. E. Discher, “How deeply cells feel: Methods for thin gels,” *Journal of Physics Condensed Matter*, vol. 22, no. 19, p. 194116, May 2010, doi: 10.1088/0953-8984/22/19/194116.
- [38] S. R. Caliari and J. A. Burdick, “A practical guide to hydrogels for cell culture,” *Nature Methods*, vol. 13, no. 5, pp. 405–414, May 2016, doi: 10.1038/nmeth.3839.
- [39] E. O. Mosaad, K. F. Chambers, K. Futrega, J. A. Clements, and M. R. Doran, “The Microwell-mesh: A high-throughput 3D prostate cancer spheroid and drug-testing platform,” *Scientific Reports*, vol. 8, no. 1, p. 253, Dec. 2018, doi: 10.1038/s41598-017-18050-1.
- [40] E. T. Verjans, J. Doijen, W. Luyten, B. Landuyt, and L. Schoofs, “Three-dimensional cell culture models for anticancer drug screening: Worth the effort?,” *Journal of Cellular Physiology*, vol. 233, no. 4. John Wiley & Sons, Ltd, pp. 2993–3003, 01-Apr-2018, doi: 10.1002/jcp.26052.
- [41] P. Joshi, A. Datar, K. N. Yu, S. Y. Kang, and M. Y. Lee, “High-content imaging assays on a miniaturized 3D cell culture platform,” *Toxicology in Vitro*, vol. 50, no. February, pp. 147–159, 2018, doi: 10.1016/j.tiv.2018.02.014.
- [42] B. J. Engel *et al.*, “Multilayered, Hyaluronic Acid-Based Hydrogel Formulations Suitable for Automated 3D High Throughput Drug Screening of Cancer-Stromal Cell Cocultures,” *Advanced Healthcare Materials*, vol. 4, no. 11, pp. 1664–1674, 2015, doi: 10.1002/adhm.201500258.
- [43] A. Rodallec *et al.*, “From 3D spheroids to tumor bearing mice: efficacy and distribution studies of trastuzumab-docetaxel immunoliposome in breast cancer,” *International journal of nanomedicine*, vol. 13, pp. 6677–6688, 2018, doi: 10.2147/IJN.S179290.
- [44] J. M. Lee *et al.*, “Generation of uniform-sized multicellular tumor spheroids using hydrogel microwells for advanced drug screening,” *Scientific reports*, vol. 8, no. 1, p. 17145, Dec. 2018, doi: 10.1038/s41598-018-35216-7.
- [45] E. Kaemmerer, F. P. W. Melchels, B. M. Holzapfel, T. Meckel, D. W. Hutmacher, and D. Loessner, “Gelatine methacrylamide-based hydrogels: An alternative three-dimensional cancer cell culture system,” *Acta Biomaterialia*, vol. 10, no. 6, pp. 2551–2562, Jun. 2014, doi: 10.1016/j.actbio.2014.02.035.

- [46] F. Ruedinger, A. Lavrentieva, C. Blume, I. Pepelanova, and T. Schepers, “Hydrogels for 3D mammalian cell culture: a starting guide for laboratory practice,” *Applied Microbiology and Biotechnology*, vol. 99, no. 2. Springer Berlin Heidelberg, pp. 623–636, 30-Jan-2015, doi: 10.1007/s00253-014-6253-y.
- [47] L. Moroni *et al.*, “Biofabrication strategies for 3D in vitro models and regenerative medicine,” *Nature Reviews Materials*, vol. 3, no. 5. Nature Publishing Group, pp. 21–37, 26-May-2018, doi: 10.1038/s41578-018-0006-y.
- [48] M. Norouzi, B. Nazari, and D. W. Miller, “Injectable hydrogel-based drug delivery systems for local cancer therapy,” *Drug Discovery Today*, vol. 21, no. 11. Elsevier Ltd, pp. 1835–1849, 01-Nov-2016, doi: 10.1016/j.drudis.2016.07.006.
- [49] M. Vigata, C. D. O’Connell, S. Cometta, D. W. Hutmacher, C. Meinert, and N. Bock, “Gelatin Methacryloyl Hydrogels for the Localized Delivery of Cefazolin,” *Polymers*, vol. 13, no. 22, p. 3960, Nov. 2021, doi: 10.3390/polym13223960.
- [50] J. Yang, Y. S. Zhang, K. Yue, and A. Khademhosseini, “Cell-laden hydrogels for osteochondral and cartilage tissue engineering,” *Acta Biomaterialia*, vol. 57. Acta Materialia Inc, pp. 1–25, 15-Jul-2017, doi: 10.1016/j.actbio.2017.01.036.
- [51] T. Chen *et al.*, “Ultratough, Self-Healing, and Tissue-Adhesive Hydrogel for Wound Dressing,” *ACS Applied Materials and Interfaces*, vol. 10, no. 39, pp. 33523–33531, Oct. 2018, doi: 10.1021/acsami.8b10064.
- [52] E. Caló and V. V. Khutoryanskiy, “Biomedical applications of hydrogels: A review of patents and commercial products,” *European Polymer Journal*, vol. 65. Elsevier Ltd, pp. 252–267, 01-Apr-2015, doi: 10.1016/j.eurpolymj.2014.11.024.
- [53] H. H. G. Song, K. M. Park, and S. Gerecht, “Hydrogels to model 3D in vitro microenvironment of tumor vascularization,” *Advanced Drug Delivery Reviews*, vol. 79. pp. 19–29, 2014, doi: 10.1016/j.addr.2014.06.002.
- [54] I. Mironi-Harpaz, D. Y. Wang, S. Venkatraman, and D. Seliktar, “Photopolymerization of cell-encapsulating hydrogels: Crosslinking efficiency versus cytotoxicity,” *Acta Biomaterialia*, vol. 8, no. 5, pp. 1838–1848, May 2012, doi: 10.1016/j.actbio.2011.12.034.
- [55] N. A. Peppas and A. S. Hoffman, “Hydrogels,” in *Biomaterials Science*, 4th Editio., no. 1, W. R. Wagner, S. E. Sakiyama-Elbert, G. Zhang, and M. J. Yaszemski, Eds. 2020, pp. 153–166.
- [56] D. Loessner *et al.*, “Functionalization, preparation and use of cell-laden gelatin methacryloyl-based hydrogels as modular tissue culture platforms,” *Nature Protocols*, vol. 11, no. 4, pp. 727–746, Mar. 2016, doi: 10.1038/nprot.2016.037.
- [57] C. D. O’Connell *et al.*, “Tailoring the mechanical properties of gelatin methacryloyl hydrogels through manipulation of the photocrosslinking

- conditions,” *Soft Matter*, vol. 14, no. 11, pp. 2142–2151, Mar. 2018, doi: 10.1039/c7sm02187a.
- [58] W. Schuurman *et al.*, “Gelatin-Methacrylamide Hydrogels as Potential Biomaterials for Fabrication of Tissue-Engineered Cartilage Constructs,” *Macromolecular Bioscience*, vol. 13, no. 5, pp. 551–561, May 2013, doi: 10.1002/mabi.201200471.
- [59] N. Monteiro *et al.*, “Photopolymerization of cell-laden gelatin methacryloyl hydrogels using a dental curing light for regenerative dentistry,” *Dental Materials*, vol. 34, no. 3, pp. 389–399, 2018, doi: 10.1016/j.dental.2017.11.020.
- [60] N. Ersimo, C. E. Witherel, and K. L. Spiller, “Differences in time-dependent mechanical properties between extruded and molded hydrogels,” *Biofabrication*, vol. 8, no. 3, p. 035012, Aug. 2016, doi: 10.1088/1758-5090/8/3/035012.
- [61] O. Bas *et al.*, “Rational design and fabrication of multiphasic soft network composites for tissue engineering articular cartilage: A numerical model-based approach,” *Chemical Engineering Journal*, vol. 340, pp. 15–23, May 2018, doi: 10.1016/j.cej.2018.01.020.
- [62] Z. Wang *et al.*, “Visible Light Photoinitiation of Cell-Adhesive Gelatin Methacryloyl Hydrogels for Stereolithography 3D Bioprinting,” *ACS Applied Materials and Interfaces*, vol. 10, no. 32, pp. 26859–26869, 2018, doi: 10.1021/acsami.8b06607.
- [63] C. S. Bahney, T. J. Lujan, C. W. Hsu, M. Bottlang, J. L. West, and B. Johnstone, “Visible light photoinitiation of mesenchymal stem cell-laden bioresponsive hydrogels,” *European Cells and Materials*, vol. 22, pp. 43–55, Jul. 2011, doi: 10.22203/eCM.v022a04.
- [64] K. S. Lim *et al.*, “New Visible-Light Photoinitiating System for Improved Print Fidelity in Gelatin-Based Bioinks,” *ACS Biomaterials Science and Engineering*, vol. 2, no. 10, pp. 1752–1762, 2016, doi: 10.1021/acsbiomaterials.6b00149.
- [65] B. D. Fairbanks, M. P. Schwartz, C. N. Bowman, and K. S. Anseth, “Photoinitiated polymerization of PEG-diacrylate with lithium phenyl-2,4,6-trimethylbenzoylphosphinate: polymerization rate and cytocompatibility,” *Biomaterials*, vol. 30, no. 35, pp. 6702–6707, Dec. 2009, doi: 10.1016/j.biomaterials.2009.08.055.
- [66] F. Sensi, E. D’Angelo, S. D’Aronco, R. Molinaro, and M. Agostini, “Preclinical three-dimensional colorectal cancer model: The next generation of in vitro drug efficacy evaluation,” *Journal of Cellular Physiology*, vol. 234, no. 1. John Wiley & Sons, Ltd, pp. 181–191, 01-Jan-2018, doi: 10.1002/jcp.26812.
- [67] S. Rhee and F. Grinnell, “Fibroblast mechanics in 3D collagen matrices,” *Advanced Drug Delivery Reviews*, vol. 59, no. 13. Elsevier, pp. 1299–1305, 10-Nov-2007, doi: 10.1016/j.addr.2007.08.006.

- [68] R. Edmondson, J. J. Broglie, A. F. Adcock, and L. Yang, “Three-Dimensional Cell Culture Systems and Their Applications in Drug Discovery and Cell-Based Biosensors,” *ASSAY and Drug Development Technologies*, vol. 12, no. 4, pp. 207–218, 2014, doi: 10.1089/adt.2014.573.
- [69] N. Baek, O. W. Seo, M. Kim, J. Hulme, and S. S. A. An, “Monitoring the effects of doxorubicin on 3D-spheroid tumor cells in real-time,” *Oncotargets and Therapy*, vol. Volume 9, pp. 7207–7218, Nov. 2016, doi: 10.2147/OTT.S112566.
- [70] M. Lal-Nag *et al.*, “Exploring Drug Dosing Regimens In Vitro Using Real-Time 3D Spheroid Tumor Growth Assays,” *SLAS Discovery*, vol. 22, no. 5, pp. 537–546, 2017, doi: 10.1177/2472555217698818.
- [71] T. B. Shelp, C. J. Lovitt, and V. M. Avery, “Assessing Drug Efficacy in a Miniaturized Pancreatic Cancer *In Vitro* 3D Cell Culture Model,” *ASSAY and Drug Development Technologies*, vol. 14, no. 7, pp. 367–380, 2016, doi: 10.1089/adt.2016.737.
- [72] T. H. Booij *et al.*, “Development of a 3D tissue culture-based high-content screening platform that uses phenotypic profiling to discriminate selective inhibitors of receptor tyrosine kinases,” *Journal of Biomolecular Screening*, vol. 21, no. 9, pp. 912–922, Oct. 2016, doi: 10.1177/1087057116657269.
- [73] K. A. Fitzgerald *et al.*, “The use of collagen-based scaffolds to simulate prostate cancer bone metastases with potential for evaluating delivery of nanoparticulate gene therapeutics,” *Biomaterials*, vol. 66, pp. 53–66, 2015, doi: 10.1016/j.biomaterials.2015.07.019.
- [74] V. Härmä *et al.*, “A comprehensive panel of three-dimensional models for studies of prostate cancer growth, invasion and drug responses,” *PLoS ONE*, vol. 5, no. 5, p. e10431, May 2010, doi: 10.1371/journal.pone.0010431.
- [75] L. Li, Q. Zhou, T. C. Voss, K. L. Quick, and D. V. LaBarbera, “High-throughput imaging: Focusing in on drug discovery in 3D,” *Methods*, vol. 96, pp. 97–102, 2015, doi: 10.1016/j.ymeth.2015.11.013.
- [76] T. H. Booij, L. S. Price, and E. H. J. Danen, “3D Cell-Based Assays for Drug Screens: Challenges in Imaging, Image Analysis, and High-Content Analysis,” *SLAS DISCOVERY: Advancing Life Sciences R&D*, vol. 1, no. 13, p. 247255521983008, Feb. 2019, doi: 10.1177/2472555219830087.
- [77] N. Blow, “Lab automation: Tales along the road to automation,” *Nature Methods*, vol. 5, no. 1, pp. 109–112, Jan. 2008, doi: 10.1038/nmeth0108-109.
- [78] G. Lippi and G. Da Rin, “Advantages and limitations of total laboratory automation: a personal overview,” *Clinical Chemistry and Laboratory Medicine (CCLM)*, vol. 57, no. 6, pp. 802–811, May 2019, doi: 10.1515/cclm-2018-1323.
- [79] F. Kong, L. Yuan, Y. F. Zheng, and W. Chen, “Automatic liquid handling for life science: A critical review of the current state of the art,” *Journal of Laboratory Automation*, vol. 17, no. 3, pp. 169–185, 2012, doi: 10.1177/2211068211435302.

- [80] F. Barthels, U. Barthels, M. Schwickert, and T. Schirmeister, “FINDUS: An Open-Source 3D Printable Liquid-Handling Workstation for Laboratory Automation in Life Sciences,” *SLAS Technology*, vol. 25, no. 2, pp. 190–199, 2020, doi: 10.1177/2472630319877374.
- [81] J. P. Celli *et al.*, “An imaging-based platform for high-content, quantitative evaluation of therapeutic response in 3D tumour models,” *Scientific Reports*, vol. 4, no. 1, p. 3751, May 2014, doi: 10.1038/srep03751.
- [82] M. Engel, L. Belfiore, B. Aghaei, and M. Sutija, “Enabling high throughput drug discovery in 3D cell cultures through a novel bioprinting workflow,” *SLAS Technology*, vol. 27, no. 1, pp. 32–38, Feb. 2022, doi: 10.1016/J.SLAST.2021.10.002.
- [83] M. Rimann, B. Angres, I. Patocchi-Tenzer, S. Braum, and U. Graf-Hausner, “Automation of 3D Cell Culture Using Chemically Defined Hydrogels,” *Journal of Laboratory Automation*, vol. 19, no. 2, pp. 191–197, 2014, doi: 10.1177/2211068213508651.
- [84] opentrons, “Opentrons API,” 2019. [Online]. Available: <https://docs.opentrons.com/ot1/index.html>. [Accessed: 04-Nov-2019].
- [85] V. Ljosa and A. E. Carpenter, “Introduction to the quantitative analysis of two-dimensional fluorescence microscopy images for cell-based screening,” *PLoS Computational Biology*, vol. 5, no. 12. Public Library of Science, p. e1000603, 2009, doi: 10.1371/journal.pcbi.1000603.
- [86] J. W. Lichtman and J. A. Conchello, “Fluorescence microscopy,” *Nature Methods*, vol. 2, no. 12. Nature Publishing Group, pp. 910–919, 18-Nov-2005, doi: 10.1038/nmeth817.
- [87] E. F. Schubert, “Light Emitting Diodes, 2nd Edition,” *Springer Verlag Berlin Heidelberg New York: Cambridge University Press*, p. 422, 2006.
- [88] T. Sato and V. N. Murthy, “Light-emitting diodes for biological microscopy,” *Cold Spring Harbor Protocols*, vol. 7, no. 12, pp. 1211–1222, 2012, doi: 10.1101/pdb.top072306.
- [89] D. Love and I. Goodhand, “Optimal LED Filtering for Fluorescence Microscopy,” *Microscopy Today*, vol. 27, no. 05, Cambridge University Press (CUP), pp. 26–30, Sep-2019.
- [90] D. F. Albeanu, E. Soucy, T. F. Sato, M. Meister, and V. N. Murthy, “LED arrays as cost effective and efficient light sources for widefield microscopy,” *PLoS ONE*, vol. 3, no. 5, p. e2146, May 2008, doi: 10.1371/journal.pone.0002146.
- [91] J. T. Wessels, U. Pliquett, and F. S. Wouters, “Light-emitting diodes in modern microscopy—from David to Goliath?,” *Cytometry Part A*, vol. 81 A, no. 3, pp. 188–197, 2012, doi: 10.1002/cyto.a.22023.
- [92] D. C. Swinney and J. Anthony, “How were new medicines discovered?,” *Nature Reviews Drug Discovery*, vol. 10, no. 7, pp. 507–519, Jul. 2011, doi: 10.1038/nrd3480.

- [93] Y. Fang and R. M. Eglen, “Three-Dimensional Cell Cultures in Drug Discovery and Development,” *SLAS Discovery*, vol. 22, no. 5, pp. 456–472, 2017, doi: 10.1177/1087057117696795.
- [94] M. Boutros, F. Heigwer, and C. Laufer, “Microscopy-Based High-Content Screening,” *Cell*, vol. 163, no. 6, pp. 1314–1325, 2015, doi: 10.1016/j.cell.2015.11.007.
- [95] C. Wenzel *et al.*, “3D high-content screening for the identification of compounds that target cells in dormant tumor spheroid regions,” *Experimental Cell Research*, vol. 323, no. 1, pp. 131–143, Apr. 2014, doi: 10.1016/j.yexcr.2014.01.017.
- [96] Z. Di *et al.*, “Ultra high content image analysis and phenotype profiling of 3D cultured micro-tissues,” *PLoS ONE*, vol. 9, no. 10, p. e109688, Oct. 2014, doi: 10.1371/journal.pone.0109688.
- [97] J. T. Collins *et al.*, “Robotic microscopy for everyone: the OpenFlexure microscope,” *Biomedical Optics Express*, vol. 11, no. 5, p. 2447, 2020, doi: 10.1364/boe.385729.
- [98] M. Wincott, R. M. Parton, A. Jefferson, I. M. Dobbie, M. J. Booth, and I. Davis, “Democratising ‘Microscopi’: a 3D printed automated XYZT fluorescence imaging system for teaching, outreach and fieldwork,” *Wellcome Open Research*, vol. 6, 2021, doi: 10.12688/WELLCOMEOPENRES.16536.1.
- [99] G. O. T. Merces, C. Kennedy, B. Lenoci, E. G. Reynaud, N. Burke, and M. Pickering, “The incubot: A 3D printer-based microscope for long-term live cell imaging within a tissue culture incubator,” *HardwareX*, vol. 9, p. e00189, Apr. 2021, doi: 10.1016/j.ohx.2021.e00189.
- [100] A. Maia Chagas, L. L. Prieto-Godino, A. B. Arrenberg, and T. Baden, “The €100 lab: A 3D-printable open-source platform for fluorescence microscopy, optogenetics, and accurate temperature control during behaviour of zebrafish, *Drosophila*, and *Caenorhabditis elegans*,” *PLoS Biology*, vol. 15, no. 7, p. e2002702, Jul. 2017, doi: 10.1371/journal.pbio.2002702.
- [101] B. Diederich *et al.*, “A versatile and customizable low-cost 3D-printed open standard for microscopic imaging,” *Nature Communications*, vol. 11, no. 1, pp. 1–9, Dec. 2020, doi: 10.1038/s41467-020-19447-9.
- [102] B. Wijnen, E. E. Petersen, E. J. Hunt, and J. M. Pearce, “Free and open-source automated 3-D microscope,” *Journal of Microscopy*, vol. 264, no. 2, pp. 238–246, Nov. 2016, doi: 10.1111/jmi.12433.
- [103] T. Aidukas, R. Eckert, A. R. Harvey, L. Waller, and P. C. Konda, “Low-cost, sub-micron resolution, wide-field computational microscopy using opensource hardware,” *Scientific Reports*, vol. 9, no. 1, pp. 1–12, 2019, doi: 10.1038/s41598-019-43845-9.
- [104] D. Schneidereit, L. Kraus, J. C. Meier, O. Friedrich, and D. F. Gilbert, “Step-by-step guide to building an inexpensive 3D printed motorized positioning stage for automated high-content screening microscopy,” *Biosensors and*

Bioelectronics, vol. 92, no. August 2016, pp. 472–481, Jun. 2017, doi: 10.1016/j.bios.2016.10.078.

- [105] T. Campbell and J. F. X. Jones, “Design and Implementation of a Low Cost , Modular , Adaptable and Open-Source XYZ Positioning System for Neurophysiology,” *HardwareX*, p. e00098, 2020, doi: 10.1016/j.ohx.2020.e00098.
- [106] J. J. Han, “FDA Modernization Act 2.0 allows for alternatives to animal testing,” *Artificial Organs*, vol. 47, no. 3, pp. 449–450, Mar. 2023, doi: 10.1111/aor.14503.
- [107] H. Tye, “Application of statistical ‘design of experiments’ methods in drug discovery,” *Drug Discovery Today*, vol. 9, no. 11, pp. 485–491, Jun. 2004, doi: 10.1016/S1359-6446(04)03086-7.
- [108] M. Kahl, D. Schneidereit, N. Bock, O. Friedrich, D. W. Hutmacher, and C. Meinert, “MechAnalyze – an algorithm for standardization and automation of compression test analysis,” *Tissue Engineering Part C: Methods*, vol. 27, no. 10, pp. 529–542, 2021, doi: 10.1089/ten.tec.2021.0170.
- [109] J. M. Bland and D. G. Altman, “Measuring agreement in method comparison studies,” *Statistical Methods in Medical Research*, vol. 8, no. 2, pp. 135–160, Apr. 1999, doi: 10.1177/096228029900800204.
- [110] P. Theer, C. Mongis, and M. Knop, “PSFj: know your fluorescence microscope,” *Nature Methods* 2014 11:10, vol. 11, no. 10, pp. 981–982, Sep. 2014, doi: 10.1038/nmeth.3102.
- [111] A. K. Nguyen, P. L. Goering, V. Reipa, and R. J. Narayan, “Toxicity and photosensitizing assessment of gelatin methacryloyl-based hydrogels photoinitiated with lithium phenyl-2,4,6-trimethylbenzoylphosphinate in human primary renal proximal tubule epithelial cells,” *Biointerphases*, vol. 14, no. 2, p. 021007, 2019, doi: 10.1116/1.5095886.
- [112] J. W. Nichol, S. T. Koshy, H. Bae, C. M. Hwang, S. Yamanlar, and A. Khademhosseini, “Cell-laden microengineered gelatin methacrylate hydrogels,” *Biomaterials*, vol. 31, no. 21, pp. 5536–5544, Jul. 2010, doi: 10.1016/j.biomaterials.2010.03.064.
- [113] I. Noshadi *et al.*, “In vitro and in vivo analysis of visible light crosslinkable gelatin methacryloyl (GelMA) hydrogels,” *Biomaterials Science*, vol. 5, no. 10, pp. 2093–2105, 2017, doi: 10.1039/c7bm00110j.
- [114] H. Suo, D. Zhang, J. Yin, J. Qian, Z. L. Wu, and J. Fu, “Interpenetrating polymer network hydrogels composed of chitosan and photocrosslinkable gelatin with enhanced mechanical properties for tissue engineering,” *Materials Science and Engineering C*, vol. 92, no. July, pp. 612–620, 2018, doi: 10.1016/j.msec.2018.07.016.
- [115] S. Eggert, M. Kahl, N. Bock, C. Meinert, O. Friedrich, and D. W. Hutmacher, “An open-source technology platform to increase reproducibility and enable high-throughput production of tailorable gelatin methacryloyl (GelMA) - based hydrogels,” *Materials and Design*, vol. 204, p. 109619, 2021, doi:

10.1016/j.matdes.2021.109619.

- [116] M. Kahl, D. Schneidereit, C. Meinert, N. Bock, D. W. Hutmacher, and O. Friedrich, “A fluorescence-based opto-mechatronic screening module (OMSM) for automated 3D cell culture workflows,” *Biosensors and Bioelectronics*: X, vol. 14, 2023, doi: 10.1016/j.biosx.2023.100372.
- [117] G. Lippi, G. Lima-Oliveira, G. Brocco, A. Bassi, and G. L. Salvagno, “Estimating the intra- and inter-individual imprecision of manual pipetting,” *Clinical Chemistry and Laboratory Medicine*, vol. 55, no. 7, pp. 962–966, Jun. 2017, doi: 10.1515/CCLM-2016-0810/MACHINEREADABLECITATION/RIS.
- [118] I. Semac, G. Horak, A. Jordan, and P. Zucchelli, “Pipetting Performances by Means of the Andrew Robot,” Geneva, 2013.
- [119] K. H. Lochner, T. Ballweg, and H. H. Fahrenkrog, “Factors influencing the measuring accuracy of piston pipettes with air interface,” *Laboratoriums Medizin*, vol. 20, no. 7–8, pp. 430–440, Jan. 1996, doi: 10.1515/LABM.1996.20.7-8.430/MACHINEREADABLECITATION/RIS.
- [120] M. W. Lutz *et al.*, “Experimental design for high-throughput screening,” *Drug Discovery Today*, vol. 1, no. 7, pp. 277–286, Jul. 1996, doi: 10.1016/1359-6446(96)10025-8.
- [121] L. A. S. Callahan, “Combinatorial method/high throughput strategies for hydrogel optimization in tissue engineering applications,” *Gels*, vol. 2, no. 2, 2016, doi: 10.3390/gels2020018.
- [122] P. Moshayedi *et al.*, “Systematic optimization of an engineered hydrogel allows for selective control of human neural stem cell survival and differentiation after transplantation in the stroke brain,” *Biomaterials*, vol. 105, pp. 145–155, Oct. 2016, doi: 10.1016/j.biomaterials.2016.07.028.
- [123] L. R. Nih *et al.*, “Engineered HA hydrogel for stem cell transplantation in the brain: Biocompatibility data using a design of experiment approach,” *Data in Brief*, vol. 10, pp. 202–209, Feb. 2017, doi: 10.1016/j.dib.2016.11.069.
- [124] J. Lam, S. T. Carmichael, W. E. Lowry, and T. Segura, “Hydrogel design of experiments methodology to optimize hydrogel for iPSC-NPC culture,” *Advanced Healthcare Materials*, vol. 4, no. 4, pp. 534–539, Mar. 2015, doi: 10.1002/adhm.201400410.
- [125] M. M. Pakulska, K. Vulic, R. Y. Tam, and M. S. Shoichet, “Hybrid Crosslinked Methylcellulose Hydrogel: A Predictable and Tunable Platform for Local Drug Delivery,” *Advanced Materials*, vol. 27, no. 34, pp. 5002–5008, 2015, doi: 10.1002/adma.201502767.
- [126] C. F. Guimarães, L. Gasperini, A. P. Marques, and R. L. Reis, “The stiffness of living tissues and its implications for tissue engineering,” *Nature Reviews Materials*, vol. 5, no. 5. Nature Research, pp. 351–370, 01-May-2020, doi: 10.1038/s41578-019-0169-1.
- [127] L. E. Bertassoni *et al.*, “Direct-write bioprinting of cell-laden methacrylated

gelatin hydrogels,” *Biofabrication*, vol. 6, no. 2, p. 024105, Apr. 2014, doi: 10.1088/1758-5082/6/2/024105.

- [128] Q. Feng *et al.*, “Mechanically resilient, injectable, and bioadhesive supramolecular gelatin hydrogels crosslinked by weak host-guest interactions assist cell infiltration and in situ tissue regeneration,” *Biomaterials*, vol. 101, pp. 217–228, Sep. 2016, doi: 10.1016/j.biomaterials.2016.05.043.
- [129] T. Bronshtein *et al.*, “A mathematical model for analyzing the elasticity, viscosity, and failure of soft tissue: Comparison of native and decellularized porcine cardiac extracellular matrix for tissue engineering,” *Tissue Engineering - Part C: Methods*, vol. 19, no. 8, pp. 620–630, 2013, doi: 10.1089/ten.tec.2012.0387.
- [130] S. Huth, S. Sindt, and C. Selhuber-Unkel, “Automated analysis of soft hydrogel microindentation: Impact of various indentation parameters on the measurement of Young’s modulus,” *PLoS ONE*, vol. 14, no. 8, p. e0220281, Aug. 2019, doi: 10.1371/journal.pone.0220281.
- [131] J. M. Patel, B. C. Wise, E. D. Bonnevie, and R. L. Mauck, “A Systematic Review and Guide to Mechanical Testing for Articular Cartilage Tissue Engineering,” *Tissue Engineering Part C: Methods*, vol. 25, no. 10, pp. 593–608, 2019, doi: 10.1089/ten.tec.2019.0116.
- [132] C. Xu, G. Dai, and Y. Hong, “Recent advances in high-strength and elastic hydrogels for 3D printing in biomedical applications,” *Acta Biomaterialia*, vol. 95, pp. 50–59, 2019, doi: 10.1016/j.actbio.2019.05.032.
- [133] Y. Xiao, E. A. Friis, S. H. Gehrke, and M. S. Detamore, “Mechanical Testing of Hydrogels in Cartilage Tissue Engineering: Beyond the Compressive Modulus,” *Tissue Engineering Part B: Reviews*, vol. 19, no. 5, pp. 403–412, Oct. 2013, doi: 10.1089/ten.teb.2012.0461.
- [134] M. L. Oyen, “Mechanical characterisation of hydrogel materials,” *International Materials Reviews*, vol. 59, no. 1, pp. 44–59, 2014, doi: 10.1179/1743280413Y.0000000022.
- [135] A. Vedadghavami *et al.*, “Manufacturing of hydrogel biomaterials with controlled mechanical properties for tissue engineering applications,” *Acta Biomaterialia*, vol. 62. Elsevier, pp. 42–63, 15-Oct-2017, doi: 10.1016/j.actbio.2017.07.028.
- [136] A. Dolatshahi-Pirouz *et al.*, “A combinatorial cell-laden gel microarray for inducing osteogenic differentiation of human mesenchymal stem cells,” *Scientific Reports*, vol. 4, pp. 1–9, 2015, doi: 10.1038/srep03896.
- [137] P. A. Levett, F. P. W. Melchels, K. Schrobback, D. W. Hutmacher, J. Malda, and T. J. Klein, “A biomimetic extracellular matrix for cartilage tissue engineering centered on photocurable gelatin, hyaluronic acid and chondroitin sulfate,” *Acta Biomaterialia*, vol. 10, no. 1, pp. 214–223, 2014, doi: 10.1016/j.actbio.2013.10.005.
- [138] C. Cha *et al.*, “Structural reinforcement of cell-laden hydrogels with microfabricated three dimensional scaffolds,” *Biomaterials Science*, vol. 2, no.

- 5, pp. 703–709, Apr. 2014, doi: 10.1039/c3bm60210a.
- [139] DIN Deutsches Institut für Normung e., “DIN EN ISO 844 - Rigid cellular plastics — Determination of compression properties.” Berlin, 2019.
- [140] S. Krishnamoorthy, B. Noorani, and C. Xu, “Effects of encapsulated cells on the physical-mechanical properties and microstructure of gelatin methacrylate hydrogels,” *International Journal of Molecular Sciences*, vol. 20, no. 20, p. 5061, Oct. 2019, doi: 10.3390/ijms20205061.
- [141] H. Shin, B. D. Olsen, and A. Khademhosseini, “The mechanical properties and cytotoxicity of cell-laden double-network hydrogels based on photocrosslinkable gelatin and gellan gum biomacromolecules,” *Biomaterials*, vol. 33, no. 11, pp. 3143–3152, Apr. 2012, doi: 10.1016/j.biomaterials.2011.12.050.
- [142] J. Hatton, G. R. Davis, A. H. I. Mourad, N. Cherupurakal, R. G. Hill, and S. Mohsin, “Fabrication of porous bone scaffolds using alginate and bioactive glass,” *Journal of Functional Biomaterials*, vol. 10, no. 1, p. 15, Mar. 2019, doi: 10.3390/jfb10010015.
- [143] A. Courtney, L. M. Alvey, G. O. T. Merces, N. Burke, and M. Pickering, “The Flexiscope: a low cost, flexible, convertible and modular microscope with automated scanning and micromanipulation,” *Royal Society Open Science*, vol. 7, no. 3, p. 191949, Mar. 2020, doi: 10.1098/rsos.191949.
- [144] I. Nuñez *et al.*, “Low cost and open source multi-fluorescence imaging system for teaching and research in biology and bioengineering,” *PLOS ONE*, vol. 12, no. 11, p. e0187163, Nov. 2017, doi: 10.1371/journal.pone.0187163.
- [145] J. B. Bosse, N. S. Tanneti, I. B. Hogue, and L. W. Enquist, “Open LED Illuminator: A Simple and Inexpensive LED Illuminator for Fast Multicolor Particle Tracking in Neurons,” *PLOS ONE*, vol. 10, no. 11, p. e0143547, Nov. 2015, doi: 10.1371/journal.pone.0143547.
- [146] W. Ouyang *et al.*, “An Open-Source Modular Framework for Automated Pipetting and Imaging Applications,” *Advanced Biology*, p. 2101063, 2021, doi: 10.1002/adbi.202101063.
- [147] O. Haeberlé *et al.*, “Identification of acquisition parameters from the point spread function of a fluorescence microscope,” *Optics Communications*, vol. 196, no. September, pp. 109–117, 2001.
- [148] S. R. Horman, J. To, and A. P. Orth, “An HTS-compatible 3D colony formation assay to identify tumor-specific therapeutics,” *Journal of Biomolecular Screening*, vol. 18, no. 10, pp. 1298–1308, 2013, doi: 10.1177/1087057113499405.
- [149] L. P. Ferreira, V. M. Gaspar, L. Mendes, I. F. Duarte, and J. F. Mano, “Organotypic 3D decellularized matrix tumor spheroids for high-throughput drug screening,” *Biomaterials*, vol. 275, Aug. 2021, doi: 10.1016/J.BIOMATERIALS.2021.120983.
- [150] G. H. Patterson, “Fluorescence microscopy below the diffraction limit,”

Seminars in Cell & Developmental Biology, vol. 20, no. 8, pp. 886–893, Oct. 2009, doi: 10.1016/j.semcd.2009.08.006.

- [151] V. Harris, K. Lloyd, S. Forsey, P. Rogers, M. Roche, and C. Parker, “Short Report A Population-based Study of Prostate Cancer Chemotherapy,” *Clinical Oncology*, vol. 23, no. 10, pp. 706–708, 2011, doi: 10.1016/j.clon.2011.04.014.
- [152] W. Yang *et al.*, “Genomics of Drug Sensitivity in Cancer (GDSC): A resource for therapeutic biomarker discovery in cancer cells,” *Nucleic Acids Research*, vol. 41, no. D1, pp. D955–D961, Jan. 2013, doi: 10.1093/nar/gks1111.
- [153] H. Huang *et al.*, “Brefeldin A enhances docetaxel-induced growth inhibition and apoptosis in prostate cancer cells in monolayer and 3D cultures,” *Bioorganic and Medicinal Chemistry Letters*, vol. 27, no. 11, pp. 2286–2291, 2017, doi: 10.1016/j.bmcl.2017.04.047.
- [154] C. Yang, W. Zhang, J. Wang, P. Chen, and J. Jin, “Effect of docetaxel on the regulation of proliferation and apoptosis of human prostate cancer cells,” *Molecular Medicine Reports*, vol. 49, no. 5, pp. 3864–3870, May 2019, doi: 10.3892/mmr.2019.9998.
- [155] K. Xu, Z. Wang, J. A. Copland, R. Chakrabarti, and S. J. Florkzyk, “3D porous chitosan-chondroitin sulfate scaffolds promote epithelial to mesenchymal transition in prostate cancer cells,” *Biomaterials*, vol. 254, no. May, p. 120126, 2020, doi: 10.1016/j.biomaterials.2020.120126.
- [156] L. J. Bray *et al.*, “Multi-parametric hydrogels support 3D invitro bioengineered microenvironment models of tumour angiogenesis,” *Biomaterials*, vol. 53, pp. 609–620, 2015, doi: 10.1016/j.biomaterials.2015.02.124.
- [157] J. C. Fontoura *et al.*, “Comparison of 2D and 3D cell culture models for cell growth, gene expression and drug resistance,” *Materials Science and Engineering: C*, vol. 107, p. 110264, Feb. 2020, doi: 10.1016/J.MSEC.2019.110264.
- [158] D. Loessner, K. S. Stok, M. P. Lutolf, D. W. Hutmacher, J. A. Clements, and S. C. Rizzi, “Bioengineered 3D platform to explore cell-ECM interactions and drug resistance of epithelial ovarian cancer cells,” *Biomaterials*, vol. 31, no. 32, pp. 8494–8506, Nov. 2010, doi: 10.1016/j.biomaterials.2010.07.064.
- [159] N. L. Habbit *et al.*, “Tunable three-dimensional engineered prostate cancer tissues for in vitro recapitulation of heterogeneous in vivo prostate tumor stiffness,” *Acta Biomaterialia*, vol. 147, pp. 73–90, Jul. 2022, doi: 10.1016/J.ACTBIO.2022.05.011.
- [160] A. V Taubenberger *et al.*, “3D extracellular matrix interactions modulate tumour cell growth, invasion and angiogenesis in engineered tumour microenvironments,” *Acta Biomaterialia*, vol. 36, pp. 73–85, 2016, doi: 10.1016/j.actbio.2016.03.017.
- [161] J. M. Correas, A. M. Tissier, A. Khairoune, G. Khouri, D. Eiss, and O. Hélenon, “Ultrasound elastography of the prostate: State of the art,”

Diagnostic and Interventional Imaging, vol. 94, no. 5, pp. 551–560, May 2013, doi: 10.1016/J.DIII.2013.01.017.

- [162] O. Rouvière *et al.*, “Stiffness of benign and malignant prostate tissue measured by shear-wave elastography: a preliminary study,” *European Radiology*, vol. 27, no. 5, pp. 1858–1866, May 2017, doi: 10.1007/s00330-016-4534-9.
- [163] R. G. Barr, R. Memo, and C. R. Schaub, “Shear wave ultrasound elastography of the prostate: Initial results,” *Ultrasound Quarterly*, vol. 28, no. 1, pp. 13–20, Mar. 2012, doi: 10.1097/RUQ.0B013E318249F594.
- [164] J. Markovits, B. P. Roques, and J. B. Le Pecq, “Ethidium dimer: A new reagent for the fluorimetric determination of nucleic acids,” *Analytical Biochemistry*, vol. 94, no. 2, pp. 259–264, Apr. 1979, doi: 10.1016/0003-2697(79)90357-9.
- [165] G. Bonner and A. M. Klibanov, “Structural Stability of DNA in Nonaqueous Solvents,” *Biotechnology and Bioengineering*, vol. 68, no. 3, pp. 339–344, 2000, doi: 10.1002/(SICI)1097-0290(20000505)68:3.
- [166] X. Wang, H. J. Lim, and A. Son, “Characterization of denaturation and renaturation of DNA for DNA hybridization,” *Environmental Health and Toxicology*, vol. 29, p. e2014007, Sep. 2014, doi: 10.5620/EHT.2014.29.E2014007.
- [167] M. Georg *et al.*, “Development of image analysis software for quantification of viable cells in microchips,” *PloS one*, vol. 13, no. 3, Mar. 2018, doi: 10.1371/JOURNAL.PONE.0193605.
- [168] P. Kaifosh, J. D. Zaremba, N. B. Danielson, and A. Losonczy, “SIMA: Python software for analysis of dynamic fluorescence imaging data,” *Frontiers in neuroinformatics*, vol. 8, 2014, doi: 10.3389/FNINF.2014.00080.
- [169] M. Kahl, M. Gertig, P. Hoyer, O. Friedrich, and D. F. Gilbert, “Ultra-Low-Cost 3D Bioprinting: Modification and Application of an Off-the-Shelf Desktop 3D-Printer for Biofabrication,” *Frontiers in Bioengineering and Biotechnology*, vol. 7, p. 184, Jul. 2019, doi: 10.3389/FBIOE.2019.00184.
- [170] T. Bharadwaj and D. Verma, “Open source bioprinters: Revolutionizing the accessibility of biofabrication,” *Bioprinting*, vol. 23. Elsevier, p. e00155, 01-Aug-2021, doi: 10.1016/j.bprint.2021.e00155.
- [171] M. C. Carvalho and R. H. Murray, “Osmar, the open-source microsyringe autosampler,” *HardwareX*, vol. 3, no. December 2017, pp. 10–38, 2018, doi: 10.1016/j.ohx.2018.01.001.
- [172] C. Zhang, B. Wijnen, and J. M. Pearce, “Open-Source 3-D Platform for Low-Cost Scientific Instrument Ecosystem,” *Journal of Laboratory Automation*, vol. 21, no. 4, pp. 517–525, 2016, doi: 10.1177/2211068215624406.
- [173] S. Hou *et al.*, “Advanced Development of Primary Pancreatic Organoid Tumor Models for High-Throughput Phenotypic Drug Screening,” *SLAS Discovery*, vol. 23, no. 6, pp. 574–584, 2018, doi:

- [174] M. Kowalski, K. Hill, K. Prasauckas, and T. Jones-roe, “Automating the generation and analysis of 3D cell cultures in Matrigel ®.” [Online]. Available: <https://www.moleculardevices.com/en/assets/app-note/dd/img/automating-the-generation-and-analysis-of-3d-cell-cultures-in-matrigel>.
- [175] O. Sirenko *et al.*, “Phenotypic Characterization of Toxic Compound Effects on Liver Spheroids Derived from iPSC Using Confocal Imaging and Three-Dimensional Image Analysis,” *ASSAY and Drug Development Technologies*, vol. 14, no. 7, pp. 381–394, Sep. 2016, doi: 10.1089/adt.2016.729.
- [176] B. G. Reid *et al.*, “Live Multicellular Tumor Spheroid Models For High-Content Imaging and Screening In Cancer Drug Discovery,” *Current Chemical Genomics and Translational Medicine*, vol. 8, no. 1, pp. 27–35, Feb. 2014, doi: 10.2174/2213988501408010027.
- [177] E. O’Duibhir *et al.*, “Machine Learning Enables Live Label-Free Phenotypic Screening in Three Dimensions,” *ASSAY and Drug Development Technologies*, vol. 16, no. 1, pp. 51–63, 2018, doi: 10.1089/adt.2017.819.
- [178] M. E. Boutin, T. C. Voss, S. A. Titus, K. Cruz-Gutierrez, S. Michael, and M. Ferrer, “A high-throughput imaging and nuclear segmentation analysis protocol for cleared 3D culture models,” *Scientific Reports*, vol. 8, no. 1, p. 11135, Dec. 2018, doi: 10.1038/s41598-018-29169-0.
- [179] E. Leary, C. Rhee, B. T. Wilks, and J. R. Morgan, “Quantitative Live-Cell Confocal Imaging of 3D Spheroids in a High-Throughput Format,” *SLAS Technology*, vol. 23, no. 3, pp. 231–242, Jun. 2018, doi: 10.1177/2472630318756058.
- [180] T. J. Puls, X. Tan, M. Husain, C. F. Whittington, M. L. Fishel, and S. L. Voytik-Harbin, “Development of a Novel 3D Tumor-tissue Invasion Model for High-throughput, High-content Phenotypic Drug Screening,” *Scientific Reports*, vol. 8, no. 1, p. 13039, Dec. 2018, doi: 10.1038/s41598-018-31138-6.

Appendices

Content

Appendix	Title
A	Commercially available high-content imaging systems suitable for 3D imaging
B	List of Materials
C	Technical Drawings of customised Components
D	Detailed changes made to “Marlin-bugfix-2.0x”
E	Python Code for Z-stacks
F	Python Code “Smooth Mix”
G	Detailed Overview of all Mixing Step Optimisation Experiments
H	Python Code for optimised Mixing
I	DoE: Results of the Model Analysis

Appendix A

Commercially available high-content imaging systems suitable for 3D imaging

In the application column, each first row refers to information provided by the manufacturer (n.s. = not specified), the second column refers to applications in the literature.

Company Name	Optics	Environ. Control	Compatible to automation	Application	
				Non-scaffold	Scaffold-based
BD Biosciences BD Pathway 855	Confocal Spinning Disk Widefield	yes	yes	n.s. -	n.s. [72], [96]
Bioteck Cytation 5	Fluorescence Brightfield Colour Brightfield Phase Contrast	yes	yes	n.s. -	n.s. -
GE Healthcare Life Science InCell Analyzer 6500	Confocal (line-scanning) Widefield Brightfield Differential Interference Contrast Phase Contrast	yes	yes	n.s. [173]	n.s. -
Logos Biosystems CELENA®X	Fluorescence Brightfield Colour Brightfield Phase Contrast	yes	no	yes -	n.s. -
Molecular Devices ImageXpress Micro Confocal	Confocal Spinning Disk Widefield Brightfield Phase Contrast	yes	yes	yes [175]	[174] -
Nexcelom Bioscience Celigo Imaging Cytometer	Fluorescence Brightfield	no	no	yes -	yes -
Perkin Elmer Operetta CLS	Confocal Spinning Disk Fluorescence Brightfield	yes	yes	n.s. [6]	n.s. [71], [176], [177]
Perkin Elmer Opera Phenix	Confocal Spinning Disk Widefield Brightfield	yes	yes	n.s. [178], [179]	n.s. [180]
Thermo Fischer Cell Insight CX7 LZR	Confocal Spinning Disk Widefield Brightfield	yes	yes	yes -	n.s. -

Company Name	Optics	Environ. Control	Compatible to automation	Application	
				Non-scaffold	Scaffold-based
Yokogawa Cell Voyager CV 8000	Confocal Spinning Disk Brightfield Phase Contrast	yes	no	yes	n.s.
				-	-
Yokogawa CQ1 Benchtop	Confocal Spinning Disk Brightfield Phase Contrast	no	yes	yes	n.s.
				-	-
Zeiss Celldiscoverer 7	Fluorescence Brightfield Phase Contrast	yes	yes	n.s.	n.s.
				-	-

Appendix B

List of Materials

	Designator	Manufacturer/ Supplier	Article Number	Quan- tity	Price (EUR)
Microscope					
Objective & Stage					
1	Objective	Nikon / Thorlabs	N10X-PF	1	965.20
2	Translation Stage	Thorlabs	MS1S/M	1	206.57
3	Objective Adapter	Thorlabs	SM1A12	1	19.87
4	Objective Mount	Thorlabs	CT101	1	43.29
5	Adapter Plate	Thorlabs	MS103/M	1	27.54
6	Angle Bracket	Thorlabs	MS102	1	30.75
7	Stepper motor NEMA 8	Eckstein Shop	20x30mm, 3.9 V, 0.6 A/Phase	1	22.58
8	Gear wheel	Maedler	MS58	1	9.26
9	Gear wheel	Conrad	Reely Motorritzel	1	3.89
10	Adapter Plate	Mechanical Workshop	Z01	1	-
Body					
11	45° Mirror	Thorlabs	CCM1-P01_M	1	157.58
12	Cube Connector	Thorlabs	CM1-CC	1	44.27
13	Filter Cube	Thorlabs	DFM1L/M	1	417.73
14	Condensor Lens	Thorlabs	ACL2520U-DG15-A	1	28.03
15	Retaining Ring	Thorlabs	SM1RRC	1	10.14
16	Tube Lens	Thorlabs	AC254-100-A-ML	1	96.40
17	Adjustable Lens Tube	Thorlabs	SM1V10	2	31.37
18	Lens Tubes	Thorlabs	SM1L05	2	23.58
19	Lens Tube	Thorlabs	SM1L20	1	15.45
20	Cage Plate	Thorlabs	CP13/M	1	29.80
21	Assembly Rods	Thorlabs	ER4-P4	1	25.26
22	End Caps	Thorlabs	SM1CP2	2	17.12
23	Adapter	Thorlabs	SM1A39	1	19.28
24	Dichroic Mirror	Edmund Optics	87284	1	160.00
25	Emission Filter	Edmund Optics	87244	1	476.00
26	Camera	pi3g.com	Raspberry Pi HQ Camera	1	54.79
Illumination Unit					
27	Blue LED	LEDs.de	Cree XP-E2 SMD-LED, blue	1	3.74
28	Mint LED	Thorlabs	MINTD3	1	144.35
29	LED Driver	Meanwell	LLD-700HW	2	12.64

	Designator	Manufacturer/ Supplier	Article Number	Quan- tity	Price (EUR)
30	Power Supply	LEDs.de	12 V - 18 W)	2	17.46
31	Heat Sink	LEDs.de	round 28.5 mm	2	9.80
32	Sticky Pad	LEDs.de	round 28.5 mm	2	2.98
33	Filter Cube	Thorlabs	CM1-DCH/M	1	159.36
34	Lens Tube	Thorlabs	SM1L03	2	27.08
Mounting					
35	Aluminium Breadboard	Thorlabs	MB1545/M	1	120.99
36	Post Holder Ø12.7	Thorlabs	PH20/M-P5	1	32.91
37	Optical Post	Thorlabs	TR30/M	1	13.32
38	Optical Post	Thorlabs	TR40/M	1	9.30
39	Post Spacer	Thorlabs	TR5M	1	18.60
			Microscope Costs		3,508.28
XYZ-Stage					
X-stage					
40	Ball Screw	Misumi	BSST1004-280	1	283.40
41	Bracket	Misumi	BNFA1004R-20	1	47.48
42	Support Unit / Bearings	Misumi	C-BSW8S-SET	1	64.96
43	Linear Rail Guides	Misumi	SSE2BSL10-265	2	170.26
44	Coupling	Misumi	MST-12-5-6	1	28.68
45	Stepper Motor NEMA 14	Watterott	2018246	1	12.18
46	Baseplate	Mechanical Workshop	X01	1	14.03
47	Connection Bridge	Mechanical Workshop	X02	1	7.41
48	Motor holder	Mechanical Workshop	X03	1	1.74
Y-stage					
49	Ball Screw	Misumi	BSST0802-230	1	302.35
50	Bracket	Misumi	BNFB802R-20	1	38.11
51	Support Unit	Misumi	C-BSW6-SET	1	64.29
52	Linear Rail Guides	Misumi	SSE2BSL10-210	2	152.89
53	Coupling	Misumi	MWSS-12-4.5-5	1	40.25
54	Stepper Motor NEMA 14	Watterot	2018246	1	12.18
55	Baseplate	Mechanical Workshop	Y01	1	7.41
56	Connection bridge	Mechanical Workshop	Y02	1	6.13
57	Motor holder	Mechanical Workshop	Y03	1	1.74
58	Gripper	Mechanical Workshop	Y04	1	-
Z-stage					
59	Easy-Mechatronics System	Dold Mechatronik	EMS1216A	1	196.17
60	Stepper Motor NEMA 17	Watterott	201898	1	12.18
61	Connection Plate	Mechanical Workshop	Z02	1	7.69
62	Angle	Mechanical Workshop	Z03	2	4.09
			XYZ-stage Costs		1,475.62
Frame					
63	Aluminium Profile	Misumi	NFSL6-3030-560	4	20.52

	Designator	Manufacturer/ Supplier	Article Number	Quan- tity	Price (EUR)
64	Aluminium Profile	Misumi	NFSL6-3030-400	10	34.27
65	Aluminium Profile	Misumi	NFSL6-3030-270	4	10.14
66	Bracket and Joints	Misumi	HBLFSN6-SST	32	62.45
67	T-Nut	Roboter Bausatz Shop	I-Type Nut 6	2	4.78
68	Bracket	Roboter Bausatz Shop	30 I-Typ Nut 6	2	7.12
				Frame Costs	139.28
Electronics					
69	Raspberry Pi 3 Model B	Reichelt	Rasp 3 B+ All In Bundle	1	66.90
70	Arduino Mega	Watterott	2018428	1	43.87
71	RAMPS 1.6+	BigTreeTech		1	17.34
72	USB Cable	Watterott	2018444	1	1.27
73	Motor Driver	Watterott	SilentStepStick TMC2130 V2	3	33.48
74	Motor Driver	Watterott	SilentStepStick TMC2209	1	10.24
75	Heat Sinks	Watterott	14.5x15x13	4	4.64
76	Jumper Wires	Watterott	F/F	1	2.44
77	Jumper Wires	Watterott	F/M	1	2.44
78	Jumper Wires	Watterott	M/M	1	2.44
79	Power Supply	Watterott	12 V/DC 5A 60W	1	16.58
				Electronics Costs	201.64
				Total Costs	5,324.82

Appendix C

Technical Drawings of customised Components

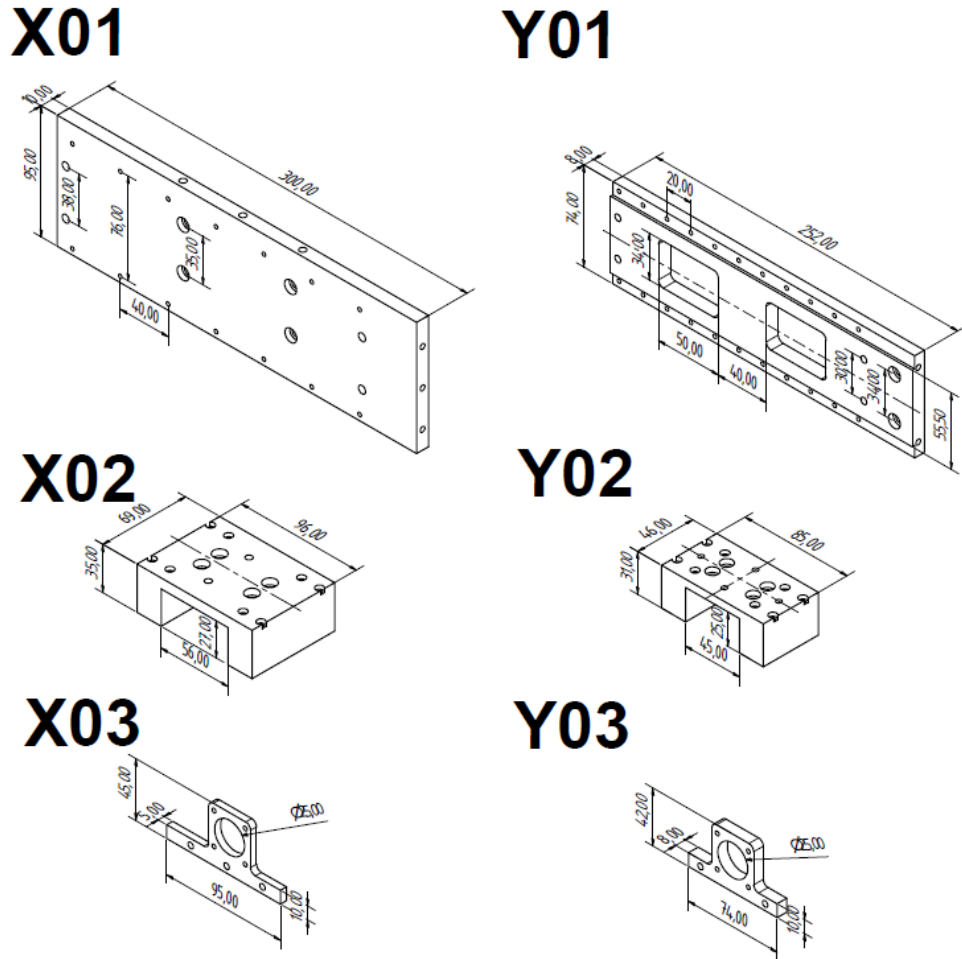


Figure 0.1 Drawings of customised components with main dimension data.

X01: X-baseplate, Y01: Y-baseplate, X02: connection bridge of the X-stage, Y02: connection bridge of the Y-stage, X03: stepper motor holder of the X-stage, Y03: stepper motor holder of the Y-stage

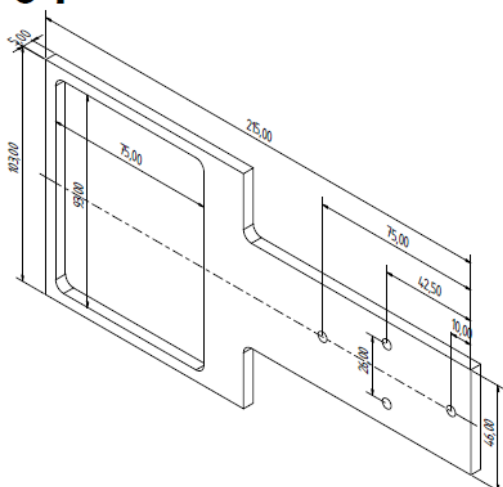
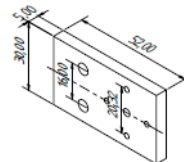
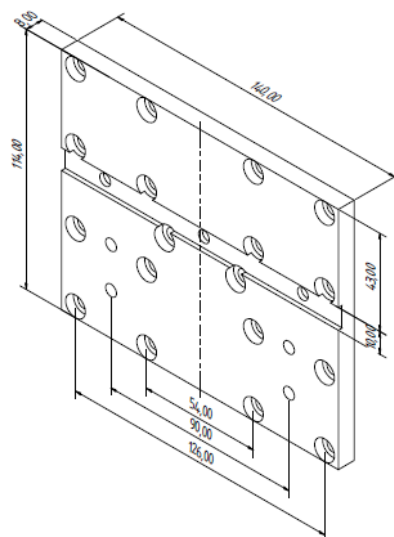
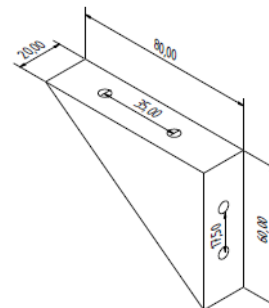
Y04**Z01****Z02****Z03**

Figure 0.2 Drawings of customised components with main dimension data.

Y04: tissue culture plate gripper, Z01: Adapter to connect Z-fine stage to aluminium profile,
Z02: Z-coarse stage connection plate, Z03: angle to connect X-stage to Z-coarse stage

Appendix D

Detailed Changes made to the Firmware “Marlin-bugfix-2.0x”

Table 0.1: Changes to *Configuration.h*

Code Line	New Code	Comment
73	#define STRING_CONFIG_H_AUTHOR "(Kahl, Melanie)"	Insert your name
129 130 131	#ifndef MOTHERBOARD #define MOTHERBOARD BOARD_RAMPS_14_EFB #endif	Define the Motherboard you use
412 ... 420	#define TEMP_SENSOR_0 998 ... #define TEMP_SENSOR_BED 998	Virtual heating of heating bed
679 680 681	#define USE_XMIN_PLUG #define USE_YMIN_PLUG #define USE_ZMIN_PLUG	Specify endstop connectors
713 714 715 716 717 718 719	#define X_MIN_ENDSTOP_INVERTING true #define Y_MIN_ENDSTOP_INVERTING true #define Z_MIN_ENDSTOP_INVERTING true #define X_MAX_ENDSTOP_INVERTING false #define Y_MAX_ENDSTOP_INVERTING false #define Z_MAX_ENDSTOP_INVERTING false #define Z_MIN_PROBE_ENDSTOP_INVERTING false	Inverting endstop logic
739 740 741 ... 747	#define X_DRIVER_TYPE TMC2130 #define Y_DRIVER_TYPE TMC2130 #define Z_DRIVER_TYPE TMC2209 ... #define E0_DRIVER_TYPE TMC2130	Define motor drivers
802	#define DEFAULT_AXIS_STEPS_PER_UNIT { 50, 100, 66.67, 160 }	Define axis steps per unit (steps/mm)
809	#define DEFAULT_MAX_FEEDRATE { 1000, 1000, 1000, 100 }	Set Feedrate higher
1187 1188 1189	#define INVERT_X_DIR false #define INVERT_Y_DIR false #define INVERT_Z_DIR false	Invert stepper direction, if an axis goes the wrong way
1229 1230	#define X_BED_SIZE 1200 #define Y_BED_SIZE 2000	Define length of X and Y axis

Table 0.2: Changes to *Configuration_adv.h*

Code Line	New Code	Comment
736 737 ... 739	#define HOMING_BUMP_MM { 10, 10, 10 } #define HOMING_BUMP_DIVISOR { 2, 2, 2 } ... #define HOMING_BACKOFF_POST_MM { 20, 20, -20 }	Define position after homing
2569 2570 2571 ... 2576	#define X_CS_PIN 63 #define Y_CS_PIN 40 #define Z_CS_PIN 42 ... #define E0_CS_PIN 65	Define SPI pins for TMC driver
2590 2591 2592 2593	//#define TMC_USE_SW_SPI #define TMC_SW_MOSI 66 #define TMC_SW_MISO 44 #define TMC_SW_SCK 65	Software option for SPI drivers
2782	#define TMC_DEBUG	Enable TMC debugging

Appendix E

Python Code for Z-Stacks

```

# LED Imports
import RPi.GPIO as GPIO    # necessary for use of GPIO pins
from time import sleep
from picamera import PiCamera
from fractions import Fraction
import serial

## --- LED Settings ---
# define using boardnumbers (1-14) or GPIO numbers
blueLED = 15
mintLED = 24

GPIO.setmode(GPIO.BCM)    # using GPIO numbers
# Define Pin als Output
GPIO.setup(blueLED, GPIO.OUT)      # GPIO 15 / Board-Pin 10 - Ground 6
GPIO.setup(mintLED, GPIO.OUT)      # GPIO 24 / Board-Pin 18 - Ground 14

## RAMPS Settings#
ramps = serial.Serial('/dev/ttyACM0', 250000) # define Port and Baudrate
print(ramps.name, 'is online') # check Port's name

# Camera Settings
cam = PiCamera(
    resolution=(2028, 1520),
    framerate=Fraction(1, 6),
    sensor_mode=3)

sleep(1)
ramps.write(b'G91\n') # Set to relative mode
print('Set to relative mode') # print a question

cam.start_preview()
cam.preview.alpha = 240

for i in range(61):
    sleep(1)
    ramps.write(b'G91\n')          # set to relative mode
    ramps.write(b'G0 E2\n')        # move Z focus
    cam.shutter_speed = 150000
    cam.iso = 400
    sleep(1)
    GPIO.output(mintLED, GPIO.HIGH) # Mint LED on
    filenameM = '20220130_R2_D4_mi_E2_%02d.bmp' % i
    sleep(2)
    cam.capture(filenameM)
    sleep(1)
    GPIO.output(mintLED, GPIO.LOW)   # Mint LED off
    cam.shutter_speed = 200000
    cam.iso = 600
    sleep(1)
    GPIO.output(blueLED, GPIO.HIGH) # Blue LED on
    filenameB = '20220130_R2_D4_b1_E2_%02d.bmp' % i
    sleep(2)
    cam.capture(filenameB)
    print('Captured:', i)
    sleep(1)
    GPIO.output(blueLED, GPIO.LOW)   # Blue LED off

ramps.write(b'G0 E-121\n')
cam.stop_preview()
ramps.close()

```

Appendix F

Python Code for “Smooth Mix”

```
def smoothMix(pipette, dH, stroke=1, iterations = 1 ,speed = 5000):
    for i in range(iterations):

        strokeLength = pipette.positions['bottom'] - pipette.positions['top']
        speedCommandString = "G1 F%d" % speed

        # relative movement
        robot._driver.send_command('G91')
        robot._driver.send_command(speedCommandString)

        partialStroke = stroke*strokeLength
        moveCommandString = "G1 Z%2.f B%2.f" % (dH, -partialStroke)
        moveCommandString2 = "G1 Z%2.f B%2.f" % (-dH, partialStroke)
        # mix 1
        robot._driver.send_command(moveCommandString)
        robot._driver.send_command(moveCommandString2)

        # absolute movement
        robot._driver.send_command('G90')
```

Appendix G

Detailed Overview of all Mixing Step Optimisation Experiments

Protocol Nr.	Exp. Nr.	GelMA conc.	Speed	CV	Protocol	Time (min)
1	1	10%	0	9.8%	PBS (without Orange G)	n. A.
2		10%	0	63.1%	10x mixing	n. A.
3		10%	0	23.2%	10x, waiting, 10x	n. A.
4		10%	0	36.3%	20x	n. A.
5		10%	0	36.5%	10x smooth mix	n. A.
6		10%	0	16.1%	10x smooth mix	n. A.
7		10%	0	4.7%	manual	n. A.
8		10%	0	1.3%	Control (PBS + Orange G: PBS, 50:50)	n. A.
9	2	10%	0	26.2%	manual	n. A.
10		10%	0	88.8%	20x smooth mix	n. A.
11		10%	0	6.4%	10x, asp-disp, 10x	n. A.
12		10%	0	7.8%	10x, asp-disp, 6x, asp-disp, 10x	n. A.
13		10%	0	10.6%	10x, asp-disp, 6x, asp-disp, 6x, asp-disp, 8x	n. A.
14		10%	0	32.4%	10x smooth mix, asp-disp, 3x, 10x smooth mix	n. A.
15		10%	0	28.7%	10x smooth mix, upper layer asp-disp further down, 10x smooth mix	n. A.
16		10%	0	6.3%	10 x smooth mix, asp-disp, 6x, asp-disp, 6x, asp-disp, 6x, 10x smooth mix	n. A.
17a	3	10%	0	3.7%	10x, asp-disp, 12x, waiting, 10x, asp-disp, 12x,	n. A.
17b		10%	0	4.7%	10x, asp-disp, 12x, waiting, 10x, asp-disp, 12x,	n. A.
18a		10%	0	18.7%	10x, asp-disp, 12x,	n. A.
18b		10%	0	6.6%	10x, asp-disp, 12x,	n. A.
19a		10%	0	8.1%	10 x smooth mix, asp-disp, 6x, asp-disp, 6x, asp-disp, 6x, 10x smooth mix	n. A.
19b		10%	0	8.3%	10 x smooth mix, asp-disp, 6x, asp-disp, 6x, asp-disp, 6x, 10x smooth mix	n. A.
20a		10%	0	41.5%	10 x smooth mix, asp-disp, 6x, asp-disp, 6x, 10x smooth mix, asp disp, 8x, 10x smooth mix	n. A.
20b		10%	0	54.5%	10 x smooth mix, asp-disp, 6x, asp-disp, 6x, 10x smooth mix, asp disp, 8x, 10x smooth mix	n. A.

Protocol Nr.	Exp. Nr.	GelMA conc.	Speed	CV	Protocol	Time (min)
21a	4	10%	0	17.2%	10x, asp-disp, 12x, waiting, 10x, asp-disp, 12x,	n. A.
21b		10%	0	5.0%	10x, asp-disp, 12x, waiting, 10x, asp-disp, 12x,	n. A.
22a		10%	0	14.4%	10x, asp-disp, 12x, 10x, asp-disp, 12x	n. A.
22b		10%	0	11.6%	10x, asp-disp, 12x, 10x, asp-disp, 12x	n. A.
23a		10%	0	6.1%	10 x smooth mix, asp-disp, 6x, asp-disp, 6x, 10x smooth mix	n. A.
23b		10%	0	3.5%	10 x smooth mix, asp-disp, 6x, asp-disp, 6x, 10x smooth mix	n. A.
24	5	10%	0	4.5%	10x, asp-disp, 12x, 10x, asp-disp, 12x	n. A.
25		10%	0	2.0%	10x, asp-disp, 10x, asp-disp, 10x	5:42
26		10%	1	2.5%	10x, asp-disp, 10x, asp-disp, 10x	4:47
27		10%	2	2.8%	10x, asp-disp, 10x, asp-disp, 10x	4:10
28		10%	3	2.2%	10x, asp-disp, 10x, asp-disp, 10x	3:56
29		10%	1	2.0%	10x smooth mix, asp-disp, 6x, asp-disp, 2x, 10x smooth mix	3:10
30		10%	2	1.5%	10x smooth mix, asp-disp, 6x, asp-disp, 2x, 10x smooth mix	3:00
31		10%	3	2.5%	10x smooth mix, asp-disp, 6x, asp-disp, 2x, 10x smooth mix	2:45
32a	6	5%	2	1.9%	10x mix, asp-disp, 10x, asp disp, 10x	3:44
32b		5%	2	2.9%	10x mix, asp-disp, 10x, asp disp, 10x	3:44
33a		5%	2	2.7%	smooth mix, asp-disp, 6x, asp-disp, 2x, smooth mix	2:35
33b		5%	2	2.3%	smooth mix, asp-disp, 6x, asp-disp, 2x, smooth mix	2:35
34a		15%	2	4.2%	10x mix, asp-disp, 10x, asp-disp, 10x	3:44
34b		15%	2	5.6%	10x mix, asp-disp, 10x, asp-disp, 10x	3:44
35a		15%	2	3.2%	smooth mix, asp-disp, 6x, asp-disp, 2x, smooth mix	2:35
35b		15%	2	2.4%	smooth mix, asp-disp, 6x, asp-disp, 2x, smooth mix	2:35

Explanations:

- 10x: 10 times standard mixing at fixed positions
- asp-disp: aspirating 1000 µl from the top layer and dispensing it further down
- a, b: Replicates

Appendix H

Python Code for optimised Mixing

```
equipment['pd1000'].move_to(equipment['ingredients'].wells(wellposition['Mixing1']).bottom(0))

equipment['pd1000'].move_to(equipment['ingredients'].wells(wellposition['Mixing1']).bottom(-33), strategy='direct')

smoothMix(equipment['pd1000'], 18, stroke=1 ,iterations=10)

equipment['pd1000'].move_to(equipment['ingredients'].wells(wellposition['Mixing1']).bottom(0))

equipment['pd1000'].aspirate(1000,equipment['ingredients'].wells(wellposition['Mixing1']).bottom(-39))

equipment['pd1000'].dispense(1000,equipment['ingredients'].wells(wellposition['Mixing1']).bottom(-46))

equipment['pd1000'].mix(2, 1000, equipment['ingredients'].wells(wellposition['Mixing1']).bottom(-46))

equipment['pd1000'].mix(2, 1000, equipment['ingredients'].wells(wellposition['Mixing1']).bottom(-44))

equipment['pd1000'].mix(2, 1000, equipment['ingredients'].wells(wellposition['Mixing1']).bottom(-42))

equipment['pd1000'].aspirate(1000,equipment['ingredients'].wells(wellposition['Mixing1']).bottom(-39))

equipment['pd1000'].dispense(1000,equipment['ingredients'].wells(wellposition['Mixing1']).bottom(-46))

equipment['pd1000'].mix(2, 1000, equipment['ingredients'].wells(wellposition['Mixing1']).bottom(-46))

equipment['pd1000'].move_to(equipment['ingredients'].wells(wellposition['Mixing1']).bottom(0))

equipment['pd1000'].move_to(equipment['ingredients'].wells(wellposition['Mixing1']).bottom(-33), strategy='direct')

smoothMix(equipment['pd1000'], 18, stroke=1 ,iterations=10)

equipment['pd1000'].move_to(equipment['ingredients'].wells(wellposition['Mixing1']).bottom(0))
```

Appendix I

DoE: Results of the Model Analysis

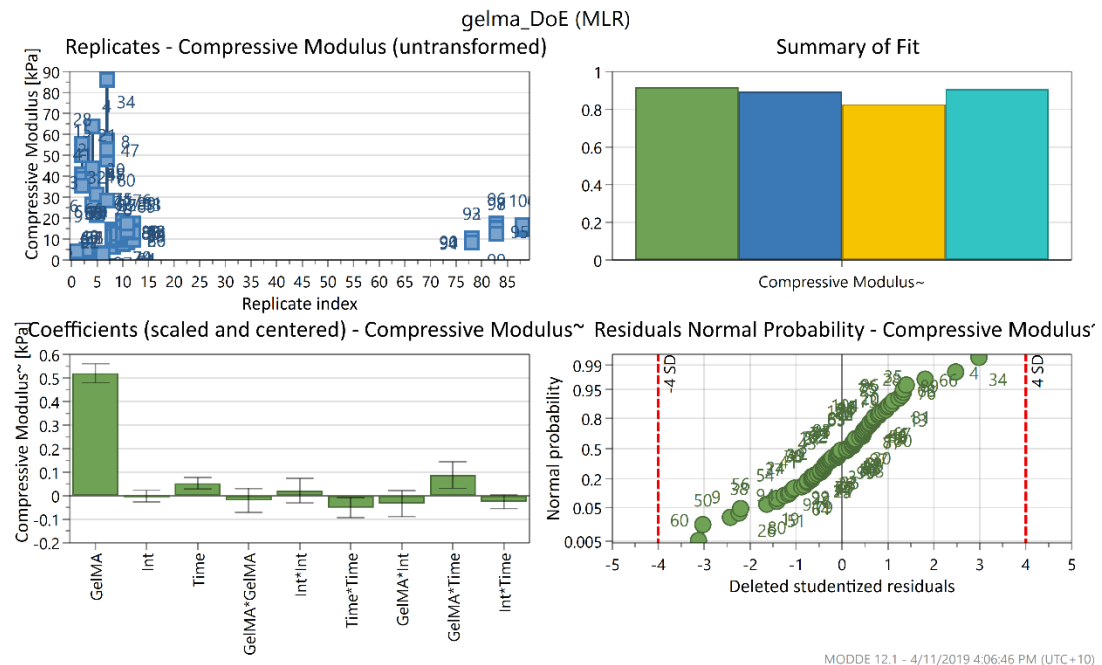


Figure 0.3 Overview plot of model validation

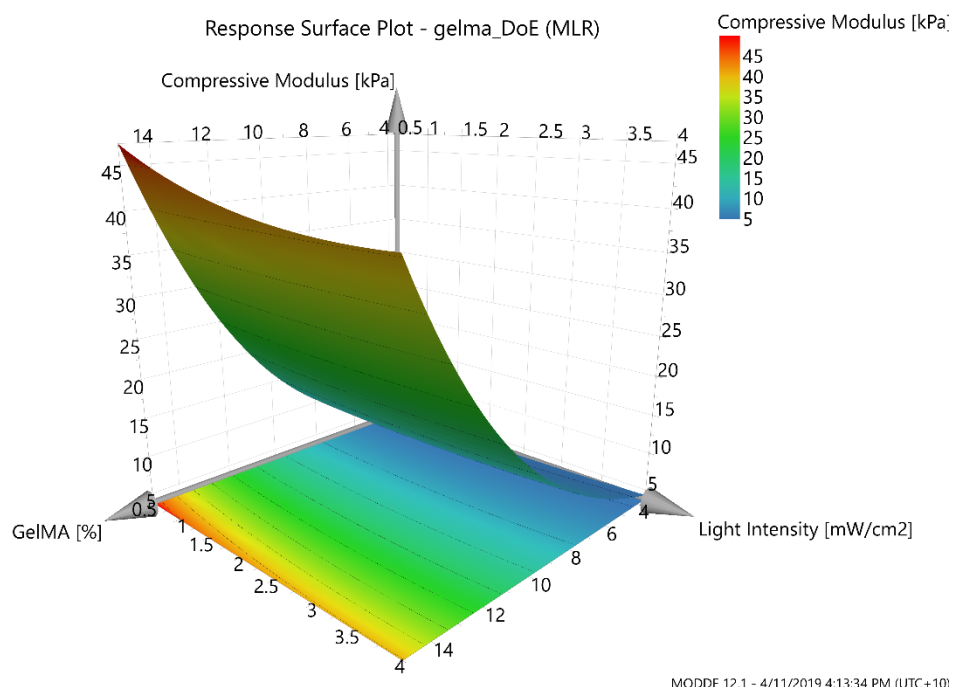


Figure 0.4 3D response surface plot